Development of a Force Field with Condensed Phase Consistent Charges for N,N'- dialkylimidazolium Room Temperature Ionic Liquids

by

Vela Mngadi
BSc (Hons)

Dissertation submitted in fulfillment of the academic requirements for the degree

Master of Science

In the Scientific Computing Research Unit, Department of Chemistry at the University of Cape Town

Supervisor: Dr Gerhard A. Venter

February 2015

Declaration

The work described in this dissertation was carried out at the Scientific Computing Research Unit, Department of Chemistry at the University of Cape Town, from January 2012 to January 2015, under the supervision of Dr. Gerhard A. Venter

These studies represent original work by the author and have not otherwise been submitted in any form for any degree or diploma to any tertiary institution. Where use has been made of the work of others it is duly acknowledged in the text.

_____

Vela Mngadi

_____

Date

Abstract

Most force field models for Room temperature ionic liquids cannot properly elucidate statics and dynamics. It is in this context that we set to assess the most efficient way to model RTILs while maintaining the integrity of the liquids statics and dynamics.

The development approach begins with the investigation of the effects that the linear scaling of partial atomic charges on nonpolarisable force fields from a reference potential has on the structure and dynamics of the room temperature ionic liquids (RTILs) 1-butyl-3-methylimidazolium tetraflouroborate $[C_4MIM][BF_4]$ and 1-butyl-3-methylimidazolium hexaflourophosphate $[C_4MIM][PF_6]$. The results show that the three-dimensional structure of the liquid is changed ever so slighter by the linear scaling of atomic charges. While dynamic properties such as viscosity and self-diffusion coefficients were majorly affected by charge scaling. Self–diffusion coefficients that span a range of four orders of magnitude between the original model and the scaled model where the ionic charge was ±0.6 e. Viscosity estimates calculated usingthe Green-Kubo and the Einstein relationships revealed that the linear scaling of atomic charges results in increased mobility of the simulated liquid.

Implicit inclusion of polarisation effects was investigated, Here a new charge scheme development using Quantum mechanics/Molecular mechanics (QM/MM) methods in CHARMM 35 interfaced with GAMESS-UK was propose. The atomic charges were derived from liquid phase calculations using an iterative procedure. This was carried out for individual ions and cation-anion pairs, for the analysis of charge transfer, within the liquid environment. The results obtained gave predictions of density, liquid structure and self-diffusion coefficients that were in excellent agreement with experimental data available. This method is preferable over the commonly used charge scaling methodology which is deem as an unphysical approach for the simulation of $[C_4MIM][BF_4]$ and $[C_4MIM][PF_6]$.

A polarisable force field based on the Drude oscillator model is presented. The model proves to be most effective for the simulation of RTILs. The force field accurately reproduced experimental results for the physicochemical properties reviewed.

Dedications

This dissertation is dedicated to my late grandmother Sizani Mngadi who is the cornerstone of my existence and to my younger siblings Phumelele and Andile, may you draw inspiration from this dissertation.

Signed by candidate Signature Removed

Acknowledgements

I am sincerely grateful to the following:

- My supervisor Dr Gerhard A. Venter for his excellent supervision, advice, motivation, patience and guidance.
- All four of my parents: Lucky & Zendele Cele, Simphiwe & Philisiwe Zama. Each of you has played a significant role in my life, thank you.
- Members of the Scientific Computing Research Unit (Team SCRU) for their encouragement and assistance given throughout my project.
- The Centre for High Performance Computing (CHPC) for their resources, which were made available to me.
- ***All*** of my friends, with a special mention to Samkelo Ngcobo, Mthokozisi Gazu, Sanele Mkhize, Tsakane Chauke, Khanyile Xashimba and Teboho Tsotetsi. Thank you for the support, encouragement and motivation. Thank you for being there.
- The National Research Foundation (NRF) and The University of Cape Town for the funds provided for my research.

Abbreviations and Symbols

^{o}C	Degrees Celsius
Å	Angstrom
ρ	Density
atm	Atmosphere
RTIL	Room Temperature Ionic Liquid
$[C_4MIM]$	1-butyl-3-methylimidazolium
$[C_2MIM]$	1-ethyl-3-methylimidazolium
BF_4	Tetrafluoroborate
PF_6	Hexafluorophosphate
SCN	Thiocyanate
DCA	Dicyanamide
MD	Molecular Dynamics
η	Viscosity
D	Debye
MSD	Mean Square Displacement
RDF	Radial Distribution Function
QM	Quantum Mechanics
MM	Molecular Mechanics
e	Electronic Charge
Δ	Change
DF	Density Fitted Charges
CPC	Condensed Phase Consistent Charges

Contents

List Of Figures

CHAPTER 1

Introduction

1.1 Ionic Liquids

An ionic liquid is a kind of liquid that is composed entirely of ions, such as KCl, and NaCl in their molten state, however, in recent years the term has been used, exclusively, to describe a sub class of organic salts that are molten near room temperature or in their pure state. In literature various terms such as molten salts, room temperature molten salts, liquid organic salts, room temperature ionic liquids have been used interchangeably to describe what is now accepted as an ionic liquid. For this work the term Room Temperature Ionic Liquid (RTIL) will be used as it best fits the liquids under study.

Formally the term Room Temperature Ionic Liquids (RTILs) refers to salts that are molten at or below the boiling point of water, which is 100 °C. Bulky heterocyclic cations in combination with organic or inorganic anions appear to be a common feature amongst ionic liquids that are be classified as RTILs.

In addition to having relatively low melting points, RTILs have a large liquidus range which means they stay in their liquid phase over an extended temperature range, for example 1-butyl-3-methylimidazolium bis(trifluoromethanesulfonyl)imide, a RTIL, melts at -6 °C and has a decomposition temperature of 439 °C thus 1-butyl-3-methylimidazolium bis(trifluoromethanesulfonyl)imideis a liquid over a temperature range of 445 °C. It is such qualities that make RTILs an excellent alternative to traditionally used organic solvents in chemical reaction. They have the potential to provide a large temperature range at which chemical reaction can be performed. Low to negligible vapour pressures and being non-flammable are other attributes of RTILs that have led to the suggestion of RTILs being used as a substitute for traditional organic solvents in chemical reaction.

It is evident that room temperature ionic liquids have features that are very unique and that have the potential to be exploited in order to improve the efficiency of certain chemical processes. Much effort is still needed in producing a body of physical data for ionic liquids so that we may understand these fascinating substances and as such we have seen a constant increase in the amount of attention given to room temperature ionic liquids over the last 20 years as can be seen in figure 1.1 below.

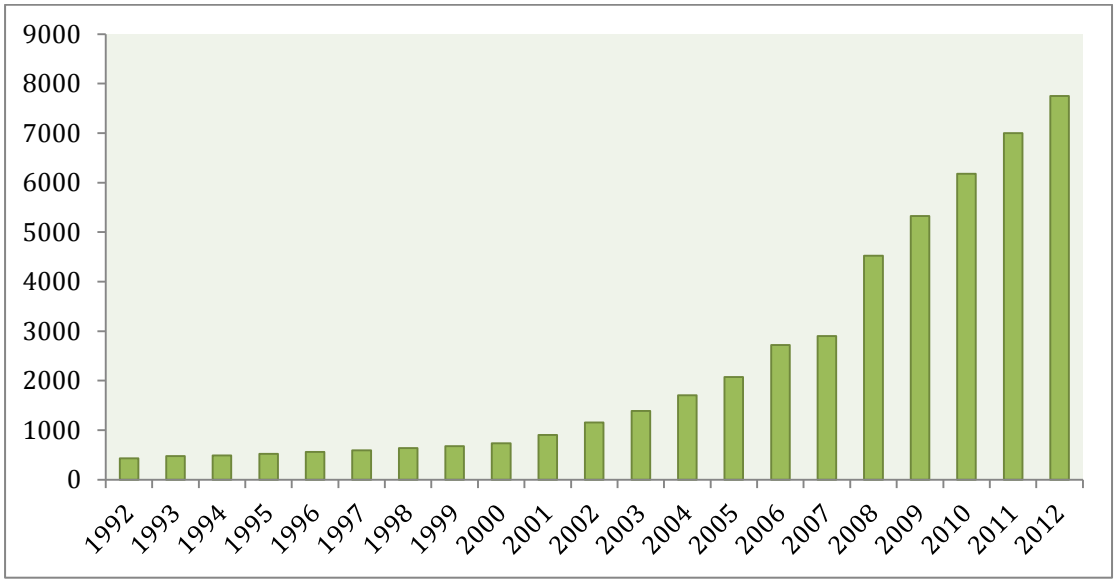

Figure 1.1: Number Of publications citing Ionic Liquids in the last twenty years.

1.2 Synthesis of Ionic Liquids

Room temperature ionic liquids are typically formed from large organic cations in combination with organic or inorganic anions. Most of the literature that is available on RTILs reports on the ionic liquids which are widely understood, which are those RTILs based on the 1,3-alkylimidazolium cation. There are, however, other cations and anions that have been used to synthesize RTILs and figure 1.2 and 1.3 shows examples of such ions that can be paired to make an ionic liquid

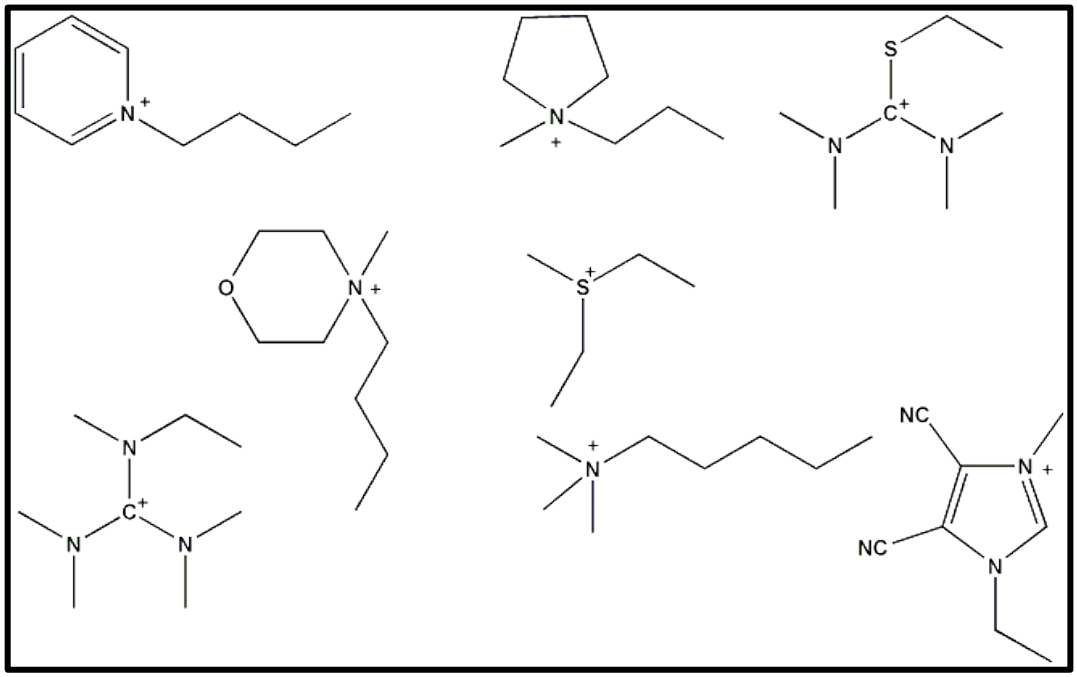

Figure 1.2: Examples of Room temperature Ionic Liquid cations.

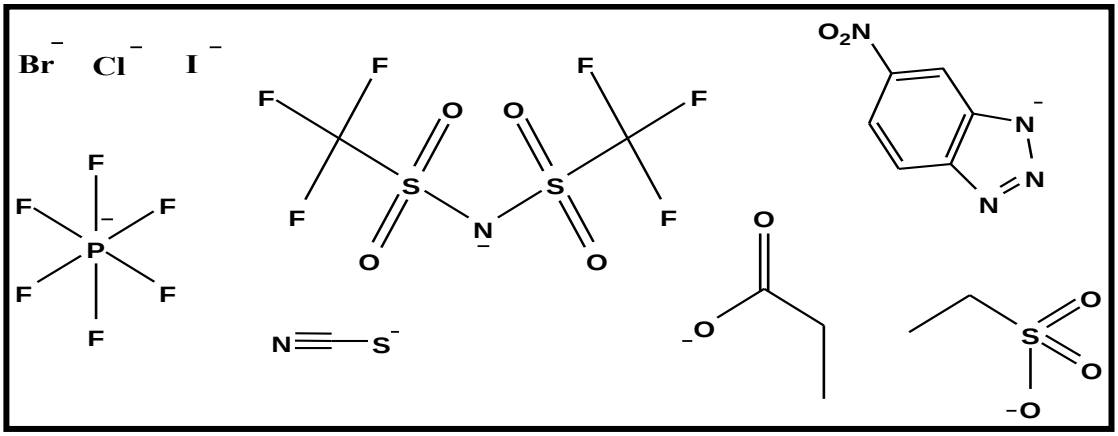

Figure 1.3: Examples of Room temperature Ionic Liquid anions.

Figure 1.2 and 1.3 do not give an exhaustive list of anions and cations that may be used in RTILs, there is a significant number of other ions that may be utilized for the synthesis of RTILs..

A study by P Walden is considered to be the first to report the synthesis of the RTIL ethylammonium nitrate in 1914 [1]. The ethylammonium nitrate species was produced by the addition of concentrated nitric acid to ethylamine, the moisture was then removed by means of a distillation and the resulting product was a pure salt that is molten at room temperature.

There are a number of synthetic routes that one can use to prepare RTILs, however, the synthesis can be broken down into two fundamental steps: the formation of the desired cation followed by an anion exchange step where necessary, to produce the intended product. In cases where the desired cation is commercially available at a reasonable price then only the second step is required to produce the RTIL of choice.

1.3 Ionic Liquid Applications

Ionic liquids have been a part of industrial processes for some time now, there are a number of examples mentioned in literature in which salts that are molten at relatively low temperature appear in chemical plants. A common example is that of the "Red oil" which was accepted as Friedel-Crafts catalyst in the process of ethylation of benzene in the mid-19th century [20]. This "red oil" was observed as separate liquid in the solution and it was only discovered much later that the oil was indeed a salt.

A second example and perhaps one of the most iconic examples of the application of ionic liquids in industry is a process that was established by BASF in 1990 known as the BASIL^{TM}-process, which is the first process that make use of RTILs in a commercial scale. This process utilizes low melting liquid Vilsmeir salt, which is a mixture of low temperature melting salts, that are liquid at the reaction temperature of 60 °C to chlorinate an acid with phosgene [18].

1.3.1 Potential fields of application

Predominantly ionic liquids have received a great deal of attention for their electrochemical abilities [19], however, more recently, researchers are now interested in applying ionic liquids outside of their classical chemical use as solvents and process chemical [20], one such area of application is the use of ionic liquids as performance chemicals.

RTILs can be synthesized to have specific properties and as such have been termed tunable liquids, the ability to tune the liquid to one's desire has opened them up to applications in the pharmaceutical/biological industry; this was shown in the work of W. Hough *et al.* in 2007 [20]. In their study they were able to show some of the strategies that could be employed to take advantage of the dual nature of ionic liquids that may lead to the realization of enhancement to the control of solubility, bioavailability, stability and new delivery options.

With the emergence of companies such as IoLiTec (Ionic Liquid Technologies), a company specializing in marketing and developing ionic liquid products and their applications, we should expect more and more interesting applications of these substances in the future [21].

1.4 Properties of Ionic Liquids

The characteristic properties of RTILs can be significantly varied by the choice of cations and anions making up the liquid. Factors such as shape, size and charge distribution of either the cation or the anion play a significant role in the overall observed property of the RTIL. An understanding of the structure-property relationship is essential for the design of RTIL with tailored properties for a specific application.

In addition to traditional experimental techniques, molecular simulation is one such way in which the properties of RTILs may be studied. The first molecular simulation study of RTILs was that undertaken by Hanke *et al.* back in 2001 [2], where they used molecular dynamics simulations to study 1,3-dimethylimidazolium chloride ($[C_1mim][Cl]$), 1,3-dimethylimidazolium hexafluoro-phosphate ($[C_1mim][PF_6]$), 1-ethyl-3methylimidazolium chloride ($[C_2mim][Cl]$) and 1-ethyl-3methylimidazolium hexafluorophosphate ($[C_2mim][PF_6]$) in their crystalline state. In addition they also modeled ($[C_1mim][Cl]$) and ($[C_1mim][PF_6]$) in the liquid state at high temperatures as both these substance have relatively high melting points. In their study they computed properties, which include average energies, molar volumes, liquid structure using radial distribution functions and self-diffusion coefficients from the mean square displacement.

The same group followed up their study in the year that followed; here they studied the behavior of different substance including water, methanol, dimethyl ether and propane in [C1mim][Cl] using molecular dynamics [4]. In the same year, 2002, Maginn and co-workers carried out Monte Carlo simulations of 1-butyl-3-methylimidazolium hexafluorophosphate $[C_4mim][PF_6]$ which they quickly followed up with another study where they compared their simulated results to experimentally available data [5].

It was around this period that other groups started gaining interests in studying RTILs and there was an influx of reports that discussed the investigation of these substances, force field development (C. Margulis *et al.* 2002 [6]; de Andrade *et al.* 2002 [7, 8], Lopes and Pádua 2004 [9];), physical chemistry of ionic liquids (Fujii *et al.* 2008 [10]; Yan *et al.* 2006 [11]), and their applications (Balducci, *et al.* 2004 [12]; Lazzari *et al.* 2007 [13]). The list of studies presented here is not exhaustive, however, reviews of simulation results will be discussed in some of the sections to follow and will include more recent data. These early studies played a significant role in identifying some of the finer detail currently employed in modeling RTILs today. The sections to follow look at the relationship between the structural features and the observed physical and chemical properties will be discussed with reference to previous studies.

1.4.1 Liquid structure

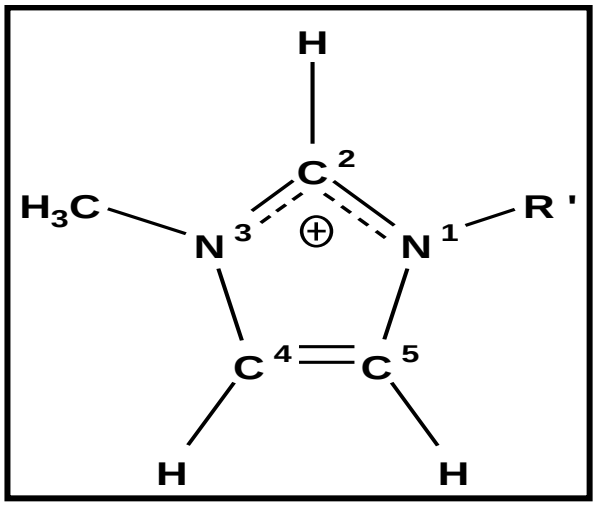

Figure 1.4: A schematic representation of a 1-alkyl-3-methylimidazolium cation.

Figure 1.4 shows a schematic representation of 1-alkyl-3-methylimidazolium a typical RTIL cation. [$C_n$mim] is a typical notation used for the 1-alkyl-3-methylimidazolium cation is where the *n* indicates the number of carbons atoms in the alkyl chain **R'**. This cation can be paired up with any anion from the list in section 1.2 to from an ionic liquid. Gas phase *ab initio* studies have been used to calculate low energy conformations of room temperature ionic liquids [15] and shown in figure **1.5** is an example of one such low energy conformation for [C_4mim][BF_4].

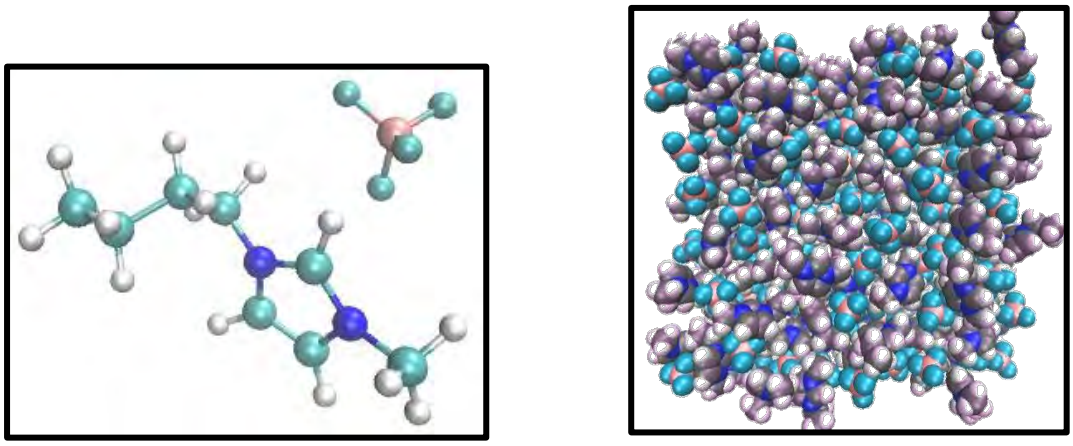

(a) (b)

Figure 1.5: (a) Optimised1-ethyl-3-methylimidazolium tetrafluoroborate [C_4mim]-[BF4] ion pair (b) snapshot of a simulation box containing 250 ions of [C_4mim][BF4].

From these calculations it was observed that anions preferentially localize near the hydrogen atom attached to the C_2 carbon (figure 1.4), which is the most acidic site of an imidazolium cation, this was shown by the work of Hunt *et al.* in 2006 [27]. Experimental data has suggested that the C_2-H hydrogen is relatively more acidic than the rest of the hydrogens in the imidazolium ring. Hunt and co-workers [27] showed that all the hydrogen atoms on the imidazolium ring have a similar charge and that the only difference between the hydrogen atoms was the charge on the C_2 carbon which lead to the conclusion that the acidity of the hydrogen atoms in the ring should be associated with charge on the carbon-hydrogen unit and not the proton on its own. Wang *et al.* observed the same localization using bulk phase molecular dynamics for $[C_4mim][PF_6]$, they found that the anion can be located at different positions during the course of the simulation , however, the most populated regions were those close to the C_2 position which is consistent with the picture given in figure 1.5 (a).

In 2004 Urahata and Ribeiro simulated a range dialkylimidazolium based RTILs with one of the alkyl groups on the cation ranging from methyl to octyl and the other being a methyl. They paired these cations with anions like F^-, Cl^-, Br^- and PF_6^- using simulations boxes much like that shown in figure 1.5 (b). Their work successfully proved that the structure of the liquid has a dependence on the alkyl chain length. With the aid of a course-grained model Voth and co-workers took this a step further and showed that as the tail of the alkyl chain increases the tails tend to aggregate resulting in polar and nonpolar domains within the liquid that are stable on a simulation timescale.

A discussion on the structure property relationship in ionic liquids would be incomplete without the mention of hydrogen bonding interactions. In their study focusing on the $[C_4mim][Cl]$ ionic liquid, Hunt and co-workers deduced that in a between the imidazolium cation and chloride anion exists a very strong ionic hydrogen bond with minor covalent contributions. Hydrogen bonds formed in ionic liquids are somewhat different to those formed in typical molecular liquids; this is because ionic liquids are made up of anions and cations whereas molecular liquids from which hydrogen bonding is widely understood are made of neutral molecules.

The character of hydrogen bonds formed in ionic liquids are somewhat different to those formed in typical molecular liquids; this is because ionic liquids are made up of charged species, whereas molecular liquids, from which most hydrogen bonding studies originate, consists of neutral molecules.

1.4.2 Thermal properties of ionic liquids

In addition to understanding the structure of the liquid and the overall observed properties one should also have a good understanding of how ionic liquid behave at typical working temperatures. This is essential when deciding whether or not to use a certain ionic liquid in a particular application. As mentioned all the salts that are of interest to us as ionic liquids are molten at ambient temperature or below the boiling point of water. These ionic liquids tend to form glasses at very low temperature and have minimal vapour pressure up to their decomposition temperature [22].

The thermal stability of an ionic liquid is directly linked to the strength of the formed heteroatom-carbon or heteroatom-hydrogen bonds in conjunction with the stability of the formed ion species [23]. In ionic liquids, the melting point is a very important property as it indicates whether a salt should be considered an ionic liquid or not. Thus some experimental and computational studies will report melting point, freezing point, glass transition point, and decomposition point temperatures of RTILs [24-26].

1.4.3 Ionic liquid dynamics

Molecular dynamics have been highly successful in assisting with the understanding of the dynamic properties of room temperature ionic liquids for ion pairs and in the bulk phase. Molecular dynamics simulations have given researchers insight to RTIL properties such as thermal conductivity, electrical conductivity, viscosity and self-diffusivity, however, due to the fact that a very wide range of species of ionic liquids can be produced by the mixing and matching of anions and cations, generating or establishing trends that are generic to all or most RTIL has proven to be a rather difficult task. Early studies by Del Popolo and Voth [14] and Morrow and Maginn [5]

became the stepping-stones towards establishing some trends amongst RTILs. Both these studies reported a slow dynamic behavior in room temperature ionic liquids.

Morrow and Maginn [5] reported the development of an all atom force field for 1-butyl-3-methylimidazolium hexafluorophosphate [C_4mim][PF_6] RTIL which at the time and currently a widely studied ionic liquid. They reported computation of self-diffusion from the slopes of the root mean-square displacement of cations and anions, which were two orders of magnitude slower than the self-diffusion coefficients computed for water at room temperature. The results obtained from these studies brought about doubt about self-diffusion coefficient predicted from previous studies as up to this point reports were based on very short simulation times, less than 1ns. The shortcomings of running short simulations will be highlighted in chapters 2 and 4.

A key difference between ionic liquids and conventional liquids is that ionic liquids are made up of charged species. The charge on the individual species making up an ionic liquid has a direct impact on the overall observed properties as an electrostatic interaction is introduced. It is thus not uncommon for researchers to investigate the electrostatic interactions that exist within the liquid and the role that they play in the observed properties.

When modelling RTILs it is important to have your simulated results as close as possible to those results obtained by way of experiments, although in most cases simulation have been done ahead of experiments. As far as simulating RTILs is concerned, it has been a very difficult task to establish a force field model that predicts properties that are comparable to experiments, this is more so the case for transport properties. [32] This will be highlighted in section 2.2.

In general, current force fields for the simulation of RTILs are not good at reproducing experimental results for transport properties and it is for this reason that

much of the effort being put into force field research in RTIL, focuses on predicting transport properties [5-7,32,33].

1.5 Objectives

In this study we set out to develop a force field model that would accurately model imidazolium based room temperature ionic liquids on the basis of experimental data that is available to us.

We aim to investigate the electrostatic interactions that govern the behavior exhibited by ionic liquids, deepening our current understanding of these electrostatic effects which are key to the observed physicochemical properties (see section 2.2.4). The knowledge gained from the electrostatic interaction studies will be incorporated into our force field model to develop a force field that best represents the electrostatics of an ionic liquid system and in turn predicts reproducible physicochemical properties.

1.6 References

1. P. Walden, Bull. Acad. Imper. Sci. (St Petersburg) 1914, 1800.
2. C. Hanke , S. Price, R. Lyndell-Bell, Mol. Phys., 2001, **99**, 801 – 809.
3. E. Hawlicka, T. Dlugoborski, Chem. Phys. Lett., 1997, **268**, 325.
4. C. Hanke , N. Atamas, R. Lyndell-Bell, Mol. Phys., 2001, **99**, 801 – 809.
5. T. Morrow, E Maginn, J. Phys. Chem. B, 2002, **106**, 12807 – 12813.
6. C. Margulis, H. Stern, B. Berne 2002J.Phys.Chem. B, **106**, 12017 -12021
7. J. de Andrade, E. Boes, H. Stassen, J. Phys. Chem. B, 2002, **106**, 3546 -3548
8. J. de Andrade, E. Boes, H. Stassen, J. Phys. Chem. B, 2002, **106**, 13344
9. J. Lopes, A.Pádua, J. Phys. Chem. B, 2004, **108**, 16893 – 16898
10. K. Fujii, Y. Soejima, J. Phys. Chem. B, 2008,**112**, 4329 – 4336.
11. Yan, T., Y. Wang, C. Knox, J. Phys. Chem. B, 2010,**114**, 6886-6904.
12. A. Balducci, U. Bardi, S. Caporali, M. Mastagostino, F. Soavi, Electrochem. Comm., 2004,**6**, 566-570.
13. M. Lazzari, M. Mastragostino, F. SoaviElectrochem. Comm., 9, 1567-1572.
14. M. Del Popolo, G. Voth G, J. Phys. Chem. B, 2004, **108**, 1744 – 1752.
15. Z. Liu, S. Huang, W. Wang, J. Phys. Chem. B, 2004, **108**, 12978 – 12989.
16. S. Urahata, M. Ribeiro, J. Phys. Chem. Chem. B, 2004, **120**, 1855 – 1862.
17. J. Strenger-Smith, C. Webber, N. Anderson, A. Chafin, K. Zong, J. Reynolds, J. Electrochem. Soc., 2002, **149**, A973 – A977.
18. S. El Abedin, F. Endres, Chem. Phys. Chem., 2006, **7**, 58 -61.
19. P. Wasserscheid, T. Welton, Ionic liquids in synthesis, Second edition, 2008, WILEY_VCH Verlags GmbH & Co. KGaA, Weinheim.
20. W. Hough, M. Smiglak, H. Rongdriguez, R. Swatlaski, S. Spear, D. Daly, J. Pernak, J. Grisel, R. Carliss, M. Soutullo, J. Davis Jr., R. Rogers, New J. Chem., 2007, **31**, 1429 – 1436.
21. N. Plechkova, K. Seddon, Chem. Soc. Rev., 2008, **37**, 123 – 150.
22. H. Ngo, K. LeCompte, L. Hargens, A. McEwen,ThermochimicaActa 357 – 358, 2000, 97 – 102

23. M. Shukla, S. Saha, A comparative study of piperidinium and imidazolium based ionic liquids thermal spectroscopic and theoretical studies, Chapter 3, http://dx.doi.org/10.55772/51797.
24. S. Zhang, N. Sun, X. He, X. Lu, X. Zhang, J. Phys. Chem. Ref. Data, 2006, **35**, 1475 – 1515.
25. S. Aparicio, M. Atilhan, F. Karadas, Ind. Eng. Chem. Res., 2010, 49, 9580 – 9595.
26. J. Holbery, K. Seddon, J. Chem. Soc., Dalton Trans. 1999, 2133
27. P. Hunt, B. Kirchner, T. Welton, Chem. Eur. J., 2006, **12**, 6762 – 6775.
28. I. Skarmoutsos, D. Dellis, R. Matthews, T. Welton, P. Hunt, J. Phys. Chem. B 2012, **116**, 4921−4933
29. Kempter, V.; Kirchner, B. J. Mol. Struct. 2010, **22**, 972.
30. Thar, J.; Brehm, M.; Seitsonen, A. P.; Kirchner, B. J. Phys. Chem. B 2009, **113**, 15129.
31. Hunt, P. A. J. Phys. Chem. B 2007, **111**, 4844.
32. F. Dommert, K. Wendler, R. Berger, L. D. Site, C. Holm, Chem. Phys. Chem., 2012, **13**, 1625 – 1637
33. V. V. Chaban, I. V. Voroshylova, O. N. Kalungin, Phys. Chem. Chem. Phys., 2011, **13**, 7910 – 7920

CHAPTER 2

Review: Force Fields for Ionic liquids

2.1 Introduction

In this chapter we review some of the force field models that are currently available in literature. We do not attempt to give an exhaustive list of all the force fields that are available, however, we highlight those that are closely aligned with our research interests.

Molecular dynamics simulation methods have been shown to be a valuable tool in studying systems on an atomistic level. For room temperature ionic liquids these methods have been used to study thermodynamic properties, structure and dynamics. The methods used are based on classical force field models that allow one to investigate systems containing a significant number of ions. The cornerstone of any MD simulation is the force field that is expected to reproduce properties over a larger number of state points.

Parameterisation of force fields for bimolecular systems has been achieved with great success in various packages such as AMBER [1], OPLS-AA [2] and CHARMM [3]. These models have been developed for a large class of molecules and are often not transferable between systems within a certain temperature range. When RTILs started becoming a field of interest amongst researchers, force field parameters were not available for many cations and anions, as most force fields focus on neutral biomolecular fragments. Thus suitable new models had to be produced, starting from existing parameters designed for these biomolecules.

2.2 Classical Force Fields

Classical force fields using all atom, united atom and coarse grained descriptions will be introduced, as well as reduced charge, polarisable and force fields that make use of charges calculated from bulk phase systems.

Classical force fields do not explicitly account for the treatment of polarisation effects that exist within bulk systems. As an attempt to include these effects, which have been found to be significant in the dynamic behavior of ionic liquids, various methods have been used, such the calculating partial charges from bulk systems, which is discussed in section 2.4., however, with the increased computational power available today it is not uncommon for polarisation effects to be included explicitly in a force field model. For field models that do not account for polarisation, non-polarisable models, suffer from lack of transferability and almost always overestimate interactions within the liquid systems. For instance, a force field that is parameterized for the calculation of properties a particular RTIL and is found to reproduce experimental data within reasonable experimental error will not necessarily produce excellent results in a case of another RTIL.

2.2.1 All Atom Models

As the name suggests, in all atom models, all atoms are explicitly defined and have characteristics or parameters associated with them in the force field. Classical force fields are typically made up of three different kinds of parameters which dictate the electrostatic, bonding and the non-bonded short-range interactions. The bonding interactions are usually adapted from a quantum mechanical calculation typically in the gas phase and some cases from available crystal structures. Electrostatic and non-bonded interactions on the other hand can be derived through a number of varying methods and techniques.

Charges fit to a Connolly surface, Charge from Electrostatic potentials (CHELPG) [4,5], Connolly [6,7] and Geodesic [8], have been arbitrarily used to calculate partial charges while there are very few methods that can be used to obtain a usable set of non-bonded short range interaction parameters; most of these depend on data provided by experiment. This was a potential setback in the initial stages of RTIL studies by molecular dynamics as very little to no data was available for these systems. Thus parameterisation for RTILs was based on well-established force fields.

In 2001 the first force field for RTILs was published by Hanke and co-workers [9]. Their force field had point charges derived from a distributed multipole analysis [10] of a charge density while the short-range interaction of their parameterisation consisted of parameters selected from a number of different force fields. The authors proposed both an all-atom and a unit atom model and showed that an all atom model was required in order to reproduce crystal structure data accurately.

Others subsequently adopted the practice used in this study. In the studies that followed parameters from different force fields were used in conjunction with partial charges refined using varying methods until such time that specific non-bonded parameters for RTILs were establish [11-13].

In 2002 a study that attempted to implicitly treat polarisation was presented by Morrow and Maginn [14]. They used non-bonded short-range interaction parameters from the CHARMM [3] force field and the authors, based on quantum mechanical computations of ion pairs, suggested a net reduced charge of ± 0.9e exists on the ions. The force field was shown to achieve good agreement with molar volumes, however, it failed to replicate isothermal compressibility. The force field gave diffusion coefficients that were comparable to those derived from experimentally determined viscosity using the Stokes-Einstein expression

A substantial number of force fields have been proposed since then yet one of the most prevalent issues that plagued the force fields still haunts them today; the issue of transferability. As the number of RTILs is large, a consistent and transferable force field model is most desirable as it would pioneer the in silico design of RTILS.

In 2004 Padua and co-workers presented one of the first systematic force fields for the treatment of RTILs. [39] The OPLS-AA/AMBER based force field was initially developed for nine room temperature ionic liquids with the following cations: 1-butyl-3-methylimidazolium, 1-ethyl-3-methylimidazolium and 1-hexyl-3-methylimidazolium in combination with the anions chloride, hexafluorophosphate and the nitrate ion. The force field was then further extended to include pyridinium and phosphonium cations as well as bromide and dicyanamide anions amongst others. [30, 40,42-44] The number of RTILs included in the force field reported by Padua and co-workers is impressive and the density and crystal phase cell parameters of the RTILs were well reproduced, however, the ability of this force field model to predict heat of vaporization and transport properties showed much less success. For instance, the enthalpy of vaporization for the $[C_2MIM][Ntf_2]$ RTIL was found to be approximately 20 $kJ.mol^{-1}$ higher [45] than values obtained from experiment. [29]

2.2.2 United Atom Models

In addition to all atom force fields, united atom force fields have been developed. Again Hanke *et al.* [9] were the first to propose such a model and their overall conclusion was that an all atom model would be required in order accurately reproduce the crystal structure of the liquid. The model developed by Hanke and co-workers had the hydrogen atoms condensed with the carbon atoms, a common approached also used by Shah and co-workers [15].

The latter authors parameterised their force field for $[BMIM][PF_6]$ and collapsed their anions into a single unit. Instead of using parameters from different force fields this group elected to adapt parameters from the OPLS-UA framework [16], bond lengths and angles were fixed at the optimized values obtained from quantum mechanical calculation and derived their partial charges using the CHELPG method. This model was only applied in Monte Carlo simulations and thus there is no insight into its dynamic abilities. Monte Carlo methods stochastic techniques, which means they are based on the use of random numbers and probability statistics to investigate problems.

In this case this method was used to calculate the molar volume, cohesive energy density, isothermal compressibility, and cubic expansion coefficient. Although in the initial work only results from Monte Carlo simulations were reported, subsequently it was shown that the model is able to produce liquid dynamic data comparable to that obtained by way of experiments [17-19].

2.2.3 Coarse-Grained Models

In a coarse-grain model ions making up the RTIL are represented in bead-like manner. The coarse-grain model is a step up from a united atom model as the beads are made up of a number of different groups and likewise the united atom model is a step up from an all-atom model. In a coarse-grain model the electrostatic interactions of the beads are given by the sum of the charges of all the constituting atoms from an atomistic model. Wang and co-workers proposed one such model, introducing a method to derive potential for the simulations based on a force matching technique. A key difference between this model and previously discussed all atom and united atom model is the manner in which the short-range interactions are represented [31].

Bhargava and co-workers proposed a different technique towards developing a coarse-grained model and their model also differed in the way in which they treated short range interaction using a 9-6 potential [32,33].

2.2.4 Charge Reduction

Room temperature ionic liquids force fields are typically parameterised to fit experimental data. Classical force fields tend to overestimate interactions that exist within the ionic liquids giving results that deviate from what is observed in experiment. Reduction of total ion charges has been found to be a viable remedy to accelerate liquid dynamics and produce results comparable to experiment. This technique is said to work as it mimics the average charge screening resulting from Polarisation as well as charge transfer effects [20]. Youngs and Hardacre [21] later investigated the effect of this approach explicitly and showed that the dynamics of a RTIL is dramatically accelerated by the linear scaling of the partial charges on each of the atoms. Structural properties, however, showed little change over different scaling factors in the range 0.5-0.9.

The scaling down of partial charges remedies the overestimation of interactions typical of classical force fields, however, scaling factors are not transferable between systems, a scaling factor that works perfectly for one system will not necessarily work just as well for another system. In addition one has no way of knowing what scaling factor would work best for a system until they have conducted a series of trial and error experiments.

Chaban *et al.* presented a new non-polarisable force field model for the simulation of transport properties of imidazolium-based RTILs making extensive use of scaling factors [46]. The force field model presented was a modification of a model originally presented by Liu *et al.* [47]. The model was developed by scaling the electrostatic charges with a factor obtained from ab initio calculations of several ionic pairs in the bulk systems. The model showed considerable improvement in reproducing experimental values of the diffusion coefficients, shear viscosities and ionic conductivities, with diffusion coefficients improving by a factor of 10. Some viscosities and ionic conductivities were, however, still underestimated. When compared to the original model by Liu *et al*., the presented model showed minor to

insignificant changes in structural properties predicted. The lead author, Chaban, of the previous study in the same year presented modifications to the force field [37]. In this study different scaling factors across a range were tested and it was shown that a scaling factor determined from a liquid property, such as the density, was good to model transport properties.

Studies on RTILs have shown that a linear relationship exists between the degree of polarisation and the scaling factor [35]. This relationship calls in to question whether the scaling of the electrostatic forces that exists between the ions can be used to accurately mimic the average influence of polarisation. In a 2012 study by Schrönder, and Steinhauser [26] the relationship between the linear scaling of charges and polarisation effects were investigated and their finding are discussed here.

In force fields Coulombic energy is calculated as shown in equation 2.1;

$$U^{Coul} = \frac{1}{4\pi\varepsilon_0}\sum_{i\alpha}\sum_{i\beta>i\alpha}\frac{q_{i\alpha}\cdot q_{i\beta}}{|r_{i\alpha}-r_{i\beta}|} \qquad \text{Eq 2.1}$$

Schroder and Steinheauser showed using perturbation theory that the average Coulombic energy is reduced by a factor $(S^{eff})^2$:[26]

$$U^{Coul} = \frac{(S^{eff})^2}{4\pi\varepsilon_0}\sum_{i\alpha}\sum_{i\beta>i\alpha}\frac{q_{i\alpha}\cdot q_{i\beta}}{|r_{i\alpha}-r_{i\beta}|} \qquad \text{Eq 2.2}$$

partial charges in an MD simulation can be scaled by the simple multiplication of permanent charges with this scaling factor:

$$q_{i\alpha}^{eff} = S^{eff} q_{i\alpha} \qquad \text{Eq 2.3}$$

Figure 2.1 gives a schematic representation of atomic charges enclosed in spherical cavities in a homogenous dielectric continuum of $\boldsymbol{\varepsilon^{con}} = \varepsilon_\infty$.

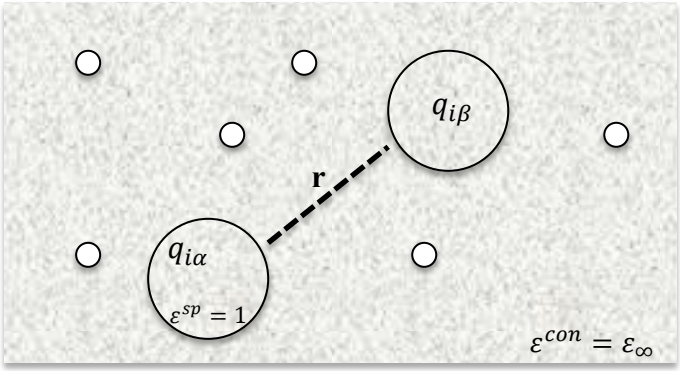

Figure 2.1: A schematic representation of the interactions between ions. Atoms are approximated with spheres. The dielectric constant inside the sphere $\boldsymbol{\varepsilon^{sp}}$ is one and outside the sphere $\boldsymbol{\varepsilon^{con}} = \boldsymbol{\varepsilon_\infty}$ (figure adapted from reference 35).

Since the charges are immersed into a dielectric continuum their interactions are changed and their Coulombic interactions can be represented as: [35]

$$U^{Coul} = \frac{(S^{eff})^2}{4\pi\varepsilon_\infty} \sum_{i\alpha} \sum_{i\beta>i\alpha} \frac{q_{i\alpha} \cdot q_{i\beta}}{|r_{i\alpha} - r_{i\beta}|} \qquad \text{Eq 2.4}$$

and it follows that a suitable scaling factor, for the simulation of RTILs, can be obtained from the Clausius-Mosottti type equation:

$$S^{\varepsilon_\infty} = \frac{1}{\sqrt{\varepsilon_\infty}} \qquad \text{Eq 2.5}$$

prior to trajectory production [35]. Thus a correction based on the scaling of permanent charges may be achieved by reference to the experimental optical dielectric constant [36]. Several studies have compared the effectiveness of charge reduction in contrast to explicit inclusion of polarisation to a force field model [35,37,38]. In the work carried out by Schroder [35] it was reported that the scaled charge model shows poor performance on a local level but shows excellent effectiveness at the collective level. This gives the indication that charge scale models

may be suitable for the prediction of bulk properties such as diffusion, which are usually overestimated by common force fields, but for more sophisticated studies on the local interactions of a RTIL system, such as hydrogen bonding, one should rather employ a polarisable force field model.

There are other routes that can be used to optimize a non-polarisable force field. Koddermann and co-workers [29] reported a force field based on that developed by Lopes and co-workers [30]. in their study they elected to retain the partial charges, but adjusted the Lennard-Jones (LJ) parameters. With this change they obtained results that are comparable to experiment.

2.3 Polarisable Force Field Models

Polarisable force fields allow for much more detailed insight into the dynamical behaviour of a system since they mimic the spontaneously induced perturbation of the molecular electronic structure due to its immediate environment. One of the first polarisable force fields of RTILs was proposed by Yan *et al.* [22] which was parameterized for 1-ethyl-3-methyl-imidazolium nitrate [C_2mim][NO_3]. In a follow up study they were able to compare their simulation results in detail with both a polarisable and non-polarisable model [23,24], the polarisable model showed significant improvement in the predicted transport properties as the self-diffusion coefficients were approximately 3 times larger and the viscosity were shown to 60% lower. There are a number of methods that one can use to implement Polarisation into a force field for RTILs that have been reported in literature such as the point dipole [25], the Drude oscillator [26], the quantum mechanical wave function-based [27] and the charge equilibrium model [28].

Borodin developed and validated a systematic many-body polarisable force field model for the simulation of 30 different RTIL systems at 298, 333, and 393 K [41].

The force field model produced made accurate predictions of density, heat of vaporization, self-diffusion coefficients, ionic conductivity, and viscosity for both small organic molecules and RTILs. For example, the deviation between the experimental and simulated diffusion coefficients was found to be in the region of 20-40% for all the RTILs simulated. Experimental procedures for the elucidation of physicochemical properties of RTILs, very rarely produce results that are of the same quality as those that have been reported using molecular dynamics simulations. The success of this force field in predicting RTILs transport properties attests to RTIL transport being driven by electrostatic polarisation effects. The model developed in the listed study was based on the polarisation model of Thole, a model that considers a point electric dipole placed on the atoms in addition to the permanent charges.

Polarisable models are essentially the best models to use for the simulation of RTILs, however, the computational costs that are attributed with using such models is often seen as a disadvantage to these models and thus researchers continue to look for alternatives that are less computationally demanding.

2.4 Charges from Bulk Phase Systems

Klahn *et al.* propose an all-atom force field for guanidinium-based (GILs) ionic liquids [48]. The force field was based on the charge distribution in the actual liquid in an attempt to improve the prediction of energetic and dynamic properties of the ionic liquids under study and to investigate the impact of electron charge transfer and Polarisation on various properties of GILs [48]. The authors reported an average electron charge transfer between -0.12 and -0.06 e from anions to the central cations and diffusion coefficients were found to be are substantially increased by a factor of up to 3.5.

In 2012 Zhang and Maginn reported having derived partial atomic charges of two ionic liquids from periodic crystal phase (condensed phase) calculations in Density Functional theory (DFT) [34]. They found that the total charge on the ions was ±0.8e and used these charges in molecular dynamics simulations. A comparison of the results using an Amber force field with four different sets of charges showed that not only is the dynamic nature of the liquid influenced by the overall charge, the charge distribution within the ions influences the observed results.

Closely related to the work of the authors mentioned in this section is the work of Krekeler *et al*., in this study they investigated the molecular polarisation of an ionic liquid in the bulk phase [49]. Their analysis revealed that electric dipole moments of cations and anions are characterized by large fluctuations, however, the fluctuations are primarily due to molecules in the immediate surroundings, a result affirming the work of the former authors.

2.5 References

1. W. D. Cornell, D. Maxwell, J. Tirado-Rivers, J. Am. Chem. Soc., 1996, **118**, 11225 – 11236.
2. W.D. Cornell, P. Cieplak, C. I. Bayly, I. R. Gould, K. M. Merz, Jr. D. M. Ferguson, D. C. Spellmeyer, T. Fox, J. Caldwell, P. A. Kollman, J. Am. Chem. Soc., 1995, **117**, 5179 – 5197.
3. A. D. Mackrell, D. Bashford, M. Bellott, R. L. Dunrack, J. D. Evanseck, M. Field, S. Fischer, J. Gao, H. Gou, S. Ha, D. Jeseph-McCarthy, L. Kuchir, T. Ngo, D. Nguyen, B. Prodhom, W. Reiher, R Roux, M. Schlenkrich, J. Smith, R. Stote, J. Straub, N. Watanabe, J. Wiórkiewicz-Kuczera, D. Yin, M. Karplus, J. Phys. Chem. B, 1998, **102**, 3586 – 3616.
4. C. M.Breneman, K. B. Wiberg, J. Comput. Chem., 1990, **11**, 361 -373.
5. L. E. Chirlian, M. M. Francl, J. Comput. Chem., 1987, **8**, 894 – 905.
6. B. H. Besler, K. M, Merz, P. Kollman, J. Comput. Chem.,1990, **11**, 431 -439.
7. K. M. Merz, J. Comput. Chem., 1992, **13**, 749 – 767.
8. M. A. Spackman, J. Comput. Chem., 1996, **17**, 1 – 18.
9. C. Hamke, S. Price, R. Lynden-bell, Mol. Phys., 2001, **99**, 801.
10. A. Stone, M. Alderton, Mol. Phys., 1985, **56**, 1047 – 1064.
11. C. Margulis, H. Stern, B. Berne, J. Phys. Chem. B, 2002, **106**, 12017 – 12021.
12. J. De Andrade, E. Boes, H. Stassen, J. Phys. Chem. B, 2002, **106**, 13344 – 13351.
13. J. De Andrade, E. Boes, H. Stassen, J. Phys. Chem. B, 2002, **106**, 3546 – 3548.
14. T. Morrow, E Maginn, J. Phys. Chem. B, 2002, **106**, 12807 – 12813.
15. J. K. Shah, J. F. Brennecke, E. J. Maginn, Green Chem., 2002, **4**, 112 -118.
16. W.L. Jorgensen, J. D. Madura, C. J. Swenson, J. Am. Chem. Soc., 1984, **106**, 6638 – 6646.
17. S. M. Urahata, M. C. C. Ribeiro, J. Chem. Phys., 2004, **120**, 1855 -1863.
18. S. M. Micaelo, A. M. Baptista, C. M. Soares, J. Phys. Chem. B, 2006, **110**, 14444 – 14451.
19. Z. Lui, X. Wu, W. Wang, Phys. Chem. Chem. Phys., 2006, **8**, 1096 – 1104.
20. X. Zhong, Z. Liu, D. Cao, J. Phys. Chem. B, 2011, **115**, 10027 – 10040.
21. T. Youngs, C. Hardacre, Chem. Phys. Chem., 2008, **9**, 1548 – 1558.
22. T. Yan, C. Burnham, M. Del Popolo, G. Voth, J. Phys. Chem. B, 2004, **108**, 11877 – 11881.

23. T. Yan, T. Wang, C. Knox, J. Phys. Chem. B, 2010, **114**, 6886 – 6904.
24. T. Yan, T. Wang, C. Knox, J. Phys. Chem. B, 2010, **114**, 6905 -6921.
25. T. Chang, L. Dang, J. Phys. Chem. A, 2009, **113**, 2127 – 2135.
26. C. Schrönder, O. Steinhauser, J. Chem. Phys., 2010, **133**, 2127 – 2135.
27. H. Nakano, T. Yamamoto, S. Kato, J. Chem. Phys., 2010, **132**, 44106.
28. M. Tanaka. H. Siehl, Chem. Phys. Lett., 2008, **457**, 263 – 266.
29. T. Koddermann, D. Paschek, R. Ludwig, Chem. Phys. Chem., 2007, **8**, 2464 - 2470.
30. J. Canongia Lopes, A. Padua, J. Phys. Chem. B, 2004, **108**, 16893 – 16898.
31. Y. Wang, S. Izvekov, T. Yan, G Voth, J. Phys. Chem. B. 2006, **110**, 3564 – 3575.
32. B Bhargava, R. devane, M. Klein, S. Balasubramanian, Soft Matter, 2007, **3**, 1395 – 1400.
33. B. Bhargava, S. Balasubramanian, M. Klein, Chem. Commun., 2008, 3339 – 3351.
34. Y. Zhong, E. Maginn, J. Phys. Chem. B, 2012, **116**, 10036 – 10048.
35. C. Schroder, Phys. Chem. Chem. Phys., 2012, **14**, 30089 -3102.
36. I. V. Leontyev, A. A. stucherbrukhov, J. Chem. Phys., 2009, **130**, 85102.
37. V. Chaban, Phys. Chem.Chem. Phys., 2011, **13**, 16055 – 16062.
38. F. Dommert, K. Wendler, R. Berger, L. D. Site, C. Holm, Chem. Phys. Chem., 2012, **13**, 1625 – 1637.
39. J. Canongia Lopes, J. Deschamps A. Padua, J. Phys. Chem. B, 2004, **108**, 2038 – 2047.
40. J. N. Canongia Lopes, A. Padua, J. Phys. Chem. B, 2006, **110**, 19586 – 19592.
41. O. Borodin, J. Phys. Chem., 2009, **113**, 11463 – 11478.
42. J. N. Canongia Lopes, A. A. H. Padua, K. Shimizu, J. Phys. Chem. B, 2008, **112**, 5039 – 5046.
43. J. N. Canongia Lopes, K. Shimnizu, A. A. Padua, Y. Umebayashi, S. Fukuda, K. Fujii, S. I. Ishiguro, J. Phys. Chem. *B,* 2008, **112**, 1465 – 1472.
44. J. N. Canongia Lopes, A. A. Padua, J. Phys. Chem. *B* 2006, **110**, 3330–3335.
45. S. V. Sambasivarao, O. Acevedo, J. Chem. Theory Comput. 2009, **5**, 1038–1050.
46. V. V. Chaban, I. V. Voroshylova, O. N. Kalungin, Phys. Chem. Chem. Phys., 2011, **13**, 7910 – 7920.
47. Z. Liu, S. Huang, W. Wang, J. Phys. Chem. B, 2004, 108, 12978 –12989.
48. M. Klahn, A. Seduraman, P. Wu, J. Phys. Chem. B, 2008, **112**, 10989 – 11004.

49. C. Krekeler, F. Dommert, J. Schmidt, Y. Y. Zhao, C. Holm, R. Berger, L. Delle Site, Phys. Chem. Chem. Phys., 2010, 12, 1821 -1821.

CHAPTER 3

Computational details

3.1 Introduction

The theoretical methods used to model the physical properties of a system consist of three broad categories namely: Quantum Mechanics (QM), Empirical Force Field Models (Classical Mechanics) and a hybrid of Quantum Mechanics with Molecular Mechanics (QM/MM) [1].

When selecting a theoretical approach to solve a problem, there are a number of factors that one needs to consider such as the size of the problem, the level of accuracy required and as well as the costs attributed to the selected method.

In this section we present a comprehensive discussion of all the computational details and the theory of the methods employed in this study. We will start off the discussion with a description of quantum mechanical methods, followed by molecular mechanics/dynamics including a brief overview of optimisation techniques. This is followed by a discussion of hybrid QM/MM methods. The chapter closes off by discussing the calculation of structural and transport properties using molecular dynamics simulation.

3.2 Background to Quantum Mechanics

Quantum Mechanics (QM) provides the most accurate first principles methods for describing chemical systems. QM methods are implemented in electronic structure programs such as Gaussian [2] and GAMESS-UK [3], both of which have been used in this project. These methods explicitly model the electrons in atomic and molecular systems with the aid of the Schrödinger equation.

The time-dependent Schrödinger equation can be written as:

$$\left\{\frac{-\hbar^2}{2m}\nabla^2 + \mathcal{V}\right\}\Psi(\boldsymbol{r},t) = i\hbar\frac{\partial\Psi(\boldsymbol{r},t)}{\partial t} \qquad \text{Eq 3.1}$$

Where $$\nabla^2 = \frac{\partial^2}{\partial x^2} + \frac{\partial^2}{\partial y^2} + \frac{\partial^2}{\partial z^2} \qquad \text{Eq 3.2}$$

To solve the Schrödinger equation one requires a number of postulates [4]. If we postulate that energy $\mathcal{V}$ does not depend on time we can consider the time independent Schrödinger equation, which is expressed as:

$$\left\{\frac{-\hbar^2}{2m}\nabla^2 + \mathcal{V}\right\}\Psi(\boldsymbol{r}) = E\Psi(\boldsymbol{r}) \qquad \text{Eq 3.3}$$

which only depends on the spatial terms/coordinates.

The left hand side of equation 3.3 is usually abbreviated to $\hat{\mathrm{H}}\Psi$, where $\hat{\mathrm{H}}$ is the Hamiltonian operator:

$$\hat{\mathrm{H}} = \frac{-\hbar^2}{2m}\nabla^2 + \mathcal{V} \qquad \text{Eq 3.4}$$

The Hamiltonian operator is made up of two terms, a kinetic and potential energy term. The kinetic energy term is:

$$\frac{-\hbar^2}{2m}\nabla^2 \qquad \text{Eq 3.5}$$

and the potential energy term, $\mathcal{V}$, is given by:

$$\mathcal{V} = \frac{1}{4\pi\varepsilon_0 r}\left(-\sum_{i}^{electrons}\sum_{I}^{nuclei}\left(\frac{Z_I e^2}{|R_I - r_i|}\right) + \sum_{i}^{electrons}\sum_{j<i}^{electrons}\left(\frac{e^2}{|r_i - r_j|}\right) + \sum_{i}^{nuclei}\sum_{j<i}^{nuclei}\left(\frac{Z_I Z_j e^2}{|R_I - R_j|}\right)\right) \qquad \text{Eq 3.6}$$

Where Z is the number of protons and *e* is the fundamental charge. The potential energy expression is made up of electrostatic interactions between nuclei, between electrons and between electrons and nuclei.

The Schrödinger equation can be solved exactly for only a few problems, which include a particle in a box, the harmonic oscillator, particle on a ring, particle on a sphere and the hydrogen atom. Imposing restrictions known as boundary conditions [4] allows for this problem to be solved. For molecular systems no exact solution of the Schrödinger equation can be found instead we obtain an approximation of the true solution by ignoring the electron-electron repulsion [4].

3.2.1 The Born-Oppenheimer approximation

It has been noted that the Schrödinger equation can be solved exactly for a molecular system; with aid of the Born-Oppenheimer approximation [5] it is possible to solve this equation. Here the nuclear kinetics are ignored, justifiable by the fact that electrons are lighter and thus possess motion which is far greater than that of protons. Electrons can be expected to instantaneously adjust to the nuclear coordinates of a molecule thus the effective energy of a molecule is [1]:

$$\hat{\mathrm{H}}^{elec}\Psi^{elec}(r,R) = E^{eff}(R)\Psi^{elec}(r,R) \qquad \text{Eq 3.7}$$

where the wavefunction depends on the position of the nuclei (R) and electrons (r). The electronic Hamiltonian is as before a sum of the kinetic and potential energy, where the kinetic energy is:

$$\left(\frac{-\hbar^2}{2m}\right)\sum_i^{electrons}\left(\frac{\partial^2}{\partial x_i^2}+\frac{\partial^2}{\partial y_i^2}+\frac{\partial^2}{\partial z_i^2}\right) \qquad \text{Eq 3.8}$$

and the potential energy is as shown in equation 3.6

3.2.2 Molecular Orbital Theory

Extension of the wavefunction to molecules requires the introduction of molecular orbitals (MO) theory. Molecular orbitals are used to approximate the complete wavefunction, where each spatial orbital, Ψ (x,y,z), depends upon the Cartesian coordinates of a single electron [1].

In most QM calculations performed for molecular systems, each molecular spin orbital is expressed as a linear combination of atomic orbitals. It follows that each MO can be written as a summation of the form:

$$\psi_i = \sum_{\mu=1}^{K} c_{\mu i}\phi_u \qquad \text{Eq 3.9}$$

where ϕ_u are the N basis functions and $c_{\mu i}$ are the molecular orbitals expansion coefficients. Which effectively means that atomic orbitals can and are represented by a combination of basis functions, which could either be of Slater-type atomic (STO's) or Gaussian-type (GTO's) atomic orbitals [1, 13].

3.2.3 The Hartree-Fock Model

The Hartree-Fock model utilizes two crucial ideas, which are the variantional theorem and the Roothaan-Hall equations. The model also makes use of Slater determinants and introduces an effective potential (The Self-consistent field).

3.2.3.1 The Variational theorem

In the variational theorem it is stated that the energy calculated from an approximation to the true wavefunction will always be greater than or equal to the "true" energy [1].

$$E' = \int \Xi^* \hat{\mathrm{H}} \Xi d\tau \geq E_0 \qquad \text{Eq 3.9}$$

where E_0 is the true energy.

The best guess or solution to a single-determinant wavefunction can be obtained by minimizing the energy with respect to the molecular orbital coefficients. When the Schrödinger equation is solved by integrating over all space with a trial wavefunction Ξ the value for the energy *E'* is:

$$E' = \frac{\int \Xi^* \hat{H} \Xi d\tau}{\int \Xi^* \Xi d\tau} \qquad \text{Eq 3.10}$$

for a normalised wavefunction:

$$E' = \int \Xi^* \hat{H} \Xi d\tau \qquad \text{Eq 3.11}$$

If the initial guess of the wavefunction, Ξ, is the true wavefunction, Ψ, then the actual energy is calculated [6]:

$$E' = \int \Psi^* \hat{H} \Psi d\tau \qquad \text{Eq 3.12}$$

3.2.3.2 The Roothaan-Hall equations

The Roothaan-Hall equations are derived by variationally optimizing a Slater determinant wavefunction and subsequently writing the wavefunction as a linear combination of atomic orbitals. The derivation is done for closed-shell system (systems with no unpaired electrons) [1]. For open-shell systems (systems with unpaired electrons) the equivalent equations are the Pople-Nesbit equations. Hartree-Fock theory in conjunction with a closed-shell single determinant is used for molecules in their ground state and is commonly known as the Restricted Hartree-Fock (RHF) theory. The standard form of the Fock matrix, which represents the average field effects of all the electrons on an orbital in the Roothaan-Hall equations is shown in equation 3.13

$$F_{\mu\nu} = H_{\mu\nu}^{core} + \sum_{\lambda=1}^{K} \sum_{\sigma=1}^{K} P_{\lambda\sigma} \left[(\mu\nu|\lambda\sigma) - \frac{1}{2} (\mu\nu|\lambda\sigma) \right] \quad \text{Eq 3.13}$$

For a full description of the on how to solve the Roothaan-Hall equations see: *Molecular Modelling: Principles and Applications* [1].

3.2.3.3 Self-Consistent field

The procedure for solving the Roothaan-Hall equations is called the Self-Consistent Field (SCF) method. The equations are solved iteratively and converge to the minimum energy; if the orbitals are self-consistent they will generate a field, which would produce the same orbitals [1].

3.2.3.4 Choosing a basis set

In order to solve the total electronic wavefunction, the approximate wave function is represented as a linear combination of atomic orbitals. A mathematical description of each atomic orbital is formulated and included into a set known as the basis set [13].

If an integration is carried out over all space, the probability of finding an electron is unity, meaning that an electron has a finite probability to exist anywhere in space. A basis set describes the orbitals that are available for the occupation of electron and the less restrictive the basis set is the more accurately the electrons are described [13].

In chemistry it possible to form a set of functions for the electrons, these function must meet both mathematical and physical constraints thus one must choose a physically sensible group of functions to represent the electrons in the simulation under study.

3.2.3.5 Density Functional Theory

The Schrödinger equation allows one to calculate the energy once the Hamiltonian has been defined. As described in section 3.2, the electronic Hamiltonian is a function of the number of electrons, their positions and the charges on the nuclei. This information can also be obtained from the electron density, in turn making the energy a function of the density, which is a function of the electronic positions (Density Functional Theory) [16].

The energy density functional $E[\rho(\boldsymbol{r})]$ is unique for unique densities, obeys the variational theorem and can be obtained via a 1-electron functional,

$$E[\rho] = d\boldsymbol{r}\rho(\boldsymbol{r})v(\boldsymbol{r}) \qquad \text{Eq 3.13}$$

where $v(\boldsymbol{r}) = \frac{\partial E[\rho(\boldsymbol{r})]}{\partial \rho(\boldsymbol{r})}$

thus the exact energy can be expressed in terms of orbitals

$$E[\rho] = \sum_{i=1}^{N} \langle \phi_i(\boldsymbol{r}) | v(\boldsymbol{r}) \phi_i(\boldsymbol{r}) \rangle \qquad \text{Eq 3.14}$$

Using the SCF procedure we can find orbitals that correspond to the lowest energy, the only difference being that in this method the Fock operator is represented as follows:

$$F^{KS}\phi_i^{KS} = \varepsilon_i^{KS}\phi_i^{KS} \qquad \text{Eq 3.15}$$

This is known as the Kohn-Sham (KS) SCF procedure and as in the RHF SCF method the orbitals are represented by a basis set.

3.3 Molecular Mechanics Methods

The success of any computational study of a chemical system can be attributed to the quality of the mathematical model employed to calculate the potential energy of the system under investigation. Depending on the size of a system and the property under investigation one can use either the Quantum Mechanical (QM) approach or the Molecular Mechanics (MM) approach. In the MM approach, a set of mathematical equations is used to describe the physical interactions that mandate the structure and dynamic properties within a chemical system.

3.2.1 Force fields

A force field is generated by a combination of potential energy functions that adequately describes the intra and intermolecular interactions of a system.

3.2.2 Molecular Mechanics Potential Energy Functions

A potential energy function is a mathematical equations that is used to calculate the potential energy of a system as a function of its three-dimensional structure. The equation consists of terms that describe the various physical interactions that mandate both the structure and the dynamics of a system. The physical interactions within a system can be broke down in two parts, namely intramolecular and intermolecular interactions

Intramolecular:

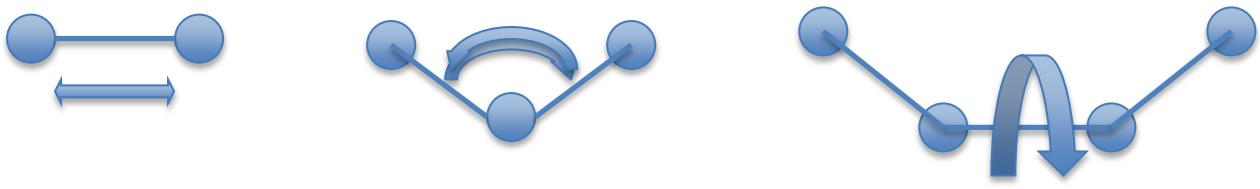

(a) (b) (c)

Figure 3.1: Schematic representation of the types of bonding interactions within a molecule (a) bond stretching (b) bond angles and (c) rotational torsion angle.

$$v(r) = \sum_{bonds} k_b(r - r_0)^2 + \sum_{angles} k_\theta(\theta - \theta_0)^2 + \sum_{dihedrals} k_x[1 + cos(n_0\chi - \delta_0)] + \sum_{impropers} k_\psi(\psi - \psi_0)^2$$

Eq 3.16

Intermolecular:

(a) (b)

Figure 3.2: Schematic representation of the types interactions between molecules (a) electrostatic interactions and (b) van der Waals interactions.

$$v(r) = \sum_{i=1}^{N-1} \sum_{j=i+1}^{N} \left\{ 4\epsilon_{ij} \left[\left(\frac{r_{min,ij}}{r_{ij}} \right)^{12} - \left(\frac{r_{min,ij}}{r_{ij}} \right)^{6} \right] + \frac{q_i q_j}{r_{ij}} \right\}$$

Eq 3.17

Equations 3.16 and 3.17 above represent the internal and external terms of any molecule respectively. For terms such as bond lengths, $\boldsymbol{k_b}$; valence angles, $\boldsymbol{\theta}$; torsion or dihedral angle, $\boldsymbol{\chi}$; and the improper rotation, $\boldsymbol{\psi}$; in equation 3.16 and 3.17, their values can be deduced from either experimental result generated by Crystallography or Nuclear Magnetic Resonance (NMR) spectroscopy, a structure generated during a

Monte Carlo (MC) simulation or Quantum mechanical (QM) calculations. The remaining terms in the equations, known as parameters, are associated with the particular atom type and the types of atom that that atom is covalently bonded to. These terms allow for correct treatment of different atoms and their different connectivity's without changing the equation.

It follows that the accuracy of how the physical interactions are treated is dependent on the parameters used in the potential energy functions above. The complete potential energy function is shown in equation 3.18

$$U = U_{bonds} + U_{angles} + U_{dihedrals} + U_{impropers} + U_{van\ der\ Waals} + U_{electrostatic}$$

Eq 3.18

3.4 Molecular Dynamics

Upon obtaining a potential energy function and developing force fields that are satisfactory, it is then possible to generate configurations of a system in a suitable ensemble. In the Molecular Dynamics (MD) approach, equations 3.19 and 3.20, the Newton's equations of motion are integrated simultaneously, over time, for all the atoms that exists within a system

$$\frac{d^2 r_i(t)}{dt^2} = \frac{F_i}{m_i} \qquad \text{Eq 3.19}$$

$$F_i = -\frac{\partial V(r_i, r_{i+1}, \ldots r_N)}{\partial r_i} \qquad \text{Eq 3.20}$$

where F_i is the force on atom *i* that has a mass m_i and *t* the time. The gradient of the potential energy, *V(r),* gives the force. Various algorithms have been used to integrate the equations of motion in MD. Integrators used in this study are discussed below.

3.4.1 Integrating the Equations of Motion

The most computationally demanding part of a molecular dynamics simulation is the calculation of the forces at every time step. In addition to be being as fast as possible, the chosen algorithm has to allow for long integration time steps with the smallest numerical error possible.

The most commonly used algorithm to integrate the equations of motion is that described by Verlet in 1967. Unfortunately this algorithm experiences some shortcomings when generating trajectories. This comes about through the addition of a small term to a difference of large terms giving rise to numerical imprecision [1]. Schemes have been suggested to account for the inefficiencies of the original Verlet algorithm, examples of such integrators include schemes such as the leapfrog algorithm, Velocity Verlet and the "New" Velocity Verlet algorithm implemented in CHARMM. The leapfrog and the CHARMM's Velocity Verlet algorithm were used in this study and are discussed in the following section.

3.4.1.1 Verlet leapfrog integration algorithm

The leap-frog algorithm uses the relationship between position **r**(t), mid time-step velocity $\mathbf{v}\left(\mathrm{t}-\frac{1}{2}\delta\mathrm{t}\right)$and acceleration **a**(t) of an atom in the following manner,

$$\boldsymbol{r}(t+\delta t)=\boldsymbol{r}(t)+\delta t\boldsymbol{v}\left(t+\tfrac{1}{2}\delta t\right) \qquad \text{Eq 3.21}$$

$$\boldsymbol{v}\left(t+\tfrac{1}{2}\delta t\right)=\boldsymbol{v}\left(t-\tfrac{1}{2}\delta t\right)+\delta t\boldsymbol{a}(t) \qquad \text{Eq 3.22}$$

$\boldsymbol{v}\left(t+\frac{1}{2}\delta t\right)$ is evaluated first after which the velocities are leaped over the coordinates to give the next mid-step values $v\left(1-\frac{1}{2}\delta\mathrm{t}\right)$. The velocities at this step are then calculated using equation 3.22 [7]:

$$v(t)=\tfrac{1}{2}\left(v\left(t+\tfrac{1}{2}\delta t\right)+v\left(t-\tfrac{1}{2}\delta t\right)\right) \qquad \text{Eq 3.23}$$

This is necessary as the energy at time *t* must be calculated, likewise any other variables that require both the system coordinates and velocities at the same time. $\boldsymbol{r}(t+\delta t)$ is then used to leap the coordinates over the velocities, now the new accelerations may be calculated for the next step.

3.4.1.2 The CHARMM Velocity Verlet integrator

The CHARMM Velocity Verlet (VV2) integrator is a type of Verlet integrator that integrates the equations of motion using explicit reversible integrators. It is derived from classical propagators using the operator factorisation or operator splitting techniques. [8] This splitting technique results in a process where a system is evaluated using the velocity-verlet integration at small time step ∂t for *n* steps under the influence of an arbitrary reference force $\boldsymbol{F}^{ref}$. The computationally expensive true force **F**, is evaluated only every *n* steps at a larger time step Δt with the integrator being applied as follows:

$$\boldsymbol{r}(\Delta t) = \boldsymbol{r}_{\boldsymbol{VV}}^{ref}\left[\boldsymbol{r}(0), \boldsymbol{v}(0) + \frac{\Delta t}{2}\left[\frac{\boldsymbol{F}(0) - \boldsymbol{F}^{ref}(0)}{m}\right]; n, \partial t\right] \qquad \text{Eq 3.24}$$

$$\boldsymbol{v}(\Delta t) = \boldsymbol{v}_{\boldsymbol{VV}}^{ref}\left[\boldsymbol{r}(0), \boldsymbol{v}(0) + \frac{\Delta t}{2}\left[\frac{\boldsymbol{F}(0) - \boldsymbol{F}^{ref}(0)}{m}\right]; n, \partial t\right] + \frac{\Delta \boldsymbol{t}}{\boldsymbol{2}}\left[\frac{\boldsymbol{F}(\Delta t) - \boldsymbol{F}^{ref}(\Delta t)}{m}\right] \qquad \text{Eq 3.25}$$

The VV2 integration procedure starts with an initial velocity condition, which is modified by the difference between the true force and the reference force, which is the force at the beginning of each large step. The velocities obtained from the integration must be modified by the difference between the reference force and the true evaluated force at the end of the large time step.

This algorithm is implemented in CHARMM for the use in polarisable force fields that are based on Drude oscillator model. For further details on the integrator method the reader is directed to reference 8.

3.4.2 Periodic boundary Conditions

Molecular dynamics simulations may be used to predict bulk properties from a simulation that contains only a fraction of the particles that a physical sample would contain. This is carried out by simulating a small sample of molecules, in the case of ionic liquids ions, contained in a cubic simulation box. Other space-filling box shapes may also be used [7]. A major shortcoming of this is that particles at the edge of the simulation box may leave the defined simulation box completely leaving fewer particles in the systems. In addition the atoms at the edge of the box may start to experience forces that are different to those experienced by particles in the bulk system. The above-mentioned issues are known as edge effects and can be accounted for by the use of periodic coundary conditions (PBC).

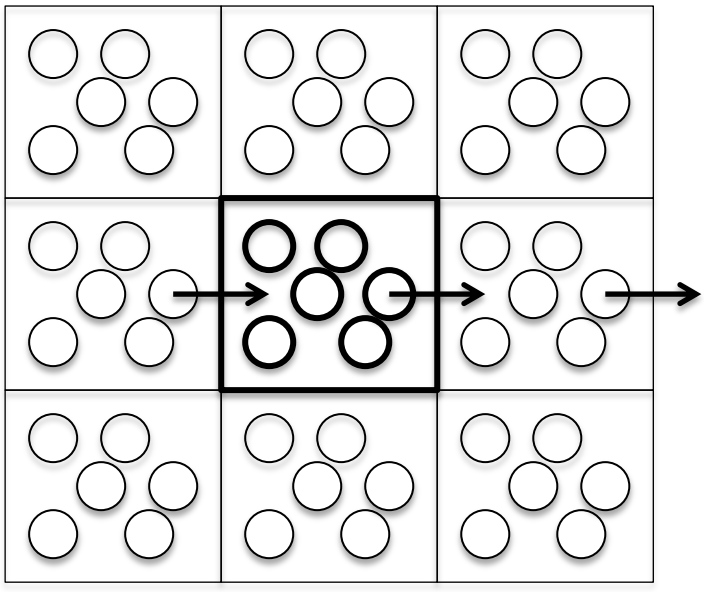

Figure 3.3: Schematic representation of periodic boundary conditions. The central shaded box represents a simulation box, which is surrounded by its periodic images. The arrows shows an instance were an atom exits the simulation box and it re-enters the simulation box in the opposite side with the same energy and velocity.

A particle that leaves the simulation box is accounted for by creating an image of the particle that has just left the simulation box [9]. The imaged particle re-enters the simulation box in the opposite side with the same velocity.

3.4.3 Potential Truncation

During a molecular dynamics simulation, the potential energy of each atom within the system under study is calculated. This can be time consuming depending on the number of atoms present in the system. As such, potential cutoffs in combination with smoothing functions are used.

3.4.3.1 Cutoffs

Non-bonded van der Waals and electrostatic interactions are treated with cutoffs and the application of periodic boundary conditions (section 3.4.3). The latter treatment requires that the minimum image convention be applied. This assures that a molecule does not see itself and interacts with only the closest (taking into account periodic images) remaining molecules in the system. A typical cutoff radius is between 9 and 12 Å, a fitting distance as the pair potential is neglected at this distance.

Simply cutting off the potential where it is non-zero can introduce significant errors, since the potential of the system will no longer be continuous, disrupting the conservation of the total energy. To avoid the above from occurring, smoothing or switching functions can be used.

3.4.3.2 Smoothing and Switching Functions

There are two methods that are commonly used to truncate the potential to zero, equations 3.26 and 3.27, the "switching" and "shifting" functions, respectively

$$S_f(r_{ij}) = \begin{cases} \left(1 - \frac{2r_{ij}^2}{r_{cut}^2} + \frac{r_{ij}^4}{r_{cut}^4}\right) & r_{ij} < r_{cut} \\ 0 & r_{ij} > r_{cut} \end{cases} \qquad \text{Eq 3.26}$$

$$S_w(r_{ij}) = \begin{cases} 1 & r \leq r_{on} \\ \frac{(r_{off}-r_{ij})^2(r_{off}+2r_{ij}-3r_{on})}{(r_{off}-r_{on})^3} & r_{on} < r_{ij} \leq r_{off} \\ 0 & r > r_{off} \end{cases} \quad \text{Eq 3.27}$$

A shifting function modifies the interaction potential over the complete range to the cutoff distance and assures that it approaches zero smoothly at the cutoff distance and is zero beyond. A switching function only adjusts the potential between an elected "cuton" and "cutoff" distances. The interaction potential is unaffected for distances less than the "cuton" distance and is zero for distances greater than the "cutoff "distance [20]. In general, the normal interaction gets multiplied by these functions in order to truncate the potential to zero.

3.4.3.3 The Ewald Summations

The most effective technique for computing the electrostatics of an MD simulation is the Ewald summation method [1]. The Ewald method is used for the treatment of long-range interactions in periodic systems, which play a vital role in the simulation of charged species.

In this method, a particle interacts with all other particles in the simulation including those imaged in periodic cells. All pairs of charges in a simulation box have a charge-charge contribution to potential energy, which can be represented as follows:

$$\mathcal{V} = \frac{1}{2}\sum_{i=1}^{N}\sum_{j=1}^{N}\frac{q_i q_j}{4\pi\varepsilon_0 r_{ij}^o} + \sum_n \sum_{i=1}^{N}\sum_{j=1}^{N}\frac{q_i q_j}{4\pi\varepsilon_0 |r_{ij}^o + \mathbf{n}L|} \quad \text{Eq 3.28}$$

The first term accounts for interactions within the central box, and the second term represents interactions between atoms in the central box and their images and between atoms in various periodic replicas [9]. Here r_{ij}^o is the minimum image distance, L is the box length and **n** splits into $\mathbf{n}_x$, $\mathbf{n}_y$ and $\mathbf{n}_z$ and represents unit vectors to all periodic boxes around the central box

The summation procedure tends to be cumbersome due to the number of charges that interact with each other in the simulation box and it surrounding periodic images. Thus when calculating the Ewald sum the trick is to break up the summation into two series based on the identity:

$$\frac{1}{r} = \frac{f(r)}{r} + \frac{1-f(r)}{r} \qquad \text{Eq 3.29}$$

The point being, one has to choose a suitable function, $f(r)$, which can deal with the rapid changes of $\frac{1}{r}$ at short r and the slow decay at long r. The potential energy charge-charge contribution thus becomes:

$$\mathcal{V} = \frac{1}{2}\sum_{i=1}^{N}\sum_{j=1}^{N}\begin{cases} \sum_{|n|=0}^{\infty}\frac{q_i q_j}{4\pi\varepsilon_0}\frac{\operatorname{erfc}(\alpha|r_{ij}+n|)}{|r_{ij}+n|} + \\ \sum_{k\neq 0}\frac{1}{L^3}\frac{q_i q_j}{4\pi\varepsilon_0}\frac{4\pi^2}{k^2}\exp\left(-\frac{k^2}{4\alpha^2}\right)\cos\left(k.r_{ij}\right) - \\ \frac{\alpha}{\sqrt{\pi}}\sum_{k=1}^{N}\frac{q_k^2}{4\pi\varepsilon_0} + \frac{2\pi}{3L^3}\left|\sum_{k=1}^{N}\frac{q_k}{4\pi\varepsilon_0}r_k\right|^2 \end{cases} \qquad \text{Eq 3.30}$$

because each charge in a system, treated with the Ewald method, is considered to be surrounded by a neutralization charge distribution, which has the same magnitude but bears an opposite charge, the sum over the charges is converted to a sum of interactions that exist between the charges and the neutralisation distributions [1]. To this a second neutralisation distribution, which counteracts the first neutralisation distribution, is added and a self-term subtracted. A forth correction term;

$$\mathcal{V} = \frac{2\pi}{3L^3}\left|\sum_{k=1}^{N}\frac{q_k}{4\pi\varepsilon_0}r_k\right|^2 \qquad \text{Eq 3.31}$$

may be required if the medium surrounding the simulation box is a vacuum, however, the term is not required if the medium is a conductor.

3.4.4 Constrained Dynamics

Constraint Dynamics allow for selected coordinates to be kept fixed during a simulation whilst not interfering with the other degrees of freedom. This method is typically used for bond vibrations involving very light atoms such as the hydrogen atom. These light atoms vibrate at a very high frequency limiting the timestep to be used in a molecular dynamic simulation. Due to these high frequency motions being of very little significance in contrast to their lower frequency counterparts they are kept fixed.

Ryckaert, Cicootti and Berendesen's SHAKE algorithm is one of the most commonly used constraint method in molecular dynamics [14]. SHAKE is a technique developed to treat the dynamics of a molecular system where a selected degree of freedom, such as a bond, is to be constrained while the other degrees of freedom are free to evolve under the influence of the interactions that exists within the system.

The most common use of the SHAKE algorithm is in constraining bonds that involve the hydrogen atom, which tend to vibrate at very high frequency in comparison to other bonds in a system [1].

3.4.5 Simulation Ensemble

In molecular dynamics simulations four types of statistical ensembles are typically used, these are the canonical (constant N, V and T); the microcanonical (constant N, V and E); the grand-canonical (constant μ, V and T) and the isothermal-isobaric (constant N, P and T), where N is the number of particles, V the volume, P the pressure, T the temperature, E the energy and μ the chemical potential.

In each ensemble the mentioned thermodynamic variables are specified and are kept constant while the other thermodynamic quantities must be determined by ensemble averaging. Fluctuations from the ensemble average are possible and have been shown to be crucial for the calculation of certain thermodynamic parameters such as heat capacities, etc. [1].

Computer simulations are of great value and are deemed to be more trust worthy when they can be compared to experiments. Thus the most obvious choice would be to either run simulations in the canonical, constant-NVT, or the isothermal-isobaric, constant-NPT, ensemble. Various methodologies have been used to implement these ensembles [1].

3.5 Hybrid simulations (QM/MM)

To date QM calculations are not feasible for large systems and MM methods cannot always provide the level of accuracy required for every given calculation. To overcome the shortcomings of both methods a combined QM/MM approach may be used, this approach is ideal for systems where electronic effects are likely to exist and a pure QM approach would be too computationally expensive to apply.

This approach is implemented with the following Hamiltonian [13]:

$$H_{effective} = H^{0}_{QM} + H_{MM} + H^{Elec}_{QM/MM} + H^{vdW}_{QM/MM} + H_{boundary} \qquad \text{Eq 3.32}$$

and the energy is evaluated as:

$$E_{total} = E_{QM} + E_{MM} + E_{QM/MM} + E_{boundary} \qquad \text{Eq 3.33}$$

each of the Hamiltonian terms describe potentials of different parts of the system and the term $H_{boundary}$ is used to account for bulk effects and is the periodic boundary term applied in Molecular dynamics (MD).

In order to account for the environmentally induced relaxation of the QM wavefunction $H^{Elec}_{QM/MM}$ is separated into parts;

$$H^{Elec}_{QM/MM} = \sum_{i}^{Solute\ electrons} \sum_{m}^{MM\ Atoms} \frac{q_m}{r_{im}} + \sum_{k}^{solute\ nuclei} \sum_{m}^{MM\ Atoms} \left[\frac{Z_k q_m}{r_{km}} + 4\varepsilon_{km} \left(\frac{\sigma^{12}_{km}}{r^{12}_{km}} - \frac{\sigma^{6}_{km}}{r^{6}_{km}} \right) \right]$$

Eq 3.34

an operator acting on the QM electrons $\sum_{i}^{Solute\ electrons}\sum_{m}^{MM\ Atoms}\frac{q_m}{r_{im}}$ and the classical term for the interaction of MM atoms with the solute nuclei.

For a more detailed description of this approach see: *A combined quantum mechanical and molecular mechanical potential for Molecular dynamics simulations* [13]

For the calculations carried out in this study Semi Empirical methods were used to model the quantum mechanical region of a QM/MM simulation. These simulations were achieved by interfacing GAMESS-UK with CHARMM.

3.6 The Drude Oscillator Model – Theory

In accordance to the classical Drude oscillator model, polarisability is introduced by the addition of massless charge particles to each polarisable atom within a molecule [14]. The massless charge is attached to an atom by a harmonic spring, as illustrated in figure 3.4, creating a finite induced dipole as the partial atomic charge is redistributed between the Drude particle and its "parent atom" [14].

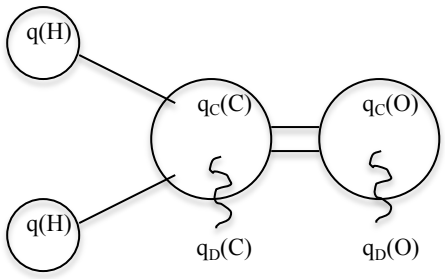

Figure 3.4: A classical Drude oscillator model using a Methanal molecule as an example. The hydrogen molecules are made non-polarisable and the displacement of the carbon and oxygen Drude particles is exaggerated for visualization purposes.

The displacement of the Drude particle in a molecular dynamics simulation is determined self-consistently by finding the minimum energy uniform with the Born-Oppenheimer approximation [14]. For a Drude particle in its equilibrium position, the polarisability of atom X, α(X), is related to the charge $q_D(A)$ through the equation,

$$\alpha(X) = \frac{q_D^2(X)}{k_D} \qquad \text{Eq 3.35}$$

where k_D is the force constant of the harmonic spring connecting a Drude particle to its "parent atom". The force constant is chosen such that the particles remain displaced and so that the whole term is equal to the point-dipole, associated with the atom-Drude pair [17].

A major advantage of using the Drude oscillator model for the explicit inclusion on polarisation is that the simple functional form of the additive force field, discussed in section 3.2.2, is preserved.

$$\mathrm{U} = \mathrm{U_{bonds}} + \mathrm{U_{angles}} + \mathrm{U_{dihedrals}} + \mathrm{U_{impropers}} + \mathrm{U_{van\ der\ Waals}} + \mathrm{U_{electrostatic}} \qquad \text{Eq 3.36}$$

The electrostatic energy, $\mathrm{U_{electrostatic}}$, in the polarisable model is substituted by a Coulombic energy terms which describe interactions between the Drude particles, the core parent atoms and as well as the self-energy of polarisable atom treated via a harmonic term and thus $\mathrm{U_{electrostatic}}$ becomes,

$$\mathrm{U_{elec}} = \sum_{A<B}^{N} \frac{q_C(A)\cdot q_C(B)}{|r(A)-r(B)|} + \sum_{A<B}^{N,N_D} \frac{q_D(A)\cdot q_C(B)}{|r_D(A)-r(B)|} + \sum_{A<B}^{N_D} \frac{q_D(A)\cdot q_D(B)}{|r_D(A)-r_D(B)|} + \frac{1}{2}\sum_{A}^{N_D} k_D |\, r_D(A) - r_D(B)|^2 \qquad \text{Eq 3.37}$$

N and N_D are the number of real atoms and Drude particles, respectively, likewise q_C and q_D are the charges on each and **r** and $\mathbf{r}_D$ are the positions of the parent atom and the Drude particles. With the aid of equation 3.37 one can perform MD simulations with only minor changes in the existing packages as the original functional form stay essentially unchanged.

During the MD simulation the Drude particle position for every configuration has to be self-consistently adjusted at each step, which is inefficient and computationally expensive [15]. To overcome this an MD algorithm based on an extended langrangian formalization [16,17] is implemented. In the formalization, a relatively small mass is assigned to a Drude particle and a low temperature thermostat controls the oscillations of the particle, [18] alleviating the inefficient and costly parts of the technique.

3.7 Calculating Thermophysical properties of Room Temperature Ionic Liquids from molecular dynamics simulations

3.7.1 Radial Distribution functions

Radial distribution functions (RDFs) are a useful means of reporting the fluid structure of a liquid. RDFs, g(r), give the probability of finding a pair of atoms separated by a distance *r*, relative to the probability expected for a completely random distribution at the same density. The equation defining the RDF between a pair of atoms in a spherical volume element is as follows:

$$\frac{1}{V} g_{ab}(r) = \frac{1}{N_a N_b} \left\langle \sum_{i=1}^{N_a} \sum_{j=1}^{N_b} \delta[r - r_{a_i b_j}] \right\rangle \qquad \text{Eq 3.38}$$

where V is the volume of the spherical shell, N is the total number of atoms within the volume of the shell, δ is the dirac delta function and r is the radial distance [14]. The double summation accounts for all *a* and *b* pairs separated by distance **r**. The integration of equation 3.38 over the full spherical volume yields

$$\frac{1}{V} \int g_{ab}(r) = \frac{1}{N_a N_b} \left\langle \sum_{i=1}^{N_a} \sum_{j=1}^{N_b} \int \delta\,[r - r_{a_i b_j}] \right\rangle \qquad \text{Eq 3.39}$$

the integral of the Dirac function is unity and $\frac{1}{V}$ is the normalisation constant for g. It thus follows that equation 3.39 may be read as a probability function and the probability of finding atoms *a* and *b* within range **Δr** from **r** is expressed as follows:

$$P\{a,b,r,\Delta r\} = \frac{4\pi r^2}{V} g_{ab}(r)\Delta r \qquad \text{Eq 3.40}$$

Thus $g(r) = 1$ indicates no order (a random distribution), while $g(r) > 1$ indicates a local ordering and $g(r) < 1$ indicates a depletion at a given separation r. Figure 3.5 shows an example of a cation-cation, anion-anion and cation-anion radial distribution function at 333.15 K and 1 atm for 1-butyl-3-methylimidazolium hexaflourophosphate. This example shows that cation–anion pairs tend to order in a first solvation shell at a separation of about 3.8 Å. Subsequent cation–anion solvation shells occur at 5.9 and 10 Å and the same type of ordering is observed amongst the cations and anions.

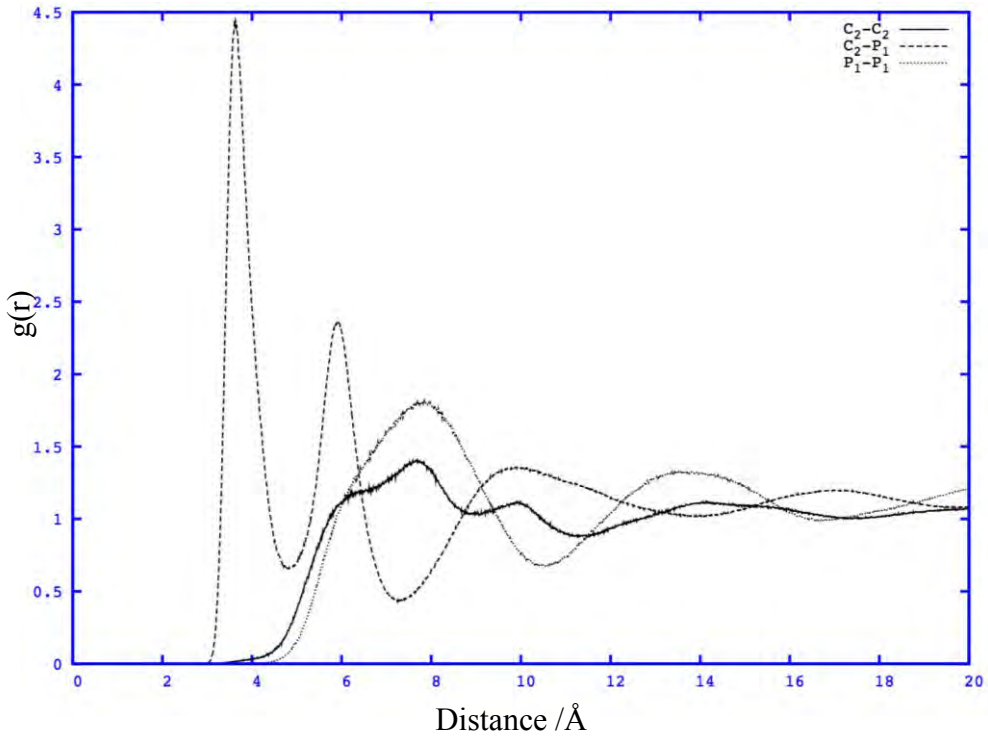

Figure 3.5: Atom-atom radial distribution function of a $[C_4MIM][PF_6]$ at T = 333.15 K and P =1 atm.

3.7.2 Correlation Functions

If one wishes to determine the correlation (supposing a correlation does exist) between two sets of data values *x* and *y*, one may do so by making use of a correlation function [1]. A correlation function provides a numerical value that encases the data and evaluates the strength of the correlation, a typical one being:

$$C_{xy} = \frac{1}{M}\sum_{i=1}^{M} x_i y_i \equiv \langle x_i y_i \rangle \qquad \text{Eq 3.41}$$

here it has been assumed that there are M values of x_i and y_i in the data sets.

If the quantities of *x* and *y* are the same, the function is usually called an *autocorrelation function* and gives an indication of the extent to which a system "recalls" its previous values. An example of one such case is that of a velocity autocorrelation coefficient whose value indicates how closely the velocity at a time t is correlated with velocity at the start, time 0. Some Correlation functions may be a property of an entire system whereas others can be averaged over all the particles like in the example of the velocity autocorrelation function, which is calculated by averaging over the *N* atoms in the simulation,

$$C_{vv}(t) = \frac{1}{N}\sum_{i=1}^{N} \mathbf{v_i}(t) \cdot \mathbf{v}_i(0) \qquad \text{Eq 3.42}$$

to obtain a normalized function, we divide by $\langle \mathbf{v}_i(0) \cdot \mathbf{v}_i(0) \rangle$:

$$C_{vv}(t) = \frac{1}{N}\sum_{i=1}^{N} \frac{\langle \mathbf{v}_i(t) \cdot \mathbf{v}_i(0) \rangle}{\langle \mathbf{v}_i(0) \cdot \mathbf{v}_i(0) \rangle} \qquad \text{Eq 3.43}$$

Thus an autocorrelation function has an initial value of 1 and at long times the value drops to 0. The time taken to lose correlation is known as the relaxation or correlation time. Simulations that are significantly longer than the relaxation times are preferred as many sets of data may be extracted from the simulation to calculate the correlation functions and to reduce the uncertainty of a calculation.

3.7.3 Self-Diffusion Constants

Molecules in a liquid tend to collide continuously with each other, preventing them from moving in simple linear paths. This motion is known as the diffusive motion of molecules, and can also be described as a random walk. *Fick's First Law* is the macroscopic law that can be used to describe diffusion. This law states that the flux, J, of the particle density is proportional to the negative gradient in the concentration of the same species:

$$J = -D\nabla c \qquad \text{Eq 3.44}$$

where D the proportionality constant called the diffusion coefficient. [11] For a uniform diffusion coefficient, the evolution of the concentration of molecules per unit volume with respect to time can be defined as follows using *fick's second law*:

$$\frac{\partial \rho(\boldsymbol{r},t)}{\partial t} = D\nabla^2\rho(\boldsymbol{r},t) \qquad \text{Eq 3.45}$$

where ρ is the concentration.

Equation 3.45 can be rewritten in terms of the probability density that a molecule will be found at some point in space. Letting $\wp(\mathbf{r}; t)$ be this normalized probability, we get for the concentration:

$$\rho(\boldsymbol{r},t) = \wp(\mathbf{r},\mathrm{t})\mathrm{N}$$

$$\int \wp(\mathbf{r},\mathrm{t})\mathrm{dr} = 1 \qquad \text{Eq 3.46}$$

if we substitute this into equation 3.46 we get:

$$\frac{\wp(\mathbf{r},t)}{\partial t} = D\nabla^2\wp(\mathbf{r},t) \qquad \text{Eq 3.47}$$

If a molecule is known to initially start at a given point ($\mathbf{r} = \mathbf{r_0}$) at t = 0. Then, the solution to $\wp(\mathbf{r}; b)$ can be obtained from:

$$\wp(\mathbf{r},t) = (\pi Dt)^{-\frac{3}{2}}\exp\left(-\frac{|\boldsymbol{r}-\boldsymbol{r_0}|^2}{4Dt}\right) \qquad \text{Eq 3.48}$$

The mean square displacement with respect to time can be computed from equation 3.48:

$$\langle|\boldsymbol{r}-\boldsymbol{r_0}|^2\rangle = \int \wp(\mathbf{r},t)|\boldsymbol{r}-\boldsymbol{r_0}|^2 d\boldsymbol{r}$$

$$= 6Dt \qquad \text{Eq 3.49}$$

Equation 3.49 is also called an Einstein relation and gives us a way to measure the diffusion constant in a simulation from the slope of the mean squared displacement (MSD) at long times:

$$D = \frac{1}{6}\lim_{t\to\infty}\langle(r_i(t)-r_i(0))^2\rangle \qquad \text{Eq 3.50}$$

For better statistics, the mean square displacement plots must be computed from multiple origins and the diffusion constants should only be calculated when the MSD plots show linearity, which only occurs after some initial time period has passed.

3.7.4 Pressure Fluctuations and Shear Viscosity

Shear viscosity and other transport properties can be calculated from molecular dynamics simulations with the aid of a suitable autocorrelation function [1]. For instance the viscosity is depend upon the stress tensor $P_{xz}(t)$ changes with time. At a time t the difference between $P_{xz}(t)$ and $P_{xz}(0)$ is given by:

$$|P_{xz}(t) - P_{xz}(0)| = \int_0^t v(t')dt' \qquad \text{Eq 3.51}$$

If both sides of the equation are squared we get

$$\langle |P_{xz}(t) - P_{xz}(0)|^2 \rangle = \int_0^t dt' \int_0^t dt'' \langle v(t') \cdot v(t'') \rangle \qquad \text{Eq 3.52}$$

Integration of the double integral, Eq 3.52 results in the Green-Kubo formula:

$$\frac{\langle |P_{xz}(t) - P_{xz}(0)|^2 \rangle}{2t} = \int_0^t \langle v(\tau).v(0) \rangle \left(1 - \frac{\tau}{t}\right) d\tau \qquad \text{Eq 3.53}$$

and in the limit:

$$\int_0^\infty \langle v(\tau).v(0) \rangle d\tau = \lim_{t\to\infty} \frac{\langle |P_{xz}(t) - P_{xz}(0)|^2 \rangle}{2t} \qquad \text{Eq 3.54}$$

The viscosity of a liquid can be related to the fluctuations of the off-diagonal elements of the pressure tensor. The viscosity can be calculated from an equilibrium simulation from the following Green-Kubo formula: [11]

$$\eta = \frac{V}{k_B T} \int_0^\infty \langle P_{xz}(t_0) P_{xz}(t_0 + t) \rangle_{t_0} dt \qquad \text{Eq 3.55}$$

This formula can also be expressed as an Einstein relationship:

$$\eta = \lim_{t\to\infty} \frac{1}{2}\frac{V}{k_B T}\frac{d}{dt}\left\langle\left(\int_{t_0}^{t_0+1} P_{xz}(t')dt'\right)^2\right\rangle_{t_0} \qquad \text{Eq 3.56}$$

both methods have been found to converge rather slowly, which is a result of the volume of the size of the simulation box fluctuates vigorously. The Einstein relation is considered to be the more convenient method to use as the inaccuracies in long time correlations can be avoided by only considering integrals over shorter correlation times.

3.8References

1. A. R. Leach, *Molecular Modelling: Principles and Applications*, Pearson Education, 2001
2. M. J. Frisch, G. W. Trucks, H. B. Schlegel, G. E. Scuseria, M. A. Robb, J. R. Cheeseman, G. Scalmani, V. Barone, B. Mennucci, G. A. Petersson, H. Nakatsuji, M. Caricato, X. Li, H. P. Hratchian, A. F. Izmaylov, J. Bloino, G. Zheng, J. L. Sonnenberg, M. Hada, M. Ehara, K. Toyota, R. Fukuda, J. Hasegawa, M. Ishida, T. Nakajima, Y. Honda, O. Kitao, H. Nakai, T. Vreven, J. A. Montgomery, Jr., J. E. Peralta, F. Ogliaro, M. Bearpark, J. J. Heyd, E. Brothers, K. N. Kudin, V. N. Staroverov, R. Kobayashi, J. Normand, K. Raghavachari, A. Rendell, J. C. Burant, S. S. Iyengar, J. Tomasi, M. Cossi, N. Rega, J. M. Millam, M. Klene, J. E. Knox, J. B. Cross, V. Bakken, C. Adamo, J. Jaramillo, R. Gomperts, R. E. Stratmann, O. Yazyev, A. J. Austin, R. Cammi, C. Pomelli, J. W. Ochterski, R. L. Martin, K. Morokuma, V. G. Zakrzewski, G. A. Voth, P. Salvador, J. J. Dannenberg, S. Dapprich, A. D. Daniels, Ö. Farkas, J. B. Foresman, J. V. Ortiz, J. Cioslowski, and D. J. Fox, Gaussian, Inc., Wallingford CT, 2009
3. GAMESS-UK is a package of ab initio programs. See: "http://www.cfs.dl.ac.uk/gamess-uk/index.shtml", M.F. Guest, I. J. Bush, H.J.J. van Dam, P. Sherwood, J.M.H. Thomas, J.H. van Lenthe, R.W.A Havenith, J. Kendrick, "The GAMESS-UK electronic structure package: algorithms, developments and applications", Molecular Physics, Vol. 103, No. 6-8, 20 March-20 April 2005, 719-747
4. P. Atkins, J. de Paula, *Atkins' Physical Chemistry*, Oxford University press, 2002
5. N. S. Ostlund, A. Szabo, *Modern Quantum Chemistry: Introduction to Advanced Electronic structure theory*, Dover Publications, New York, 1996
6. A. Hinchliffe, *Chemical Modelling: From atoms to Liquid*, Wiley, 1999
7. M.P. Allen, D.J. Tildesley. *Computer Simulations of Liquids*, Oxford University press, 1987
8. Mark E. Tuckerman, Douglas J. Tobias, Michael L. Klein, Mol. Phys., 1996, **87**, 1117 – 1157

9. M. Scott Shell, CHE210D lecture notes: Simulations of bulk phases, http://www.engr.ucsb.edu/~shell/che210d/Simulations_of_bulk_phases.pdf, accessed: 30.12.2013.
10. A. Frisch, J. B. Foresman, *Exploring Chemistry with Electronic Structure Methods* (Gaussian Inc. Pittsburgh, 1996)
11. M. Scott Shell, CHE210D lecture notes: Computing properties, http://www.engr.ucsb.edu/~shell/che210d/Computing_properties.pdf, accessed: 30.12.2013.
12. Encyclopedia of Computational Chemistry, eds. P. V. R. Scheleyer, N. L. Allinger, T. Clark, J. Gasteiger, P. A. Kollman, Wiley, Chichester, 1998
13. C. Crammer, *Essentials of computational chemistry*, Wiley, 2004
14. M. Mandello, G. S. Grest, J. Chem. Phys., 1997, **106**, 9327 - 9336
15. T. Koddermann, R. Ludwig, D. Paschek, Chem. Phys. Chem., 2008, **9**, 1851 – 1858
16. Jan H. Jensen, *Molecular Modeling Basics,* CRC Press, 2010,

CHAPTER 4

Classical Force Field Model for Room Temperature Ionic Liquids

4.1 Introduction

In this section molecular dynamics simulations are used to predict diffusion coefficients and viscosities of room temperature ionic liquids using a standard force field with and without employing scaling factors (see section 2.2.4). Structural features as well as liquid densities are investigated. Two specific ionic liquids, 1-butyl-3-methylimidazolium tetrafluoroborate ($[C_4MIM][BF_4]$) and 1-butyl-3-methylimidazolium ($[C_4MIM][PF_6]$) are used. $[C_4MIM][BF_4]$ and $[C_4MIM][PF_6]$ were chosen for this study as they have been extensively explored in literature using both experiment and simulations, this would allow for ease in benchmarking the results obtained in this study.

The bulk of the computational methods used in the work presented in this chapter have been discussed in general in chapters 2 and 3, however, the specific computational details of the methods are described below.

4.2 Computational Details

Initial configurations of 250 and 300 ion pairs of $[C_4MIM][BF_4]$ and $[C_4MIM][PF_6]$ in cubic boxes of 40 Å and 48 Å, respectively, were generated for molecular dynamics using Packmol [15]. The starting volumes were chosen to match the experimental density. The configurations were subsequently relaxed using 700 steps of Newton-Raphson energy minimization. The system was heated at 10.0 K every 50 steps to 800.0 K and then cooled at 10.0 K every 50 steps to 333.15 K, followed by 10 ns of MD simulation in the isothermal-isobaric (NPT) ensemble employing a Nose-Hoover barostat to maintain a pressure of 1.0 atm at a temperature of 333.15 K. Periodic boundary conditions were used. Of the 10 ns, 5 were regarded as equilibration and the remaining 5 were used to compute liquid densities and average simulation box sizes. NPT simulations were also carried out at 298.15 K, however, 333.15 K was preferred for the remainder of the discussion, since this temperature is well above the melting points of $[C_4MIM][BF_4]$ and $[C_4MIM][PF_6]$, which are 202.15 and 279.55

K, respectively. The time step was set to 1 fs and the Verlet algorithm was used to integrate the equations of motion. The SHAKE algorithm with a tolerance of 1.0×10^{-10} was applied to all bonds containing a hydrogen atom. The van der Waals interactions were cut off beyond 14.0 Å and a switching function initiated at 12.0 Å was used to bring the dispersion interaction to zero at the cut off distance. The nonbonded list cutoff was chosen as 14.0 Å. Long-range electrostatic interactions were treated with the particle mesh Ewald method [16 - 17]. The thermodynamic properties of the system such as total energy and velocity were saved every 50 timesteps.

Following this, canonical (NVT) molecular dynamics simulations were carried out at 333.15 K using the same computational details as above, using the average box size calculated from the NPT simulation. 50 ns of MD were recorded and the first 10 ns were regarded as equilibration. The MD simulations were carried out using CHARMM c35b2.

Parameters for the force field functional form were obtained in the following manner. Lennard-Jones parameters, torsion angle and bond distance/angle force constants for all the cations and anions were taken from the CHARMM 27 force field [14]. Partial charges on each of the atoms were calculated from DFT generated electrostatic potentials of isolated ion pairs using the Merz-Kollman methodology, the level of theory used was B3LYP/cc-pVDZ. The charges on symmetrically equivalent atoms were averaged and set equal. Gaussian 03 was used for all QM calculations. Force field parameters are shown in Table 4.1 and 4.2.

Table 4.1: Partial Atomic Charges and Lennard-Jones Parameters Used in This Work.

Atom	q /e	r_{min} /Å	ϵ_i /kJ mol^{-1}	Atom	q /e	r_{min} /Å	ϵ_i /kJ mol^{-1}
C_5	-0.2983	1.800	0.050	H_{11}	-0.0030	1.320	0.022
C_4	-0.1608	1.800	0.050	H_{12}	-0.0030	1.320	0.022
N_3	0.2358	1.850	0.200	C_{10}	-0.3488	2.06	0.080
C_2	-0.1935	1.800	0.050	H_{13}	0.0970	1.320	0.022
N_1	0.3738	1.850	0.200	H_{14}	0.0970	1.320	0.022
H_1	0.2328	0.900	0.046	H_{15}	0.0970	1.320	0.022
H_2	0.2764	0.900	0.046	B_1	1.0608	2.010	0.398
H_3	0.2272	0.900	0.046	F_1	-0.5152	1.750	0.255
C_6	-0.3310	2.275	0.020	F_2	-0.5152	1.750	0.255
H_4	0.1280	0.900	0.046	F_3	-0.5152	1.750	0.255
H_5	0.1280	0.900	0.046	F_4	-0.5152	1.750	0.255
H_6	0.1280	0.900	0.046	P_1	1.2823	2.150	0.255
C_7	-0.4692	2.275	0.020	F_1	-0.3804	1.700	0.255
H_7	0.1738	1.320	0.022	F_2	-0.3804	1.700	0.255
H_8	0.1738	1.320	0.022	F_3	-0.3804	1.700	0.255
C_8	0.1474	2.175	0.055	F_4	-0.3804	1.700	0.255
H_9	0.0066	1.320	0.022	F_5	-0.3804	1.700	0.255
H_{10}	0.0066	1.320	0.022	F_6	-0.3804	1.700	0.255
C_9	0.1717	2.175	0.055				

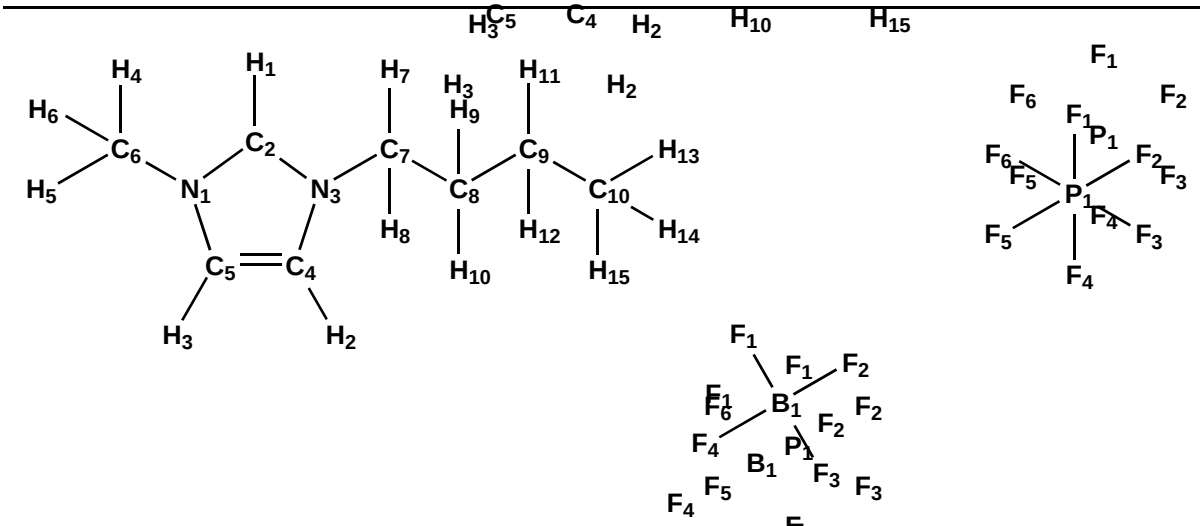

Figure 4.1: Structure of [C_4MIM], [BF_4] and [PF_6], with labeled atoms.

Table 4.2: Bond, Angle, Dihedral, and Improper Force Constants.

bonds	K_b /kJ mol^{-1} Å^{-2}		bonds		
		$r_{0\,/}$ Å		k_b /kJ mol^{-1} Å^{-2}	$r_{0\,/}$ Å
C_6-N_3	220.0	1.462	$C_{8,9}$-$H_{9,10,11,12}$	309.0	1.095
C_7-N_1	220.0	1.462	C_{10}-$H_{13,14,15}$	322.0	1.094
$N_{1,3}$-$C_{4,5}$	400.0	1.382	C_7-C_8	200.0	1.531
C_4-C_5	410.0	1.361	C_8-C_9	222.5	1.537
$N_{1,3}$-C_2	400.0	1.337	C_9-C_{10}	222.5	1.531
C_2-H_1	340.0	1.078	B-F	289.8	1.389
$C_{4,5}$-$H_{2,3}$	340.0	1.078	P-F	280.0	1.646
$C_{6,7}$-$H_{4,5,6,7,8}$	309.0	1.090			
angles	k_θ / kJ mol^{-1} rad^{-2}	θ_o /Deg	angles	k_θ / kJ mol^{-1} rad^{-2}	θ_o /Deg
C_8-C_7-N_1	140.0	112.3	$H_{7,8}$-C_7-H	35.5	108.4
$C_{4,5}$-$N_{1,3}$-C_2	130.3	108.3	$H_{7,8}$-C_7-C_8	33.4	111.7
$H_{4,5,6}$-C_6-N_3	30.0	109.4	$H_{9,10}$-C_8-C_7	33.4	109.1
H_1-C_2-$N_{1,3}$	25.0	125.4	C_7-C_8-C_9	58.0	111.5
N_1-C_4-C_5	25.0	130.7	C_8-C_9-C_{10}	58.4	112.3
N_1-C_2-N_3	130.0	109.1	H-$C_{8\text{-}9}$-H	35.50	108.4
$N_{1,3}$-C_2-H_1	25.0	125.4	C_8-$C_{9,}$-H	26.5	108.4
$H_{2,3}$-$C_{4,5}$-C	25.0	130.5	C_9-C_{10}-H	35.5	107.2
N_3-C_4-H_2	25.0	122.0	F-B-F	49.9	109.5
$H_{4,5,6}$-C_6-H	35.5	108.4	F-P-F	100.0	90.0
dihedrals	K_x / kJ mol^{-1}	n	θ_o /Deg	dihedrals	K_x / kJ mol^{-1}	n	θ_o /Deg
C_2-N_3-C_4-C_5	14.0	2	180.0	C_2-$N_{1,3}$-$C_{7,6}$-H	0.195	2	180.0
N_1-C_5-C_4-N_3	14.0	2	180.0	$C_{4,5}$-$N_{3,1}$-$C_{6,7}$-H	0.0	3	0.0
N_1-C_2-N_3-C_4	14.0	2	180.0	C_2-$N_{3,1}$-C_7-C_8	0.1	3	180.0
H_1-C_2-$N_{1,3}$-$C_{5,4}$	3.0	2	180.0	C_5-N_1-C_7-C_8	0.2	4	0.0
H_2-C_4-C_5-H_3	2.0	2	180.0	N_1-C_7-C_8-C_9	0.0	3	0.0
C_4-$C_{5,4}$-$N_{1,3}$-$C_{7,6}$	0.0	0	0.0	H,C-C_9-C_{10}-H	0.16	3	0.0
H_2-C_4-N_3-C_2	3.0	2	180.0	N_1-C_7-C_8-$H_{9,10}$	0.0	3	0.0
$N_{1,3}$-$C_{5,4}$-$C_{4,5}$-$H_{2,3}$	3.0	2	180.0	C_7-C_8-C_9-C_{10}	0.15	3	0.0
$N_{1,3}$-C_2-$N_{3,1}$-$C_{6,7}$	0.0	2	180.0	$H_{7,8}$-C_7-C_8-$H_{9,10}$	0.195	3	0.0

Table 4.2 continues…

dihedrals	K_x / kJ mol^{-1}	n	θ_o /Deg	dihedrals	K_x / kJ mol^{-1}	n	θ_o /Deg
H_1-C_2-$N_{3,1}$-$C_{6,7}$	0.0	2	180.0	H,C-C_8-C_9-H,C	0.195	3	0.0
$H_{2,3}$-$C_{4,5}$-$N_{3,1}$-$C_{6,7}$	0.0	2	180.0				
improper	k_ψ / kJ mol^{-1} rad^{-2}		ψ_o /Deg	improper	k_ψ / kJ mol^{-1} rad^{-2}		ψ_o /Deg
H_1-N_1-N_3-C_2	0.50		0.00	$N_{1,3}$-$C_{4,5}$-C_2-$C_{6,7}$	0.60		0.00

4.3 Results and Discussion

4.3.1 Density

Experimentally the density of room temperature ionic liquids is one of the easiest and most unambiguous properties to measure with aid of an excellent analytical balance and volumetric glassware. Shown in table 4.3 are the experimental and simulated liquid densities for [C_4MIM][BF_4] and [C_4MIM][PF_6] at 298.15 K and 333.15 K.

Table 4.3: Liquid densities for [C_4MIM][BF_4] and [C_4MIM][PF_6].*

	Temp /K	[C_4MIM][BF_4] /g cm^{-3}	[C_4MIM][PF_6] /g cm^{-3}
Simulation	333.15	1.080 ± 0.0012	1.3358 ± 0.00189
Experiment	333.15	1.178 [13]	1.340 [13]
Simulation	298.15	1.102 ± 0.002	1.362 ± 0.0036
Experiment	298.15	1.211 [35]	1.368 [32]

**Simulation errors were calculated as the standard deviation of the density calculated from five 1 ns blocks*

The density of the RTILs was calculated from the oscillations of the MD box volume. The current model was found to have great predictive ability for [C_4MIM][PF_6], but did not perform as well for [C_4MIM][BF_4]. The calculated percentage deviations of the molecular dynamics simulation from the experimental values were found to be 8.3 and 0.3 % for [C_4MIM][BF_4] and [C_4MIM][PF_6] at 333.15 K and 9.0 and 0.4 % at 298.15 , respectively.

The force field performs better at higher temperatures and although being very accurate to model [C_4MIM][PF_6], the density of [C_4MIM][BF_4]is underestimated. Liu and co-workers [12] reported a classical force field based on AMBER for these ionic liquids. This force field had a 1.4 % deviation from experiments at 298 K for [C_4MIM][BF_4], performing significantly better than our current force field. For [C_4MIM][PF_6] at 313 and 333 K they the error was 0.8 and 1.1 %. Tokuda and co-workers showed that there is a relationship between the molecular weight of the cation and the density [5]. Thus, for RTILs with the same cation, the density should be directly proportional to the molecular weight of the anion. Studies have also shown that there is a linear decrease in density of an ionic liquid with an increase in the temperature [6-9] as opposed to conventional (non-charged) solvents.

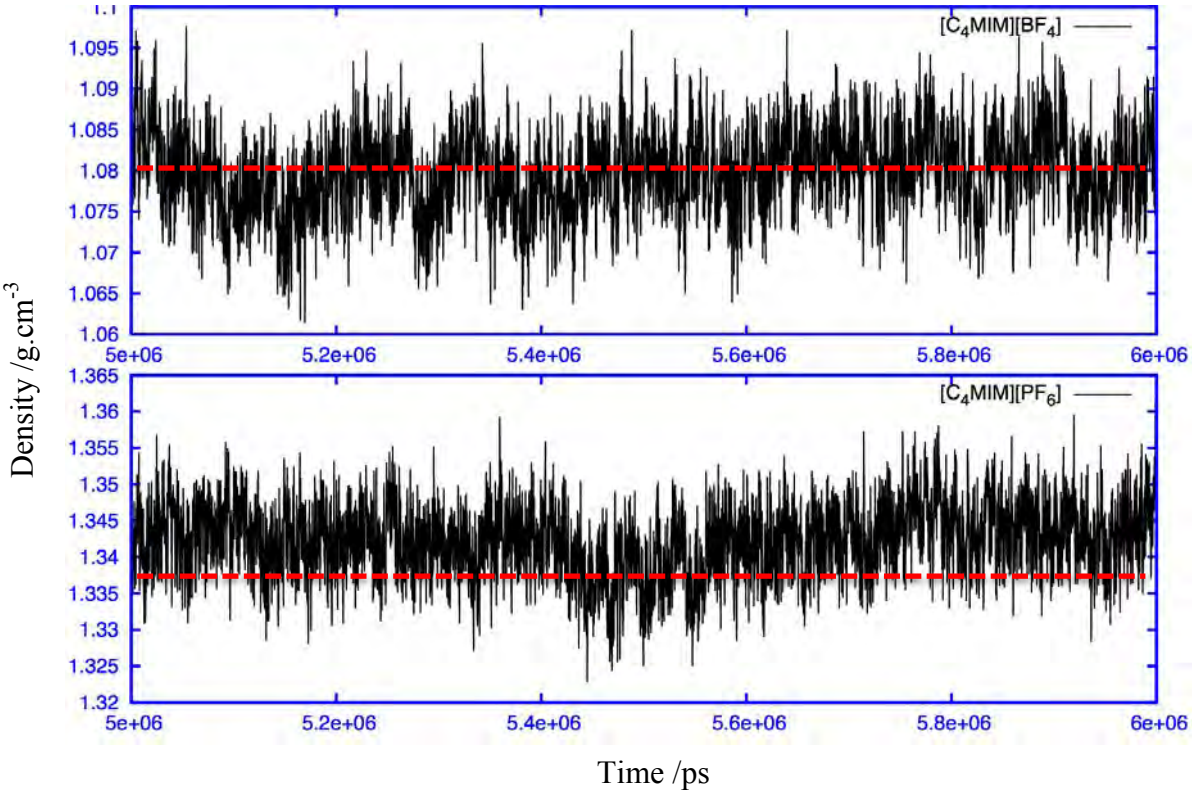

Figure 4.2: The densities of [C_4MIM][BF_4] and [C_4MIM][PF_6] plotted over time and the calculated average density (Shown as the red line).

Figure 4.2 shows the density fluctuation of the liquid over a 1 ns time period during the simulation. The density of the liquid tends to sit in blocks alternating around the overall observed liquid density. Radial distribution functions (RDFs) calculated over the alternating

blocks show no significant difference in the structure of the liquid, thus these fluctuations are not a result of a change in phase within the room temperature ionic liquid.

The agreement between simulated densities and experiment could be improved by fine-tuning the Lennard-Jones parameters, however, for the purposes of this work, which focuses on the investigation of the partial charges in RTIL models, we have elected to keep all other parameters constant as far as possible.

In MD studies, much like in experiment, liquid densities are easy to compute. Transport properties, however, are challenging to simulate accurately, especially in RTILs where the intermolecular interactions are strong and polarisation is important. The focus of the work is therefore to development a force field that can accurately describe transport properties of RTILs, such as diffusion and viscosity.

4.3.2 Liquid Structure

Information from Nuclear Magnetic Resonance (NMR) and Infrared (IR) spectroscopy experiments have shown that for imidazolium based ionic liquids, interactions between the acidic hydrogens on the imidazolium ring (C_2, and C_4/C_5) and the anion are the most important [8]. Figure 4.3 and 4.4 show the radial distribution functions (RDFs) of C_2-X, C_4-X, C_5-X, C_2-C_2 and X-X where X=B/P for [C_4MIM][BF_4] and [C_4MIM][PF_6] respectively, that were computed over 5 ns trajectory. Site-site (i.e. atom to atom) RDFs are often preferred over center-of-mass RDFs as they provide a more detailed account of the structure of the liquid [24], this work makes use of site-site RDFs.

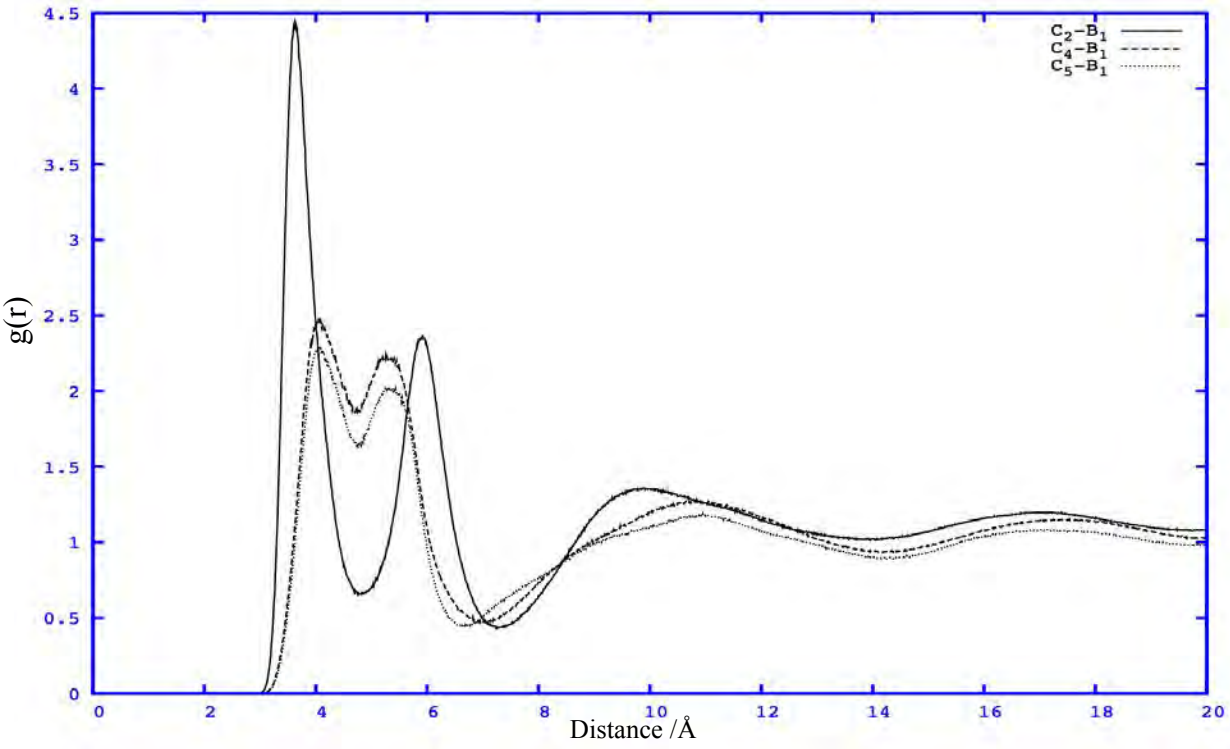

(a)

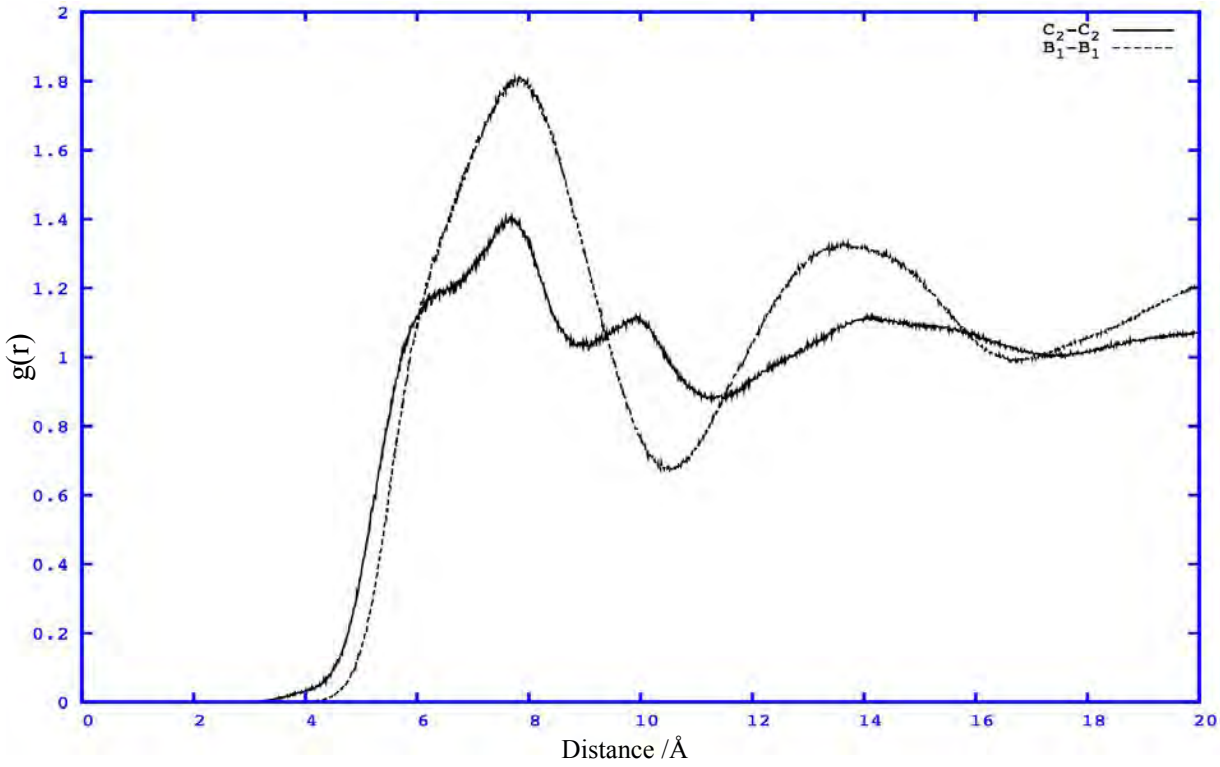

(b)

Figure 4.3: (a) C_2-B_1, C_4-B_1, C_5-B_1 and (b) C_2-C_2, B_1-B_1 radial distribution function in [C_4MIM][BF_4] calculated over a 5 ns period.

In figure 4.3it can be seen that the ordering in the liquid spans beyond 20 Å, which is nearly half of the length of the simulation box. This ordering is characteristic of a system dominated by the long-range Coulombic interactions [24]. The C_2-X RDF in figure 4.3 (a), shows that there are four peaks located at 3.6, 6.0, 10.6 and 17.3 Å. The first two peaks indicate a solvation shell consisting of mostly anions nearest to the cation. The first of these peaks correspond to strong coordination with the H_2 proton (the "front"), the second to weaker coordination with H_4/H_5 (the "back"). The weak nature of this latter interaction is evident from the position of the first peak around H_4/H_5, which occurs at a larger distance and lower value of g(r). Liu and co-workers [12] reported two solvation shell locations for the same system at 4.4 Å and 11.6 Å. The difference results from them using centre-of-mass (COM) RDFs. Since the imidazolium COM is closer to the middle of the ring, coordination at the front and back is equidistant and appears as one peak; these RDFs always have less peaks than their atom-atom based counterparts [24, 34,36-37].

Table 4.2 shows the RDF maxima and minima, as well as the coordination numbers over the first and second peak, calculated for [C_4MIM][BF_4]. The coordination number, N, can be calculated from the integration of the RDF from one minima to another,

$$N = 4\pi \int_{R_{min1}}^{R_{min2}} \rho g(r) r^2 dr \qquad \text{Eq 4.1}$$

where ρ is the number density and R_{minX} refers to the appropriate minima in g(r), as given in Table 4.2. Coordination is preferred at the front of the cation above and below the plane of ring. This is confirmed here with an integration of 2.3 representing ≈ 2 anions. Likewise, at the back of the cation a total of two anions coordinate (N = 1.8), one with each of the hydrogens H_4 and H_5. A centre-of-mass RDF would report a first cation-anion solvation shell coordination number that would be the sum of calculated coordination numbers from the C_2-X, C_4-X and C_5-X RDFs. If the three coordination numbers are summed, a value of 5.7 is obtained, which is consistent with the coordination number of 6 reported by Liu and co-workers.

Table 4.2: $[C_4MIM][BF_4]$ Radial distribution function maxima, minima and first and second shell coordination numbers.

	Position[a] / Å				Number of ions	
	$\mathbf{R}_{max1}$	$\mathbf{R}_{min1}$	$\mathbf{R}_{max2}$	$\mathbf{R}_{min2}$	N_1	N_2 2nd Peak
C_2-X	3.6	4.9	6.0	7.6	2.3	5.7
C_4-X	4.0	4.9	5.8	6.2	1.8	5.2
C_5-X	4.0	4.9	5.8	6.7	1.8	5.3
X-X	7.9	8.6	10.1	11.6	-	-
C_2-C_2	7.1	10.4	14.1	10.4	-	-

[a]*Tabulated values refer to locations of the maximum and minimum of the radial distribution function*

Much like the $[C_4MIM][BF_4]$, $[C_4MIM][PF_6]$ was found to have an ordering that spans past 20 Å. In fact the RDFs of the two systems are very similar. The anion-anion (P_1-P_1) RDF in $[C_4MIM][PF_6]$, however, exhibits a split peak, which is a result of the sequential ordering that occurs as a result of cation-anion pair interactions.

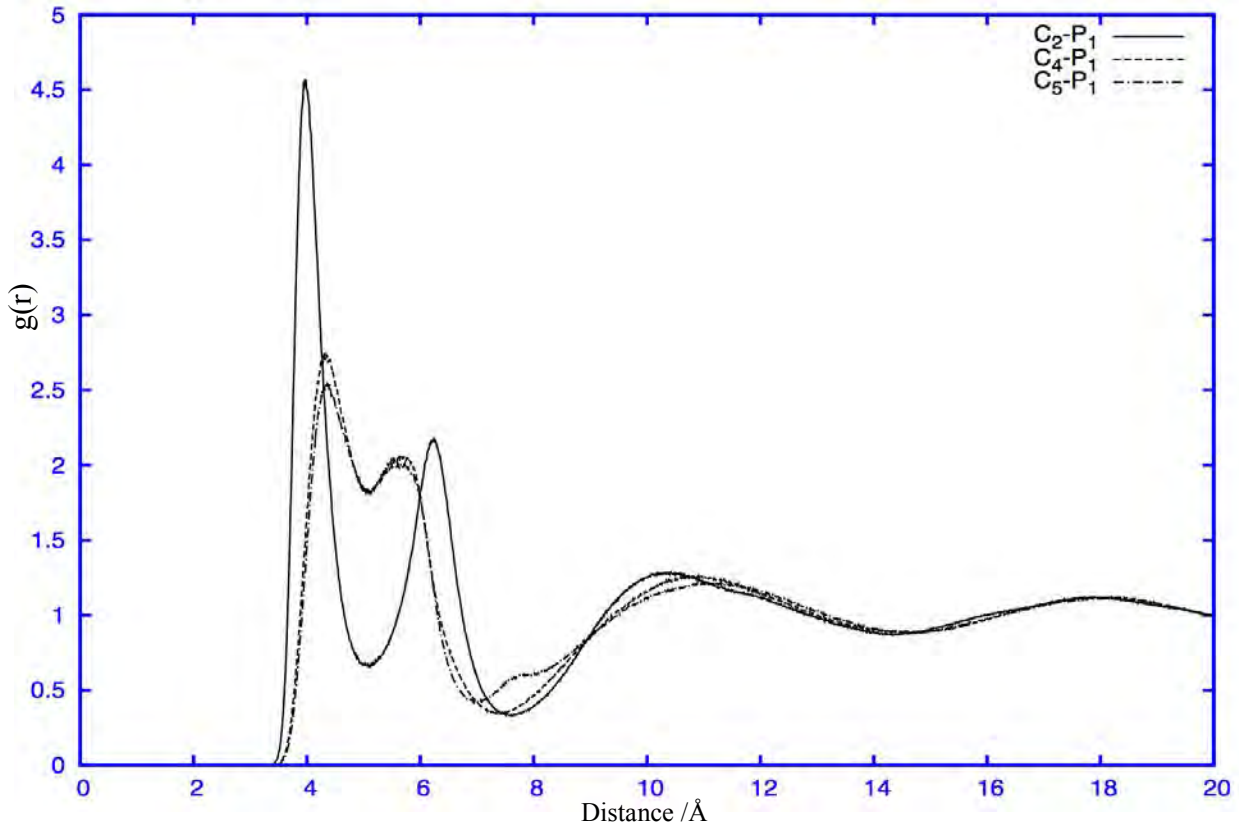

(a)

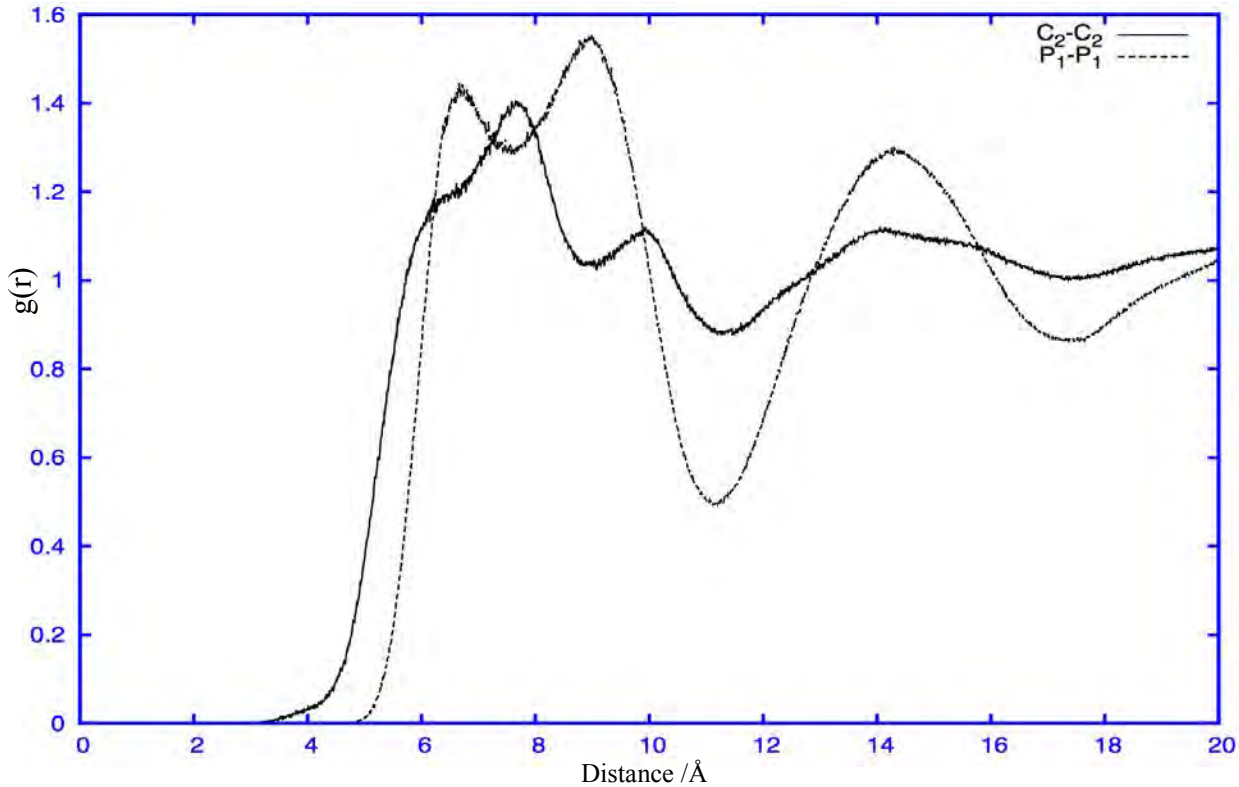

(b)

Figure 4.4: (a) C_2-P_1, C_4-P_1, C_5-P_1 and (b) C_2-C_2, P_1-P_1 RDFs of [C_4MIM][PF_6] calculated over a 5 ns period.

Table 4.3 lists all the calculated maxima, minima and coordination numbers for $[C_4MIM][PF_6]$.

Table 4.3: $[C_4MIM][PF_6]$ Radial distribution function maxima and minima.

	Position[a] / Å				Coordination numbers	
	$\mathbf{R}_{max1}$	$\mathbf{R}_{min1}$	$\mathbf{R}_{max2}$	$\mathbf{R}_{min2}$	N_1	N_2
C_2-X	3.9	5.1	6.3	7.9	2.2	5.8
C_4-X	4.2	5.0	5.8	6.9	1.8	5.6
C_5-X	4.2	5.0	5.8	7.6	1.7	5.2
X-X	8.9	7.5	9.2	11.8	-	-
C_2-C_2	7.6	8.6	10.2	11.6	-	-

[a] *Tabulated values refer to locations of the maximum and minimum of the radial distribution function*

Both [C4MIM][PF6] and [C4MIM][BF4] have an approximate total of 6 and 16 anions surrounding a central cation in its first and second solvation shell. The solvation shells of [C4MIM][PF6] were found to be slightly bigger in size, which is consistent with PF6 being slightly bigger than BF4. Morrow and Maginn [24] studied [C4MIM][PF6] and reported three solvation shells located at 4.3, 10.6, and 17.6 Å, with the cation centre-of-mass as the reference. We found four peaks corresponding to three solvation shells at 3.9, 6.3, 10.8 and 17.6 Å, in close agreement with those reported in reference 24. The first two peaks in this work correspond to the first solvation shell reported by Morrow and Maginn. The first solvation shell splits into two peaks because of the asymmetry in the cation when using atom centred RDFs, whereas Morrow and Maginn used centre-of-mass (which lies closer to the geometric centre of the imidazolium ring) RDFs.

4.3.2 Self-diffusion coefficients

In this section the diffusivity of $[C_4MIM][BF_4]$ and $[C_4MIM][PF_6]$ is evaluated from MD simulations.

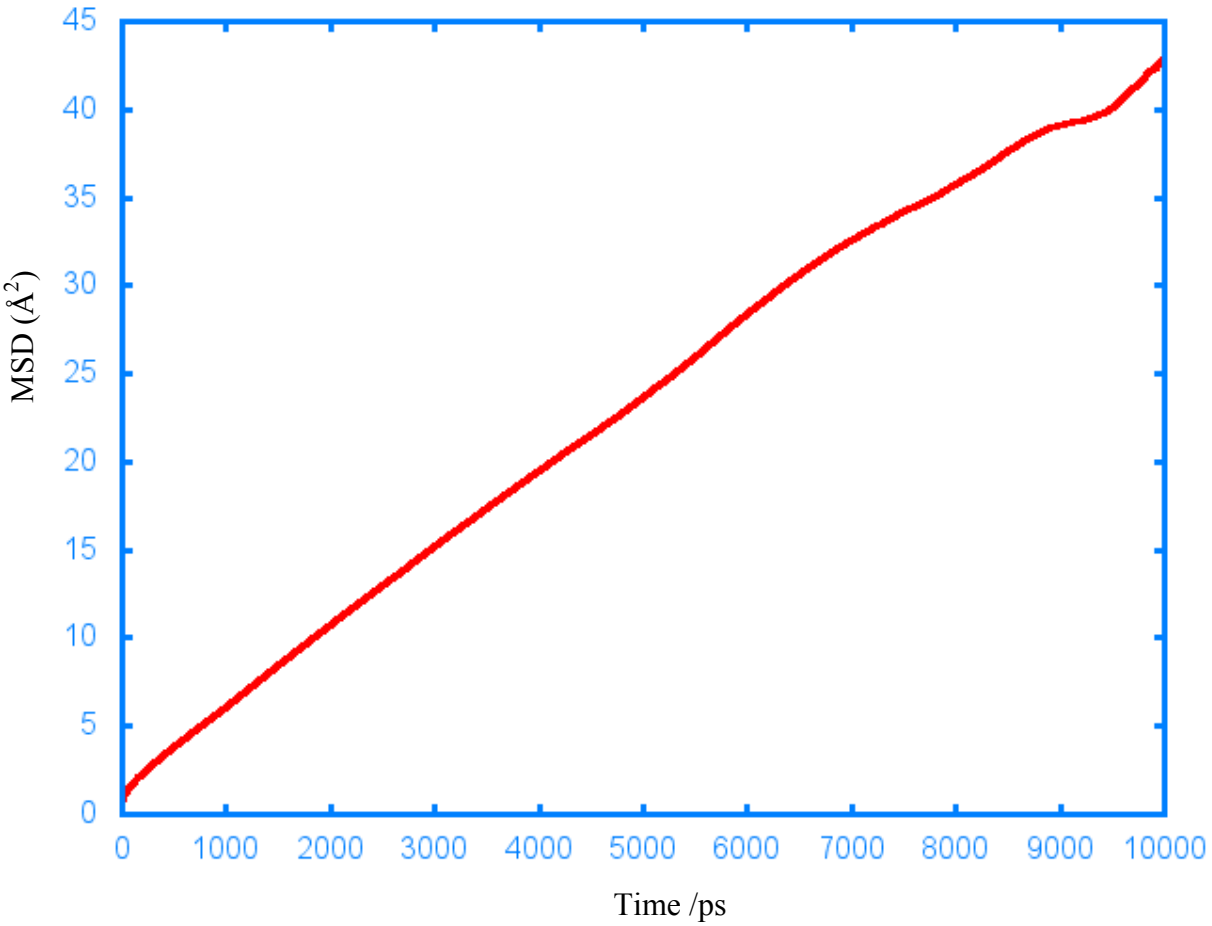

Figure 4.5: Mean square displacements (MSDs) of cations in $[C_4MIM][BF_4]$ calculated over a 10 nanosecond trajectory.

Table 4.4 shows the calculated self-diffusion coefficients for the anions and cations of the ionic liquids calculated from the Einstein relationship [28],

$$D = \frac{1}{6}\lim_{t\to\infty}\langle(r_i(t) - r_i(0))^2\rangle \qquad \text{Eq 4.2}$$

where $\langle (r_i(t) - r_i(0))^2 \rangle$ is the center-of-mass, ensemble averaged mean square displacements (MSDs) of particle *i*, either the cation or anion. The average is calculated as a sum of all ions, *N*, with a normalisation constant $\frac{1}{N}$. For each simulation 50 ns of MD trajectory was recorded and MSDs were computed. Figure 4.5 shows a 10 ns block MSD plot computed from the start of the simulation to 10 ns. The plot shows that the MSD becomes linear after approximately 100 ps, however, previous studies have shown that for some [C_4MIM][BF_4] RTILs (depending on the viscosity) one requires trajectories of up to 5 ns to accurately calculate self-diffusion coefficients [2 - 4]. This is because equation 4.2 is only valid once a system reaches its true diffusive motion. Ionic liquids are notorious for their slow diffusion [3] and thus take a significant amount of time to reach this regime.

One can determine whether the diffusive regime has been reached by plotting the following expression as a function of time, [13]

$$\beta(t) = \frac{d \log((r_i(t) - r_i(0))^2)}{d \log(t)} \qquad \text{Eq 4.3}$$

where β characterizes the motion of the system. β < 1 represents motion in the sub-diffusive state and β = 1 indicates that the system is experiencing diffusive motion.

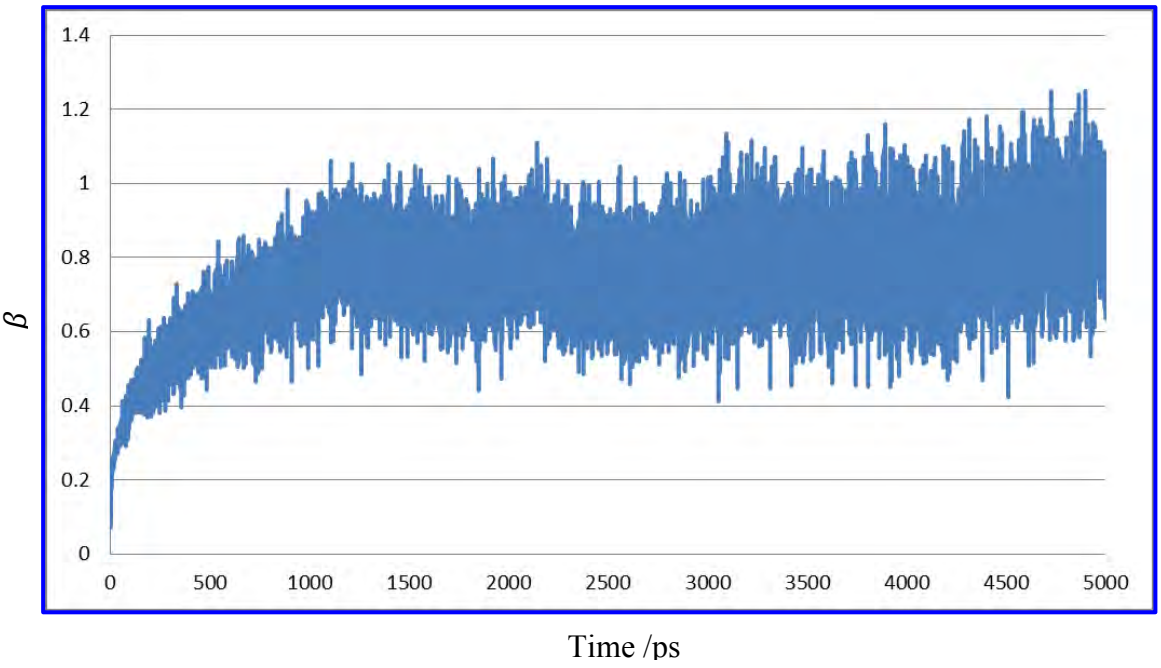

Figure 4.6: The value of β for [C_4MIM][BF_4] as a function of time calculated at 333.15 K.

The β values for all systems were calculated and plotted in order to determine an appropriate length scale for the calculation of self-diffusion coefficients. In practice, it has been shown that a β value of 0.7 and above is sufficient for an accurate estimation of diffusion coefficients [10]. Figure 4.6 shows this plot for [C_4MIM][BF4]. The system has not quite reached its diffusive motion even when 1 ns has elapsed and it should be expected that one needs to exclude at least an initial 2 ns of simulation data in fitting the linear region.

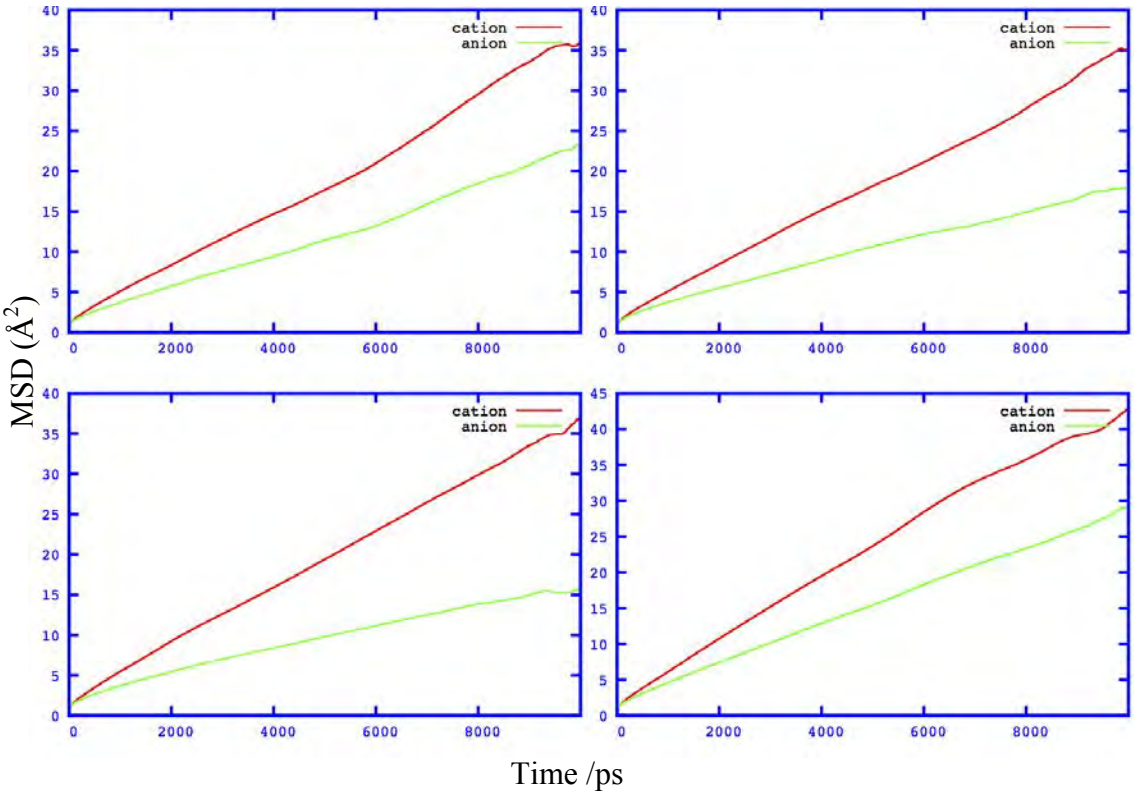

Figure 4.7: 10 ns block MSDs of the cations and anions of [C_4MIM][BF_4] at 333.15 K.

Following equilibration, the remaining 40 ns of data was split into blocks of 10 ns, as shown in figure 4.7, and self-diffusion coefficients were determined from each block and averaged in order to obtained a measure of error. This was done by fitting a straight line between 4 and 8 ns in each of the blocks; average diffusion coefficient and the standard deviation are shown in table 4.4. The standard deviation, expressed as a percentage of the diffusion coefficient, is much less for [C_4MIM][BF_4] (≈10%) than for [C_4MIM][PF_6] (≈30%). This can be attributed to the overall slower diffusion of the latter, thus requiring longer simulation times and an

expected larger error if the same length of simulation is used. These results suggest that even longer simulation times could be used, however, we deemed the accuracy sufficient for the comparative needs of this work.

Stokes' Law stipulates that in a simple liquid one can expect the smaller species, or rather the species with smaller effective radii, to diffuse at a faster rate in comparison to larger species within the liquid [8]. This, however, does not hold for RTILs as the involved species are charged and electronic interactions such as hydrogen bonding have been thought to result in deviations from this law [8]. It has been shown that the diffusion rates of the anionic species are associated with their strength as hydrogen bond acceptors [24 -27], anions that interact much more strongly with the cations will tend to diffuse slower than expected from size arguments. Table 4.4 shows the calculated self-diffusion coefficients as well as experimentally determined values.

Table 4.4: Calculated self-diffusion coefficients /x10^{-11} m^2s^{-1} for $[C_4MIM][BF_4]$ and $[C_4MIM][PF_6]$ at 333.15 K.

	$[C_4MIM][BF_4]$/x10^{-11} m^2s^{-1}		$[C_4MIM][PF_6]$/ x10^{-11} m^2s^{-1}	
	Anion	Cation	Anion	Cation
Simulation	1.29 ± 0.108	2.43 ± 0.018	0.134 ± 0.053	0.268 ± 0.074
Experiment [5]	5.94	5.91	2.84	3.65

Experimental data for self-diffusion coefficients are very scarce, more so at our working temperature of 333.15 K. Tokuda *et al*. used PGSE-NMR measurements to determine the diffusion of the ions in $[C_4MIM][BF_4]$ and $[C_4MIM][PF_6]$ over a range of temperatures from 260 to 380 K [5]. The data were fit to a Vogel-Fulcher-Tamman (VFT) equation;

$$D = D_o \exp\left[\frac{-B}{(T - T_0}\right]$$

with the parameters D_0, B and T_0, shown in table 4.5.

Table 4.5: VFT equation parameters of self-diffusion coefficients data taken from reference 5.

$$D = D_o \exp\left[\frac{-B}{(T - T_0)}\right]$$

	D_0 /x10^{-4} $cm^{-2}s^{-1}$	B /x10^2	T_0 /K
$[C_4MIM][BF_4]$			
Cation	1.4 ± 0.1	9.25 ± 0.28	162 ± 2
Anion	2.8 ± 0.4	11.08 ± 0.40	153 ± 3
$[C_4MIM][PF_6]$			
Cation	1.5 ± 0.3	9.87 ± 0.54	164 ± 4
Anion	1.8 ± 0.3	10.84 ± 0.54	165 ± 4

This expression was subsequently used to determine diffusion coefficients at 333.15 K. Table 4.4 shows that the force field gives low self-diffusion coefficient in comparison to experiment. This result is in line with the slow dynamic behavior exhibited when non-polarisable force fields are used in simulations [18,19,24,36]. Developing a force field model that can predict both thermodynamic and transport properties of RTILs is still one of the most challenging tasks, as can be seen from our results. The current force field model is able to reproduce the density, but struggles to reproduce a dynamic property such as the self-diffusion coefficient.

Compared to experiment, a deviation of 78.3 and 95.3% for the anions of $[C_4MIM][BF_4]$ and $[C_4MIM][PF_6]$, respectively and likewise 58.9 and 92.7% for the cations, is observed. It is noteworthy that Tokuda determined the diffusion of the anion and cation in $[C_4MIM][BF_4]$ to be very similar and that the anion in fact diffuses slightly faster. Using VFT coefficients it was determined that only at temperatures below 330 K does the anion diffuse slower. The MD results here predict a slower diffusing anion at 333 K, in line with other simulation studies [24, 34]. Traditional classical force field models for RTILs using data directly from gas phase computations are known to severely overestimate self-diffusion coefficients. Earlier force field models have reported deviations from experiments that are well over 100%, whereas some studies did not validate their models against experimentally determined transport properties. In most of the earlier cases force fields were not validated against experimental data due to the very limited availability of data from experiments for these RTILs. [16, 21, 33]

4.3.4 Viscosity

Viscosity is another transport property that is extremely important to predict. RTILs have high viscosities compared to molecular solvents and classical non-polarisable force fields are known to overestimate this viscosity. This can be expected from the underestimation of diffusion coefficients, from the Stokes-Einstein equation. Viscosity can be calculated via equilibrium MD [20] using the Green-Kubo (GK) formula discussed in section 3.5.3 [3].

$$\eta = \frac{V}{10k_BT}\int_0^\infty \langle \sum_{\alpha\beta} P_{\alpha\beta}(0)P_{\alpha\beta}(t)\rangle dt \qquad \text{Eq 4.4}$$

Here $P_{\alpha\beta}$ is an $\alpha\beta$ element of the pressure tensor. The viscosity is calculated as a collective property and statistical improvement is obtained by including fluctuations of the diagonal components of the pressure tensor [38,39]. For the viscosity estimates, the sum of the autocorrelation function is comprised of six independent terms of the pressure tensor, which are; $2P_{xy}$, $2P_{yz}$, $2P_{zx}$, $\frac{4}{3}\left[P_{xy} - \frac{1}{3}(P_{xx} + P_{yy} + P_{zz})\right]$, $\frac{4}{3}\left[P_{yy} - \frac{1}{3}(P_{xx} + P_{yy} + P_{zz})\right]$ and $\frac{4}{3}\left[P_{zz} - \frac{1}{3}(P_{xx} + P_{yy} + P_{zz})\right]$. The components of the pressure tensor are calculated during the simulation in CHARMM and written to file.

The bracket in equation 4.4 indicates that the average must be taken over all time origins. V is the volume, T is temperature and k_B is the Boltzmann constant.

Alternatively, viscosity can be calculated using the Einstein relation, [3]

$$\eta = \frac{V}{20k_BT}\lim_{t\to\infty} dt\langle \sum_{\alpha\beta}(G_{\alpha\beta}(t) - G_{\alpha\beta}(0))^2\rangle \qquad \text{Eq 4.5}$$

where,

$$G_{\alpha\beta}(t) = \int_0^t P_{\alpha\beta}(t')dt' \qquad \text{Eq 4.6}$$

Equation 4.5 requires the determination of the mean square displacement of the integral of the pressure tensor [22], after which the viscosity can be calculated from the gradient of the (MSD).

Table 4.6 shows viscosity estimates calculated using both methods.

Table 4.6: Viscosities in mPa s (cP) for $[C_4MIM][BF_4]$ and $[C_4MIM][PF_6]$ at 333.15 K.

$[C_4MIM][BF_4]$/ mPa s		**$[C_4MIM][PF_6]$/ mPa s**	
Experiment			
31 [13] (22.5)*		59 [13] (45.3)*	
Simulation			
Green-Kubo	**Einstein**	**Green-Kubo**	**Einstein**
158 ± 16	145.3 ± 59.2	682 ± 128	526.8 ± 81.2

* *Experimental viscosity calculated using Tokuda's VFT fits at 333.15 K* [5].

Obtained results indicate a significant overestimation of the viscosity of both systems. $[C_4MIM][BF_4]$, which has an experimental viscosity of 31 mPa s (cP) at 333 K, is estimated to a have a viscosity of ~160 mPa s using the Green-Kubo method. An example of the viscosity estimate plot is shown in Figure 4.8. Using the Einstein relation a viscosity of ~145 mPa s is predicted using the integral of the pressure tensor shown in Figure 4.9. The calculated viscosities are thus between 5 and 10 times the experimental viscosity.

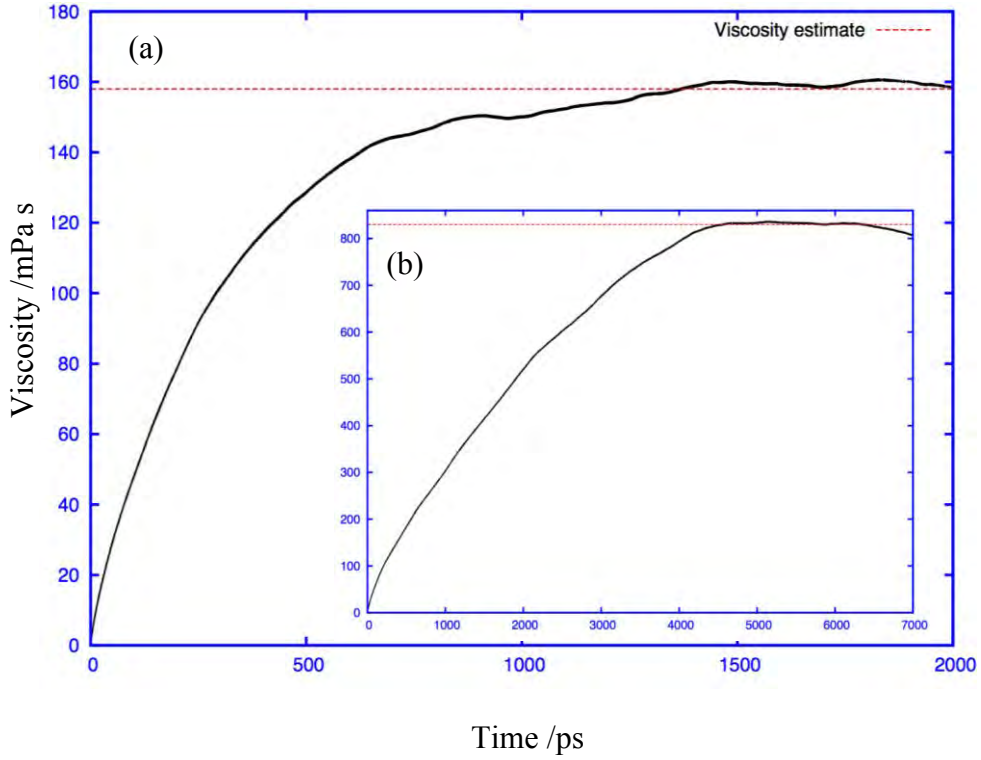

Figure 4.8: Green-Kubo viscosity estimate for (a) $[C_4MIM][BF_4]$ (b) $[C_4MIM][PF_6]$ computed at 333.15 K over 40 ns.

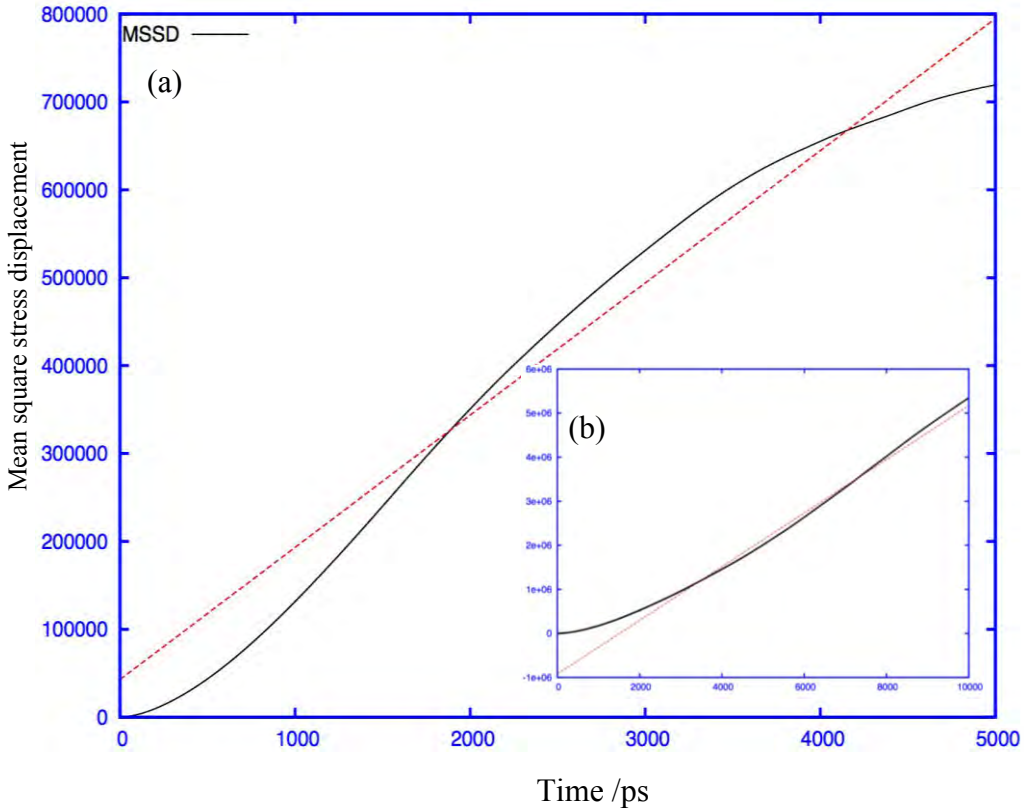

Figure 4.9: Einstein relation mean square stress displacement for (a) $[C_4MIM][BF_4]$ (b) $[C_4MIM][PF_6]$ computed at 333.15 K over 40 ns.

We calculated viscosity estimates using 40 ns of MD. Chen *et al*. [20] investigated the short and long correlation time behavior of a pressure-pressure time correlation function for a simple Lennard-Jones fluid. Similar results are seen in this work. In figure 4.8 (a) and (b) the correlation function was computed over 40 ns, but it gives a plateau after several hundred picoseconds giving an overestimation of the viscosity of the liquid. The observed result of overestimated viscosities is similar to that of other force fields that make use of gas phase data in parameterisation [40].

It is possible to improve the calculation of the running integral in equation 4.4 by fitting the correlation function to a decaying exponential function and obtaining the integration analytically [41]. As the aim here was not to determine very accurate viscosities but rather judge the effect of altering the charge parameterisation procedure, this additional complexity was not attempted.

4.4 Charge Scaling

A number of studies have been conducted on improving the shortcomings of classical force fields for RTILs. It has been shown that introducing polarisability can significantly improve the prediction of transport properties [23]. This is, however, a computationally expensive method and thus many groups have looked at developing methods that are just as effective yet not so computationally demanding. One such method is reducing the total charges on the ions. Morrow and Maginn [24] showed that the dynamics of a RTIL could be significantly improved by reducing the charges. A similar strategy as that used by Youngs and Hardacre [43], which is to linearly scale down the partial charges in order to improve the transport properties, is used next. This in effect scales the electrostatic interaction by a factor of S^{eff} (see section 2.2.4). The partial charges on the ions were scaled to give charges of ±0.6, ±0.7, ±0.8, ±0.9 and ±1.2. Non-scaled (± 1.0) results from the previous sections are included here to allow for comparison

4.4.1 Density

The tabulated result (see Table 4.6) for the density clearly indicate that as one linearly scales down the charges on the ions the liquid becomes less dense, due to the a decrease in the interionic interactions. In turn an improvement in the mobility of the ions can thus be expected. The changes in the predicted densities range from 0.9789 to 1.1181 g cm^{-3} for $[C_4MIM][BF_4]$ and 1.2337 to 1.3358 g cm^{-3} for $[C_4MIM][PF_6]$. It is important to note that scaling is expected to decrease density as explained above, thus a force field that predicts densities that are lower than experiment cannot be improved in this way. Rather, this latter observation is symptomatic of Lennard-Jones parameters that are not optimal and can be corrected accordingly.

Experiments have reported varying values for densities that lie within or just outside of the predicted range in this work. This is obviously related to the accuracy and the precision used in the experimental technique and the purity of the samples [42].

Table 4.6: Simulated liquid densities for $[C_4MIM][BF_4]$ and $[C_4MIM][PF_6]$ at 333.15K with different scaling factors.

Scaling factor	Density /g cm^{-3}	
	$[C_4MIM][BF_4]$	$[C_4MIM][PF_6]$
Experimental	1.178 [13]	1.340 [13]
0.6	0.9789 ± 0.0004	1.2377 ± 0.0014
0.7	1.0077 ± 0.0008	1.2625 ± 0.0019
0.8	1.0326 ± 0.0010	1.2887 ± 0.0029
0.9	1.0566 ± 0.0012	1.3135 ± 0.0007
1.0	1.0802 ± 0.0015	1.3358 ± 0.0019
1.2	1.1181 ± 0.0004	1.4231 ± 0.0004

The calculated percentage deviations of the molecular dynamics simulations from the experimental values were found to be 16.9 to 8.3% and 7.6 to 0.3% for $[C_4MIM][BF_4]$ and $[C_4MIM][PF_6]$, respectively. Since $[C_4MIM][PF_6]$ already had a very accurate density with unscaled charges, scaling has a negative impact on the results. $[C_4MIM][BF_4]$ had a density lower than experiment, and thus further scaling increases the error even more, as mentioned above.

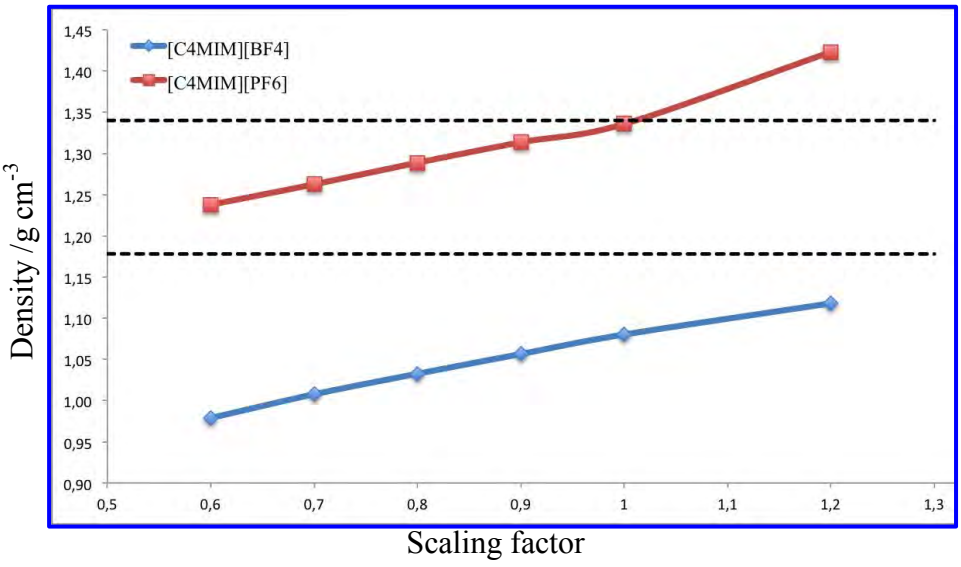

Figure 4.10: Calculated density for $[C_4MIM][BF_4]$ and $[C_4MIM][PF_6]$ at 333.15 K and 1 atm calculate from six different scaling factors.

Shown in figure 4.10 are the calculated densities against each of the scaling factors. Both liquids show a linear change with the scaling factors up to the non-scaled (1.0) model. Chaban has shown that a uniform scaling factor can be determined by looking at density and then applying this to other properties [34], however, this is not feasible here because of the greater error resulting from scaling as discussed above.

Furthermore, in section 4.3.3 and 4.3.4 it was shown that one cannot use a model's ability to predict density alone as an indicator of how well it performs in other areas and interpolating from figure 4.10 to determine a uniform scaling factor may not necessarily be the best practice.

4.4.2 Liquid Structure

Another key question that comes about is that of understanding what changes are being introduced to the system by scaling the charges. An investigation of how the Not product related RDFs change as a result is a good place to start.

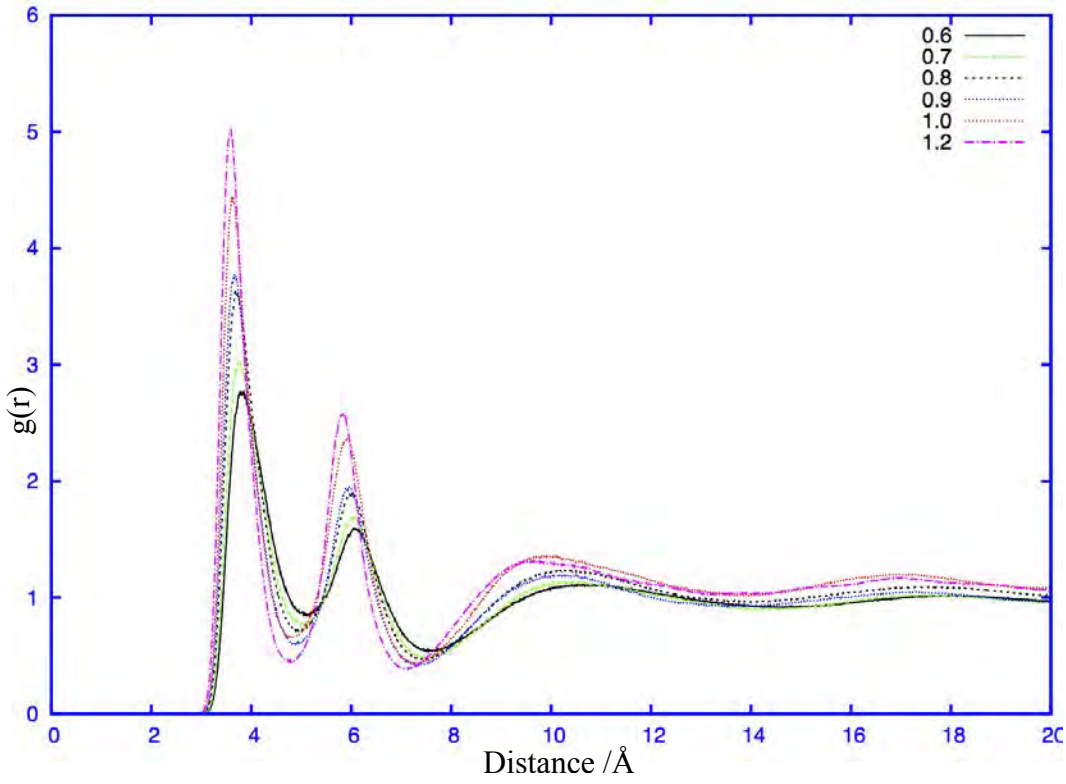

Figure 4.11: C_2-B_1 RDFs for [C_4MIM][BF_4], computed at 333.15 K and 1 atm over a 1 ns period with charges scaled in 0.1 increments from 0.6 to 1.0 and 1.2.

In the 2011 study by Chaban *et al.* on the effects of charge scaling it was concluded that the scaling has no significant impact on the overall observed structure of the liquid [34]. To confirm this observation RDFs between the C_2 atom of the imidazolium ring (see figure 4.1) and the central ion of the corresponding anion were analyzed. These RDFs are shown in figure 4.11 and 4.13.

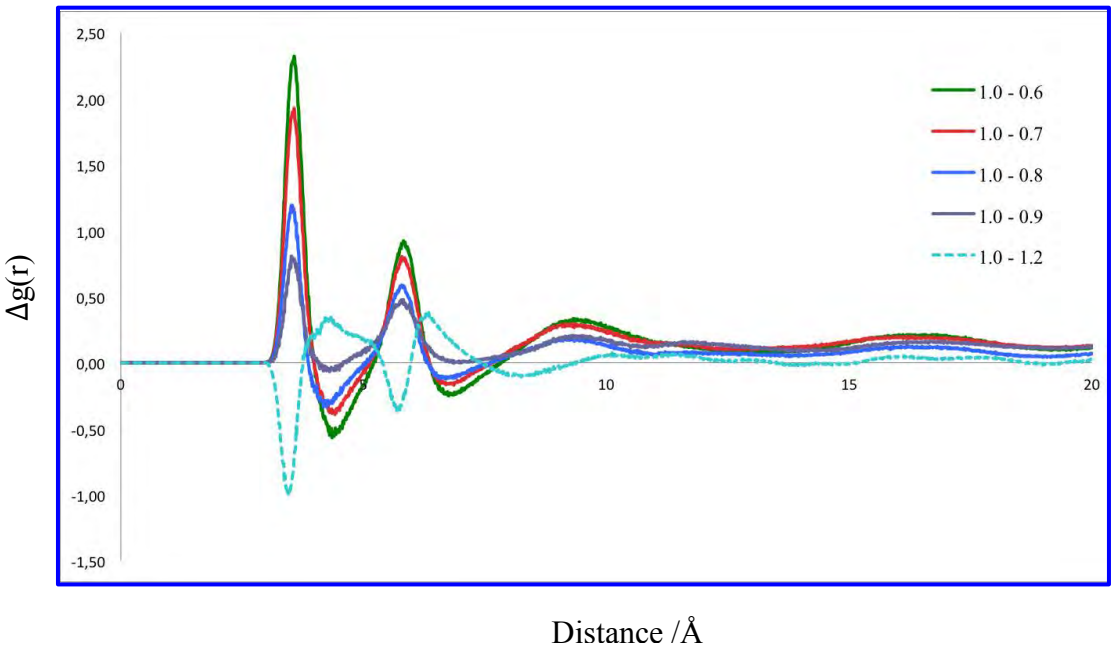

Figure 4.12: ΔRDF, for [C_4MIM][BF_4] (the difference between the 1.0 RDF and each of the scaled charge simulations).

Figure 4.11 shows that the overall structure of the liquid does not change significantly from one scaling factor to the next. In figure 4.12 the change in the RDFs (ΔRDF) was plotted, these were constructed from the difference between the 1.0 RDF and each of the RDFs from the different scaling factors. All the RDFs have a peak of varying height at ~3.8 Å that shifts very slightly to the left going from the 0.6 to the 1.2 scaling factor. The distance between the first two peaks is maintained, indicating uniform structure with the scaling down or up of the charges. Positions of the maxima and minima are shown in table 4.7.

Table 4.7: [C_4MIM][FF_6] RDF maxima and minima.

C_2- X	Position / Å			Coordination No.	
	R_{max1}	R_{min1}	R_{max2}	N_1	N_2
0.6	3.8	5.2	6.2	1.8	5.4
0.7	3.8	5.1	6.1	1.9	5.5
0.8	3.7	5.0	6.1	1.9	5.5
0.9	3.6	5.0	6.0	2.0	5.6
1.0	3.6	4.9	6.0	2.3	5.7
1.2	3.4	4.8	5.9	2.3	5.7

Coordination numbers were calculated and the approximate number of coordinating ions was found to be consistent for all the scaling factors. Youngs and Hardacre showed that decreasing the total charges results in the weakening of the attractive forces that exists between the ions [43]. This is clearly evident in this work as well, the probability of finding an anion next to a cation gradually decreases as the total charge is reduced. It follows that when the overall charge on the ion is increased the model will show stronger interactions. This can be seen in the ΔRDF plots, where the plot corresponding to the 1.0 RDF – 1.2 RDF exhibits a negative value where the initial RDFs had a predicted high probability of cation-anion interaction.

It is interesting to note that even though the probability in the RDFs changes, the number of coordinating ions around C_2 remains similar for the first and second peaks as can be seen in table 4.7. This implies that even though the reduction of charges results in the loss of detail in the RDF [43], the predictions of the overall structure of the liquid remains similar.

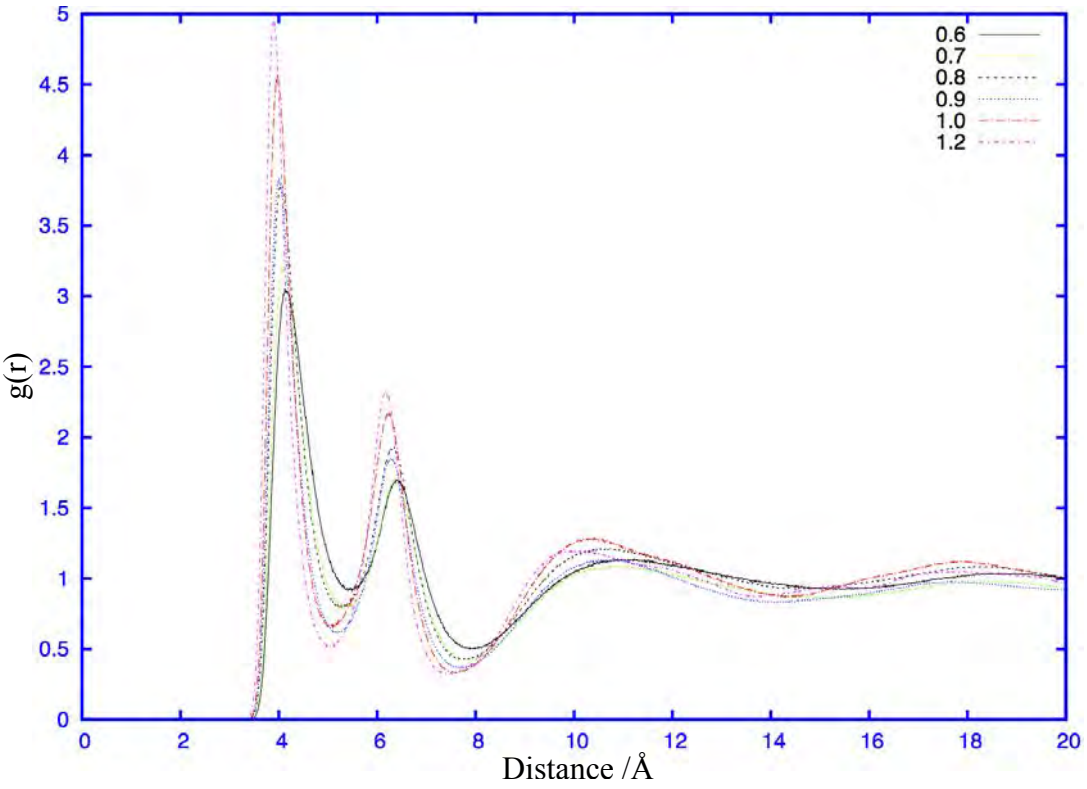

Figure 4.13: C_2-P_1 RDF for [C_4MIM][PF_6] computed at 333.15 K and 1 atm over a 1 ns time period with charges scaled in 0.1 increments from 0.6 to 1.0 and 1.2 calculated.

The change in structure of $[C_4MIM][PF_6]$ exhibits the same properties as that of $[C_4MIM][BF_4]$. Shown in figures 4.13 and 4.14 and table 4.8 are the corresponding data.

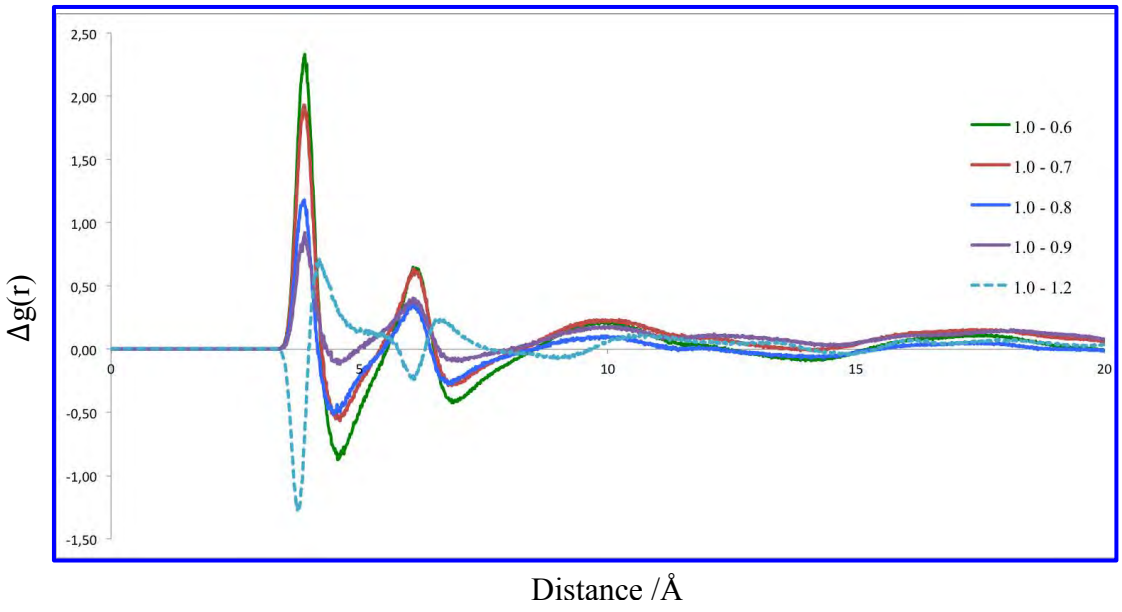

Figure 4.14: ΔRDF of $[C_4MIM][PF_6]$.

Table 4.8: $[C_4MIM][PF_6]$ RDF maxima and minima.

C_2- X	Position / Å			Coordination No.	
	R_{max1}	R_{min1}	R_{max2}	N_1	N_2
0.6	3.8	5.2	6.2	1.9	5.4
0.7	3.8	5.1	6.1	2.0	5.4
0.8	3.7	5.0	6.1	1.9	5.5
0.9	3.6	5.0	6.0	2.0	5.6
1.0	3.6	4.9	6.0	2.2	5.8
1.2	3.4	4.8	5.9	2.0	5.8

4.4.3 Self-Diffusion Coefficients

Section 4.3.3 showed that non-scaled, non-polarisable force fields underestimate self-diffusion coefficients. This result comes about through the overestimation of the interactions that exist within the RTILs. In this section the effect that charge scaling has on the self-diffusion coefficients are reported.

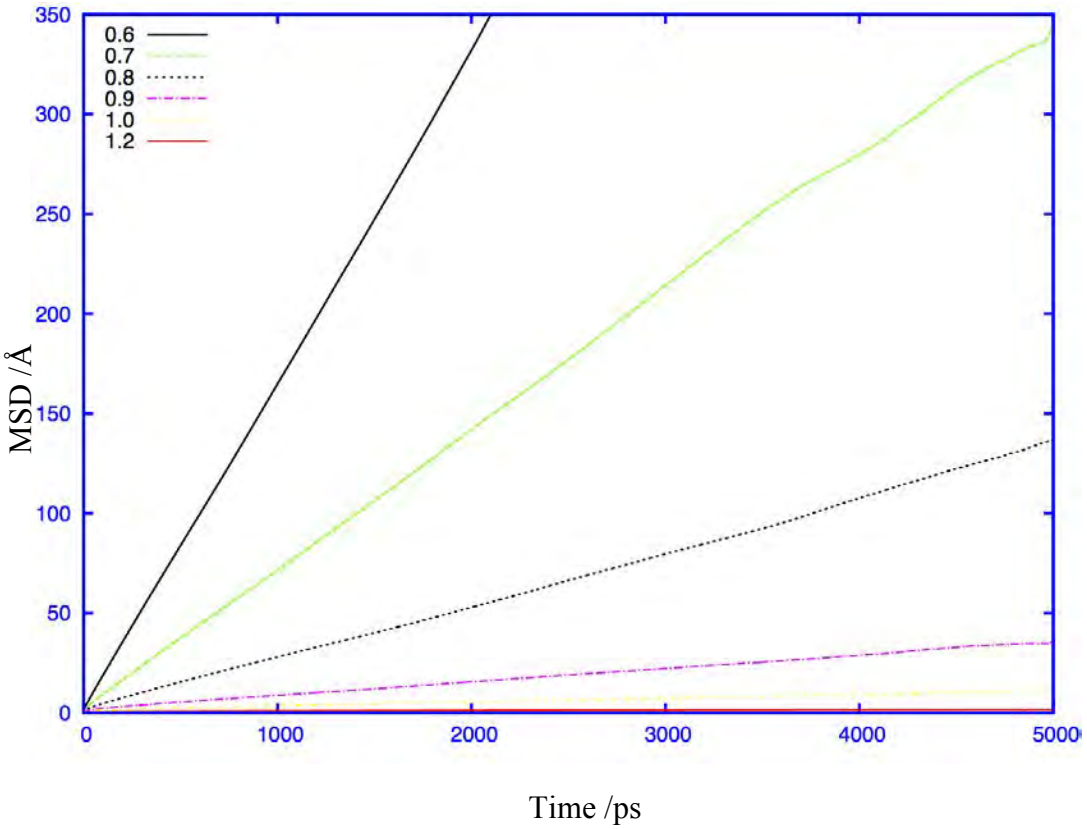

Figure 4.15: MSDs for the cation (C_4MIM) of $[C_4MIM][PF_6]$ calculated with the different scaling factors at a temperature of 333.15 K.

Figure 4.15 shows the calculated MSDs for the different $[C_4MIM][PF_6]$ force fields. The reduction of the total charges on the ions leads to a decrease in the intermolecular attraction between the ions, which results in increased fluidity of the liquid as can be seen in the calculated diffusion coefficients in table 4.9.

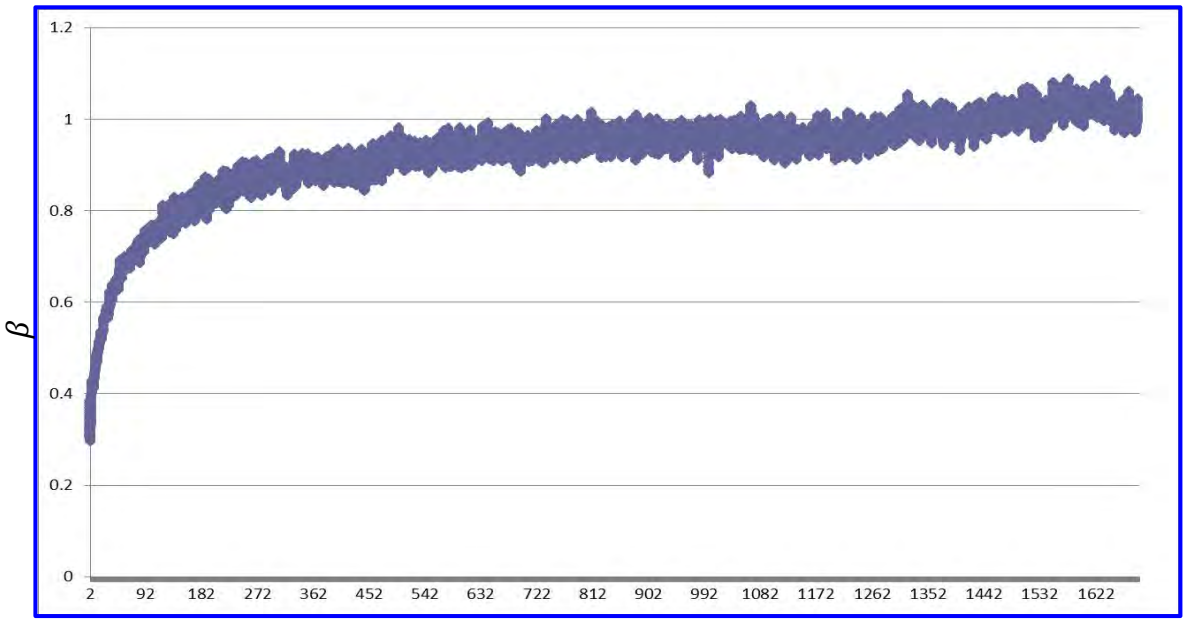

Figure 4.16: The value of β for [C_4MIM][BF_4] as a function of time calculated at 333.15 K from a simulation with charges scaled by 0.8.

Again β values were determined in order to evaluate the diffusive motion of the RTIL systems. Figure 4.10 shows the values for β from a simulation with charges scaled by a factor of 0.8. This plot shows that the simulation reaches its diffusive regime after about 500 ps. The time it takes to reach the linear regime depends on the viscosity, thus with a scale factor of 0.8 and more fluidity comes an earlier linear regime in comparison to the non-scaled dynamics.

An assessment of the self-diffusion coefficients in table 4.9 shows that scaling charges to between 0.8 and 0.9 gives results that are within the range of coefficients calculated from VFT fits to experimental data from reference 5 for both [C_4MIM][BF_4] and [C_4MIM][PF_6].

Table 4.9: calculated self-diffusion coefficients for $[C_4MIM][BF_4]$ at 333.15 K with different scaling factors.

Scaling factor	Diffusion /x 10^{-11} m^2 s^{-1}	
	Anion	Cation
Experiment	5.94	5.91
0.6	43.0 ± 2.32	47.2 ± 4.01
0.7	17.9 ± 0.07	23.8 ± 1.23
0.8	7.02 ± 1.17	8.91 ± 1.63
0.9	1.82 ± 0.33	3.54 ± 0.14
1.0	1.29 ± 0.108	2.43 ± 0.018
1.2	0.0191 ± 0.012	0.0282 ± 0.014

The trend of the calculated self-diffusion coefficients is plotted in figure 4.17. Again it is clear that the anion consistently diffuses at a slower rate than the cation even when charge scaling is applied. Whereas the density change was linear, diffusion coefficients show a much greater change at lower scaling factors. With diffusion considered as an activated process, it is dependent on an activation barrier in an exponential way (as the VFT equation shows). Thus decreasing the activation barrier by decreasing the interionic interaction should show an exponential change in diffusion, as is seen here.

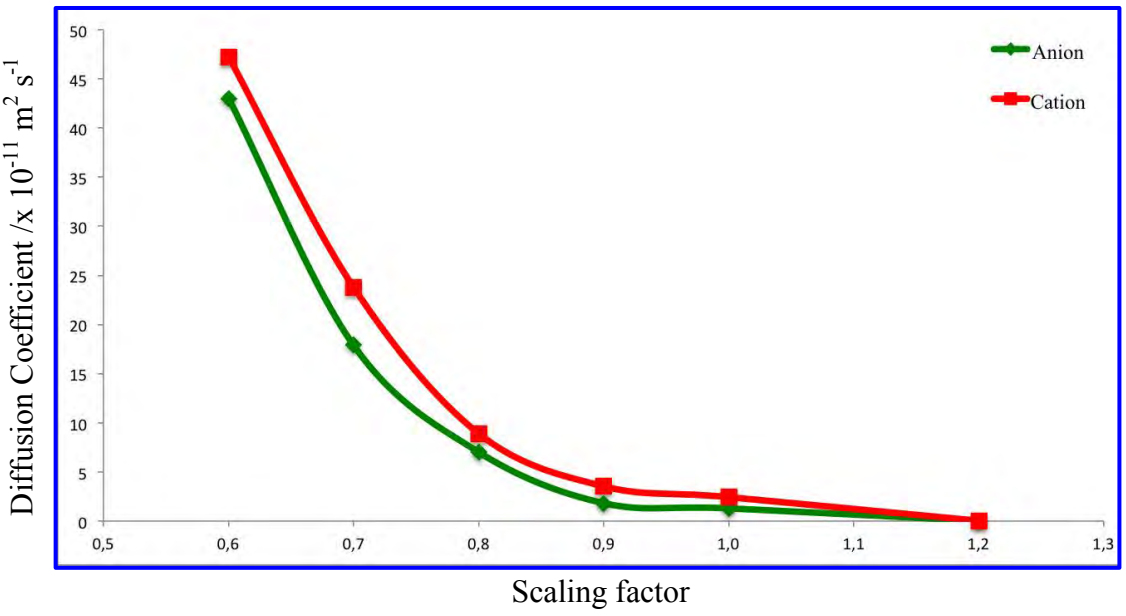

Figure 4.17: Calculated diffusion coefficients for $[C_4MIM][BF_4]$ from each of the scaling factors as a function of time calculated at 333.15 K.

Self-diffusion coefficients were also calculated for $[C_4MIM][PF_6]$ from scaled charge simulation and the calculated values are shown in table 4.10 and represented graphically in figure 4.18.

Table 4.10: calculated self-diffusion coefficients for $[C_4MIM][PF_6]$ at 333.15 K with different scaling factors.

Scaling factor	Diffusion /x 10^{-11} m^2 s^{-1}	
	Anion	Cation
Experimental	2.84	3.65
0.6	27.9 ± 1.06	22.7 ± 2.78
0.7	12.1 ± 0.70	17.9 ± 1.99
0.8	2.26 ± 0.87	4.50 ± 0.29
0.9	0.625 ± 0.004	1.24 ± 0.53
1.0	0.134 ± 0.053	0.268 ± 0.074
1.2	0.0358 ± 0.022	0.0422 ± 0.034

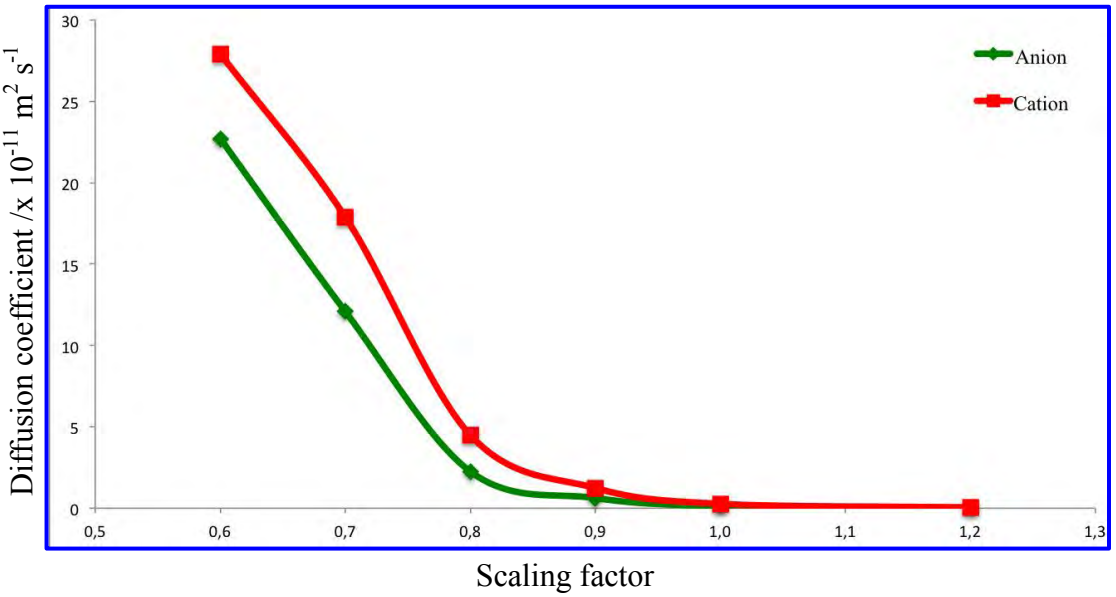

Figure 4.18: Calculated diffusion coefficients for $[C_4MIM][PF_6]$ RTIL from each of the scaling factors as a function of time calculated at 333.15 K.

From this data it can be seen that the mobility of the ions in both $[C_4MIM][BF_4]$ and $[C_4MIM][PF_6]$ increases as the overall charge on the ions is scaled down.

Empirically, a scaling factor that would give the best results for transport properties can be obtained from the optical dielectric constant (ε_∞), $S = \frac{1}{\sqrt{\varepsilon_\infty}}$ (see section 2.2.4 for the origins of this expression). The optical dielectric constant can be calculated from the refractive index, n, as $\varepsilon_\infty = n^2$. $[C_4MIM][BF_4]$ and $[C_4MIM][PF_6]$ have a refractive index of 1.37 and 1.84, respectively [43,44]. Thus it follows that the scaling factors that would be ideal for the modeling of these RTILs from a bulk shielding argument should be lower than what was found here, 0.730 and 0.543.

4.5.3 Viscosity

We again calculated viscosity using both the Green-Kubo and Einstein equation. The protocol was the same as that discussed in section 4.3.4. Similar to the self-diffusion coefficients, the 0.8 scaling factor gives the best viscosity estimates for $[C_4MIM][BF_4]$. In the case of $[C_4MIM][PF_6]$ there was a greater difference in the results from the two methods. The Green-Kubo method overestimated the viscosity, predicting 69.2 mPas where the Einstein relationship gives a viscosity of 46.03 mPas, which is much closer to the experimentally determined value of 59 mPas. It is interesting to note that a change of 0.1 in the overall charge on the ions can lead to a doubling, in some cases more, of the predicted viscosity estimate. Viscosity estimates were not calculated from the force field with charges scaled by 1.2 as the pressure-pressure time correlation function for these systems had not converged even after 40 ns worth of MD simulations.

Table 4.11: Viscosities for $[C_4MIM][BF_4]$ and $[C_4MIM][PF_6]$ at 333.15 K with different scaling factors.

Scaling factor	Viscosity / mPa s			
	$[C_4MIM][BF_4]$		$[C_4MIM][PF_6]$	
	Green-Kubo	Einstein	Green-Kubo	Einstein
Experimental	31 [13] (22.5)*		59 [13] (45.3)*	
0.6	3.3 ± 0.8	3.68 ± 0.945	12.8 ± 1.9	7.43 ± 0.19
0.7	8.7 ± 1.3	6.95 ± 2.16	23.2 ± 4.2	19.6 ± 1.45
0.8	29.3 ± 5.8	28.08 ± 1.07	69.2 ± 7.6	46.03 ± 5.78
0.9	64.2 ± 9.0	65.81 ± 3.95	265.7 ± 20.5	287.4 ± 68.4
1.0	158.6 ± 16	145 ± 59.2	682 ± 128	526.8 81.2
1.2	-	-	-	-

* *Experimental viscosity calculated using Tokuda's VFT fits at 333.15 K.*

In figure 4.19 the calculated viscosity estimates for both $[C_4MIM][BF_4]$ and $[C_4MIM][PF_6]$ are compared graphically.

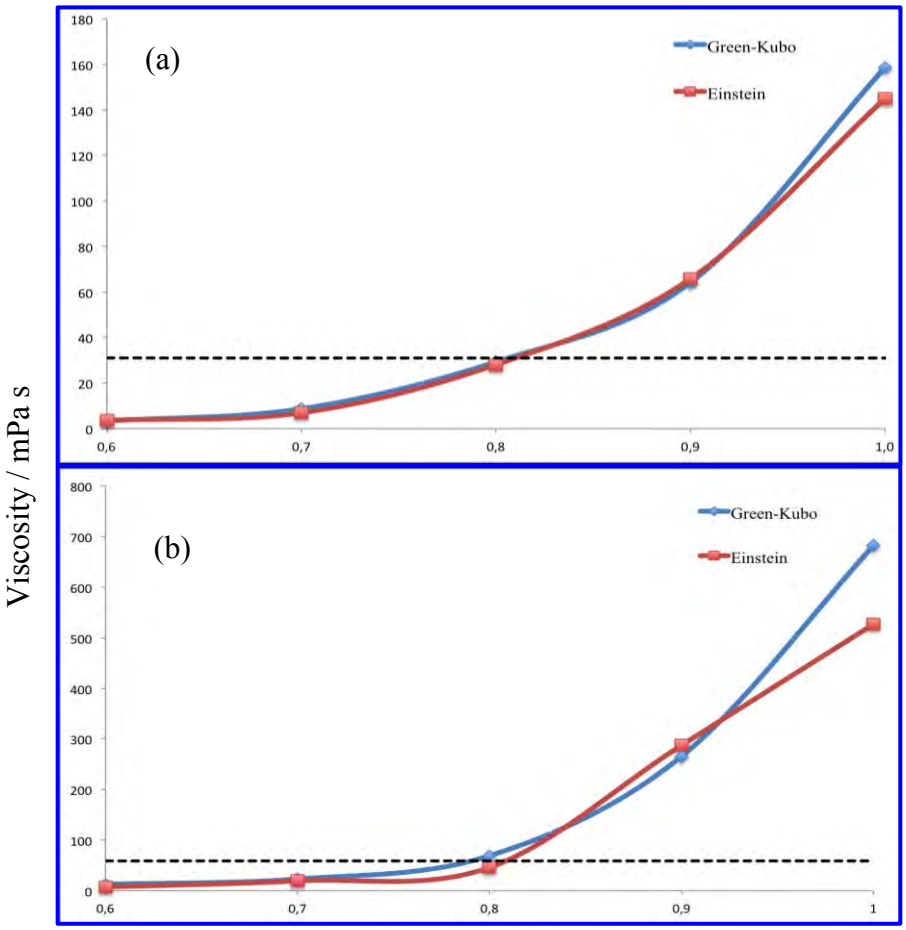

Figure 4.19: Calculated viscosity estimates for (a) $[C_4MIM][BF_4]$ and (b) $[C_4MIM][PF_6]$ from each of the scaling factors at 333.15 K and 1 atm using the Green-Kubo and Einstein method.

From the plots it can be seen that the trend for the calculated viscosity estimates is the same using the Green-Kubo or the Einstein relationship. The reduction of charge results in increased mobility of the ions of the liquid.

4.5 References

1. L. Martínez, R. Andrade, E. G. Birgin, J. M. Martínez, J. Comp. Chem., 2009, **30**, 2157 - 2164.
2. T. Koddermann, Chem. Phys. Chem. 2008, **9**, 1851 – 1858.
3. M. Mondello, G. Grest, J. Chem. Phys., **106**, 1997, 9327 – 9335.
4. C. Cadena, Q. Zhao, R. Q. Snurr, E. J. Maginn, J. Phys. Chem. B 2006, **110**, 2821-2832.
5. H. Tokuda, K. Hayamizu, K. Ishii, J. Phys. Chem. B, 2004, **108**, 16593 – 16600.
6. J. Lopes, A. Pádua, J. Phys. Chem. B, 2004, **108**, 16893 – 16898.
7. M. Del Popolo, G. Voth G, J. Phys. Chem. B, 2004, **108**, 1744 – 1752.
8. P. Wasserscheid, T. Welton, Ionic liquids in synthesis, Second edition, 2008,WILEY_VCH Verlags GmbH & Co. KGaA, Weinheim.
9. S. Urahata, M. Ribeiro, J. Phys. Chem. B, 2004, **120**, 1855 – 1862.
10. Z. Liu, T. Chen, A. Bell, B. Smit, J. Phys. Chem. B 2010, **114**, 4572–4582.
11. Z. Gu, J. Brennecke, J. Chem. Eng. Data, 2002, **47**, 339.
12. Z. Lui, S. Huang, W. Wang, J. Phys. Chem. B, 2004, **108**, 12978 -12989.
13. D. Tomida, A. Kumagai, K. Qiao, C. Yokoyama, J. Thermophysics, 2006, **27**,39 – 47.
14. A. Mackrell, J. Wiorkiewicz-Kuczera, M. Karplus, J. Am. Chem. Soc., 1995,**117**, 11946.
15. L. Martinez, R. Andrade, E. Birgin, J. Martinez, J. Comput. Chem., 2009, **30**,2157 – 2164.
16. T. A. Darden, D. M. York, L. G. Pedersen, J. Chem. Phys. 1993, **98**, 10089.
17. U. Essmann, L. Perera,M. L. Berkowitz, T. Darden, H. Lee, L. G. Pedersen, J. Chem. Phys. 1995, **103**, 8577.
18. S. Tsuzuki, W. Shinod, H. Saito, M Mikami, H, Tokunda, M. Watanabe, J.Phys. Chem. B., 2009, **113**, 10641 – 10649.
19. F. Dommert, J. Schimdt, B. Qiao, Y. Zhao, Krekeler, L Site Delle, R. Berger, C. Holm, J. Chem., 2008, **129**, 224501.
20. T. Chen, B. Smit, A. Bell, J. Chem. Phys., 2009, **131**, 246101.
21. B. Hess, J. Chem. Phys., 2002, **116**, 209 – 217.
22. M. Mondello, G. Grest, J. Chem. Phys., 1997, **106**, 9327 – 9335.

23. T. Yan, C. Burnham, M. Del Popolo, G. Voth, J. Phys. Chem. B., 2004, **108**,11877 – 11881.
24. T. Morrow, E Maginn, J. Phys. Chem. B, 2002, **106**, 12807 – 12813.
25. J. Lopes, J. Deschamps, A. Padua, J. Phys. Chem. B, 2004, **108**, 2038 – 2047.
26. P.A. Hunt, Mol. Simul., 2006, **32**, 1 – 10.
27. O. Borodin, G. D. Smith, J. Phys. Chem. B, 2006, **110**, 11481 – 11490.
28. R. Prado, L.C. Freitas, J. Mol. Structure: THEOCHEM, 2007, **847**, 93 – 100.
29. C. J. Margulis, H. A. Stern, B. J. Berne, J. Phys. Chem. B, 2002, **106**, 12017 -12021.
30. A Bagno, F. DÁmico, G. Saielli, J. Mol. Liq., 2007, **131-132**, 17 -23.
31. D. Zhao, Z. Fei, R. Scopelliti, P. Dyson, J. Inorg. Chem., 2004, **43**, 2197.
32. D.W. Armstrong, L. He, Y. S. Lui, J. Anal. Chem., 1999, **71**, 3873.
33. J. Canongia Lopes, J. Deschamps A. Padua, J. Phys. Chem. B, 2004, **108**, 2038 – 2047.
34. V. V. Chaban, I. V. Voroshylova, O. N. Kalungin, Phys. Chem. Chem. Phys., 2011, **13**, 7910 – 7920.
35. J. J. Wang, Y. Tian, Y. Zhao, K. Zhuo, K. Green Chem. 2003, **5**, 618.
36. Y. Zhong, E. J. Maginn, J. Phys. Chem. B. 2012, **116**, 10036 – 10048.
37. T. Yan, C. J. Burnham, M. G. Del Popolo, G. A. Voth, J. Phys. Chem. B, 2004, **108**, 11877 – 11881.
38. P. J. Daivis and D. J. Evans, J. Chem. Phys., 1994, **100**, 541.
39. H. Liu, E. Maginn, J. Chem. Phys., 2011, **135**, 124507.
40. V. Chaban, Phys. Chem. Chem. Phys., 2011, **13**, 16055 – 16062.
41. C. Rey-Castro, A. L. Tormo, F. L. Vega, J Phys. Chem. B 2006, **110**, 14426.
42. K. R. Seddon, A. Stark, M. Torres, Pure Appl. Chem., 2000, **72**, 2275 – 2287.
43. T. G. A. Youngs, C. Hardacre, Chem. Phys. Chem., 2008, **9**, 1548 – 1558.
44. Y. Jeon, J. Sung, C. Sed, H. Lim, H. Cheong, M. Kang, B. Moon, Y. Ouchiand, D. Kim, J. Phys. Chem. B, 2008, **112**, 4735 – 4740.

CHAPTER 5

Force Field Model with Self-Consistent Condensed Phase Charges

5.1 Introduction

In the previous chapter we saw that the partial charges assigned to each of the atoms making up the ions in a room temperature ionic liquid model play a very critical role in how the model behaves and in the physicochemical properties predicted by the model. In classical MD simulations partial charges are typically assigned to atoms from a gas phase QM calculation as it was carried out in the sections leading up to this chapter.

Ionic liquids are composed of charged species and thus very strong electrostatic interactions exist within the liquid. In MD simulations these electrostatic interactions are treated using Coulomb's law and the charge distribution for each ion is used to determine the overall contribution to the electrostatic interactions.

In a 2008 study by Klähn and co-workers, the development of a force field for Guanidinium-based ionic liquid that makes use of an electronic charge distribution derived from an actual liquid was published [1]. In 2012 Zhang and Maginn also proposed a study where they used an AIMD approach to derive atomic charges for an ionic liquid system [2]. In both of the above mentioned studies the focus of the work done was in aid of coming up with alternative and potentially better way to determine partial atomic charges for the simulation of RTILs.

Traditionally partial atomic charges for RTIL force fields are derived from first principle QM calculations, using the one-particle electron density approach; this approach is based on fitting atomic point charges to reproduce the Electrostatic Potential (ESP). Since their inception ESP methods have been subjected to issues in reproduction of the fitted charges, these issues come about as a result of strong dependence on molecular orientation and conformation and not being transferable between common groups in homologous molecules [1, 3 - 5].

A variety of solutions have been suggested to overcome these shortcomings, [4,5] the most effective solutions have been those that rely on constraining the fitting procedure to reproduce a target molecular property such as the dipole moments, a charge on a non-hydrogen atom or the quadrupole moments [4,6]. These algorithms are known as Restrained Electrostatic Potential (RESP) methods.

There are three major algorithms that are typically used to calculate partial atomic charges for RTILs: ChelpG [16,17], Connolly (commonly referred to as Merz-Kollman [7] charges) and the Geodesic [7] algorithm. The key difference between the three algorithms is the manner in which points for the fitting procedure are selected on the ESP surface.

In chapter 4 we made use of the Connolly (Merz-Kollman, MK) algorithm to fit partial atomic charges on the ions of the RTILs under investigation. In this algorithm a spherical surface of points is computed around each atom at a probe radius chosen as a multiple of the van der Waals radius [22]. The molecular surface is produced by combining individual atomic surfaces and discarding the points within the chosen multiples of the van der Waals radius of any of the atoms [5]. For a detailed description of the ChelpG and Geodesic algorithms the reader is directed to references 16 and 18, respectively.

The MK and ChelpG schemes are notorious for their structural dependence and as such the Geodesic scheme was developed to smooth out the positions of the Connolly points, eliminating shortcomings of the Connolly scheme. The geodesic scheme has been shown to produce partial atomic charges that have a reduced dependence on structural properties [18].

In this chapter we introduce a charge fitting methodology of our own design and compare it to the charge fitting scheme used in the previous chapter, namely the MK scheme, for the completeness of the study. We then take steps towards improving the newly established charges.

5.2 Computational details

5.2.1 Charge Fitting Methodology

In this section we develop a charge fitting methodology based on an average condensed or bulk phase system. The QM/MM engine that we will adopt makes use of the GAMESS-UK package, which does not have a standard procedure implemented for calculating Merz-Kollman (MK) charges similar to what was done in the previous chapter. New gas phase charges, referred to as Density Fitted (DF) charges were thus calculated using the GAMESS-UK package

The methodology was first applied to individual ions in the gas phase, after which frames were selected from a molecular dynamics simulations with a hybrid QM/MM Hamiltonian and external points charges to polarise the QM region. The general QM fitting procedure is discussed in this section. Adjustments made when computing condensed phase consistent charges are discussed in section 5.4.1.

Coordinates of individual ions were read into either GAMESS-UK (for gas phase calculations) or CHARMM/GAMESS-UK, where CHARMM 35 and GAMESS-UK [23] were interfaced for a hybrid simulation (QM/MM) as discussed in chapter 3. The quantum mechanical calculation was done at the HF/6-31G(d) level of theory and the geometry optimised. The steps that follow can be broken down into three phases and the phases are as follows: to start off, a Self-Consistent Field (SCF) calculation is performed [25].

In the second phase the electron density is generated on a 30 Å 3D grid after which the electrostatic potential is calculated at the 0.002, 0.00175, 0.00150 and 0.00125 au isodensity surfaces. The surfaces were chosen to replicate the Connolly or Merz-Kollman type methodology. In the final phase the potential derived charges are then generated from the potential points generated in phase two while the overall charge is constrained to +1 or -1 for the cation and anion, respectively.

5.2.2 Molecular Dynamics

Molecular dynamics were run according to the protocol outlined in Chapter 4 with the exception of partial atomic charges, nonbonded parameters were kept unchanged from those reported in Chapter 4. Partial charges on each of the atoms were calculated from ab initio generated electrostatic potential using the methodology described in section **5.2.1**.

5.3 Results and Discussion

5.3.1 Physicochemical Properties: Comparison between Charge Schemes (MK vs DF)

5.3.1.1 Potential Derived charges

Figure 5.1 shows a schematic representation of the calculated charges on heavy atoms using the MK and DF methodology and in figure 5.2 we show a comparison of all the calculated charges. The two schemes produce charges that are of similar signs on all atoms, although differences in magnitude of up to 0.2 e were found. In general the DF scheme underestimates the charges, which results in the ions having a more uniform charge distribution. Different transport properties, as will be discussed later in the chapter, should thus be expected. The charges on atoms C_4 and C_5 differ by 0.137 and 0.068 e^- respectively, but are both negative. The proximity of the non-polar butyl chain to C_5 clearly leads to a more neutral charge in both schemes when fitting to the overall potential. Carbon C_2 is situated in-between two electron withdrawing nitrogen atoms and it possesses a slightly more positive charge in comparison to carbon C_4 and C_5. Whereas the MK scheme results in this charge being negative, -0.193 e, in the DF scheme it is close to neutral.

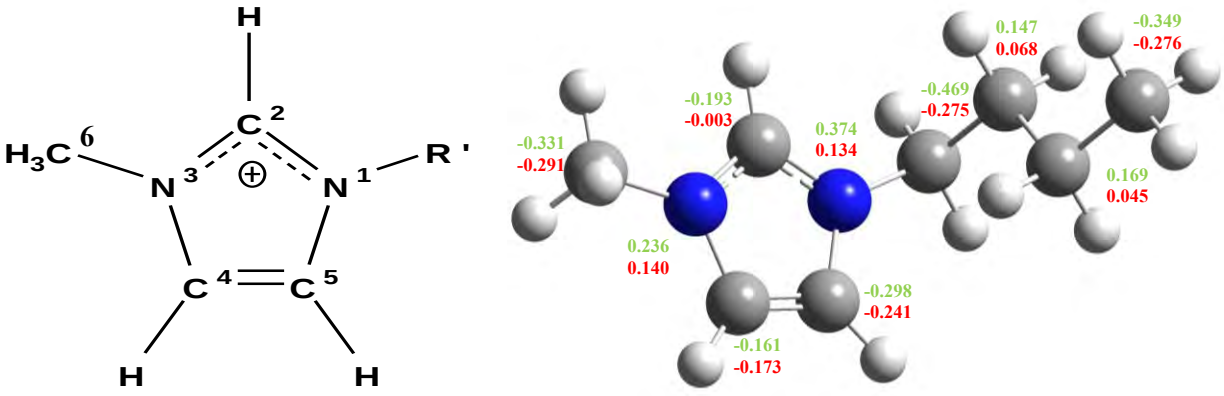

Figure 5.1: C_4MIM cation with partial atomic charges fitted using the MK and DF charge fitting schemes (charge on hydrogen atoms not shown).

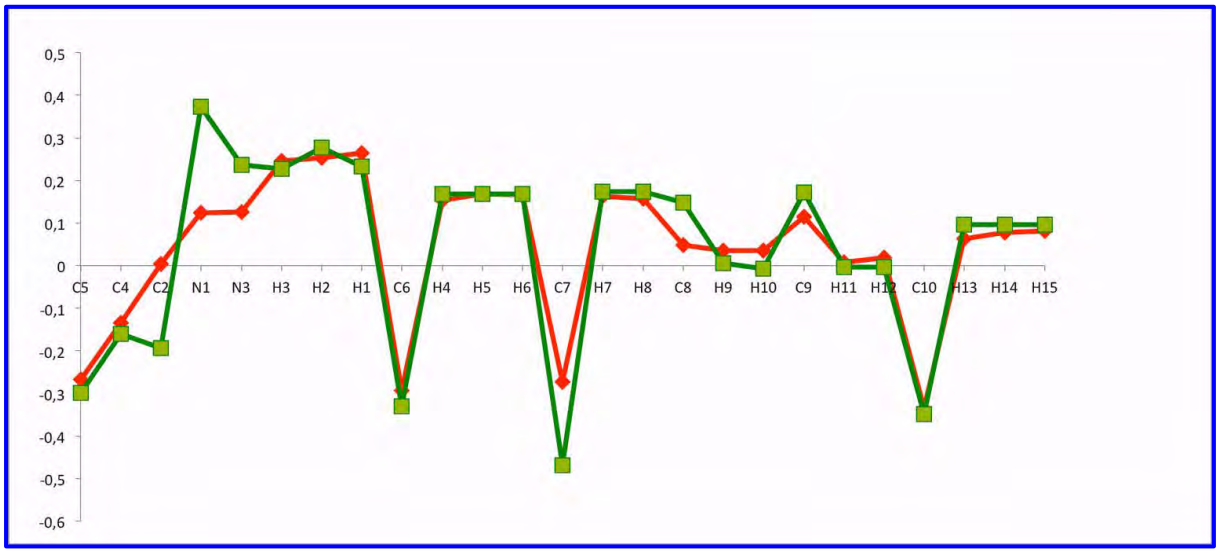

Figure 5.2: Partial charges fitted on a C_4MIM cation in the gas phase using the MK (in green) and DF (in red) methodology.

Previous studies have shown that the anion positions itself around the C_2-H bond in the liquid. The DF scheme predicts a more positive charge of 0.257 on H_2 and combined with a significantly less negative charge on C_2, should greatly enhance interaction at this position.

A key difference between the two nitrogen atoms in the imidazolium ring is the length of the alkyl chains attached to each. MK predicts a discrepancy of approximately 0.2 e^- in the charges on the nitrogen atoms, whereas the DF scheme predicts the two to possess an

approximately equal charge. Previous studies have shown that partial charges fitted on the C_4MIM cation using the ChelpG scheme result in the nitrogen having similar charges while the MK and Geodesic methodology report a discrepancy between these atoms [24]. A full set of the charges fitted on the atoms is shown in appendix A5.1.

It is important to note that the fitted charges rely heavily on the structure used and caution should be taken especially if one seeks to compare individual atoms within a molecule. A classic example is that of the butyl chain that has the ability to rotate and bend away and toward the ring changing the local environment of the ring. This problem can be solved by using average charges over several conformations. When fitting charges in the presence of external point charges later in this chapter, we will address this problem in this way.

Both anions, BF_4 and PF_6, used in this study are symmetrical molecules and as such no major differences were noted in the charges fitted for each of the anions. Although the magnitude of the charges again differed by about 0.2 e, however, the trends in the fitted charges remained unchanged.

Having produced a new charge set for the cations and these are now put to test in their ability to predict transport properties.

5.3.1.2 Density

Table 5.1 shows the density of RTILs predicted from molecular dynamics simulations using the two charge schemes disused in section 5.3.1.1 and the values predicted from experiments.

Table 5.1: liquid densities for $[C_4MIM][BF_4]$ and $[C_4MIM][PF_6]$ at 333.15 K.

	Density /g.cm^{-3}	
	$[C_4MIM][BF_4]$	$[C_4MIM][PF_6]$
Simulation (MK)	1.080 ± 0.0012	1.336 ± 0.0019
Simulation (DF)	1.081 ± 0.0031	1.342 ± 0.0023
Experiment	1.178 [13]	1.340 [13]

As far as the prediction of the liquid density goes, no charge scheme is found to perform significantly better than the other. The calculated percentage deviations are 8.3 and 0.3 % for $[C_4MIM][BF_4]$ and $[C_4MIM][PF_6]$, respectively, using the MK charges and 8.2 and 0.15 % for $[C_4MIM][BF_4]$ and $[C_4MIM][PF_6]$, respectively, using DF charges.

5.3.1.3 Liquid Structure

Radial distribution functions were calculated for the assessment of the changes in the liquid structure due to the change in charge distribution arising from the newly established charge set. As was the case with scaled charges, no significant changes were observed in the overall structure of the liquid as result of the change in the partial charges and thus the RDFs are not shown here.

5.3.1.4 Self-Diffusion Coefficients

In this section we compare the same force field substituting the MK charges with DF charges. Since the overall cation/anion charge is ±1, transport properties are expected to still be overestimated in both cases.

Table 5.2 shows a summary of the diffusion at 333.15 K, using the exact same computational procedure as before.

Table 5.2: Calculated self-diffusion coefficients /x10^{-11} m^2s^{-1} for $[C_4MIM][BF_4]$ and $[C_4MIM][PF_6]$ at 333.15 K.

	$[C_4MIM][BF_4]$/x10^{-11} m^2s^{-1}		**$[C_4MIM][PF_6]$/ x10^{-11} m^2s^{-1}**	
	Anion	Cation	Anion	Cation
Simulation (MK)	1.29 ± 0.0108	2.43 ± 0.018	0.134 ± 0.00053	0.268 ± 0.00074
Simulation (DF)	0.984 ± 0.036	1.87 ± 0.053	0.0823 ± 0.025	0.126 ± 0.057
Experiment [5]	5.94	5.91	2.84	3.65

The DF charge scheme predicts much slower dynamics in comparison to the MK charge scheme. For $[C_4MIM][BF_4]$ the predicted self-diffusion coefficients are approximately 25% slower for both cation and anion . Deviations from experiments are 68.4 and 83.4 %, respectively.

$[C_4MIM][PF_6]$ also exhibits slower diffusion when simulated with DF charges, the cation and anion deviating by 53 and 38.5 % from MK charges and 96.5 and 97.1 % from experiments, respectively.

The self-diffusion coefficient results obtained point to the fact that MK charges outperform DF when used in MD simulations to reproduce transport properties. A possible explanation could be the enhanced interaction around C_2-H that was mentioned earlier. In the sections that follow we build on the newly derived DF charges, a key focus in this study, whereby we let the RTIL in the bulk phase inform the partial charges fitted on the atoms.

5.4 Condensed Phase Consistent (CPC) Charges

5.4.1 Deriving Partial Charges in the Condensed phase

To derive partial charges in the condensed or bulk phase several snapshots of an MD simulation were extracted and were used as starting coordinates for hybrid QM/MM calculations of the system. This was carried out for individual ions and ions pairs within the bulk phase.

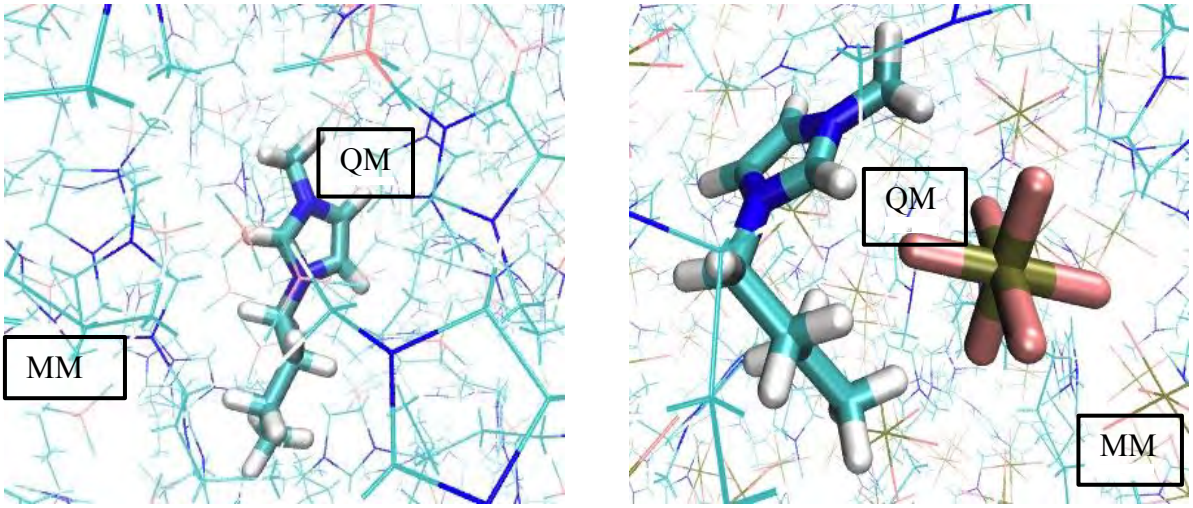

(a) (b)

Figure 5.3: Partitioning of the simulated ionic liquid systems treated with a classical force field (MM – surrounding stick-like molecules) and a fragment treated with QM (bold molecule) for QM/MM calculations. (a) QM fragment that contains only one ion for the evaluation of electric Polarisation. (b) Structure optimized with the QM/MM method, where the QM fragment encompasses an ion pair to analyze electron charge transfer between ions.

From a one nanosecond trajectory we extracted 200 frames spaced 100 (i.e. 0.05 ps) frames apart in order to capture the varying number of conformations that the ions may exist in. The full set of coordinates was read into CHARMM/GAMESS-UK after which a central ion was selected and the simulation box re-centered around this ion. The central ion is treated quantum mechanically and is relaxed in 10 steps of Newton-Raphson optimisation. The

remainder of the ions in the liquid were treated with molecular mechanics, as shown in figure 5.3, and their MM charges were included in the calculation of the electrostatic potential and the electron density of the QM region. This procedure was then continued iteratively. The selection of the central ion was set up such that if a cation was selected in the first run, an anion would be selected next and the process would continue in this manner. After each run the calculated charges were applied to the MM region and assessed for convergence; convergence was defined as a change less than 0.002 e^- between successive iterations. Where fitted charges had not converged, the new charges were applied back into the simulation and the process repeated. In practice it was found that convergence was achieved well within ten steps on each of the cation or anion. This process is carried out for all selected 200 frames and an average charge is calculated from all of the frames. This algorithm is shown in a flow diagram in figure 5.4

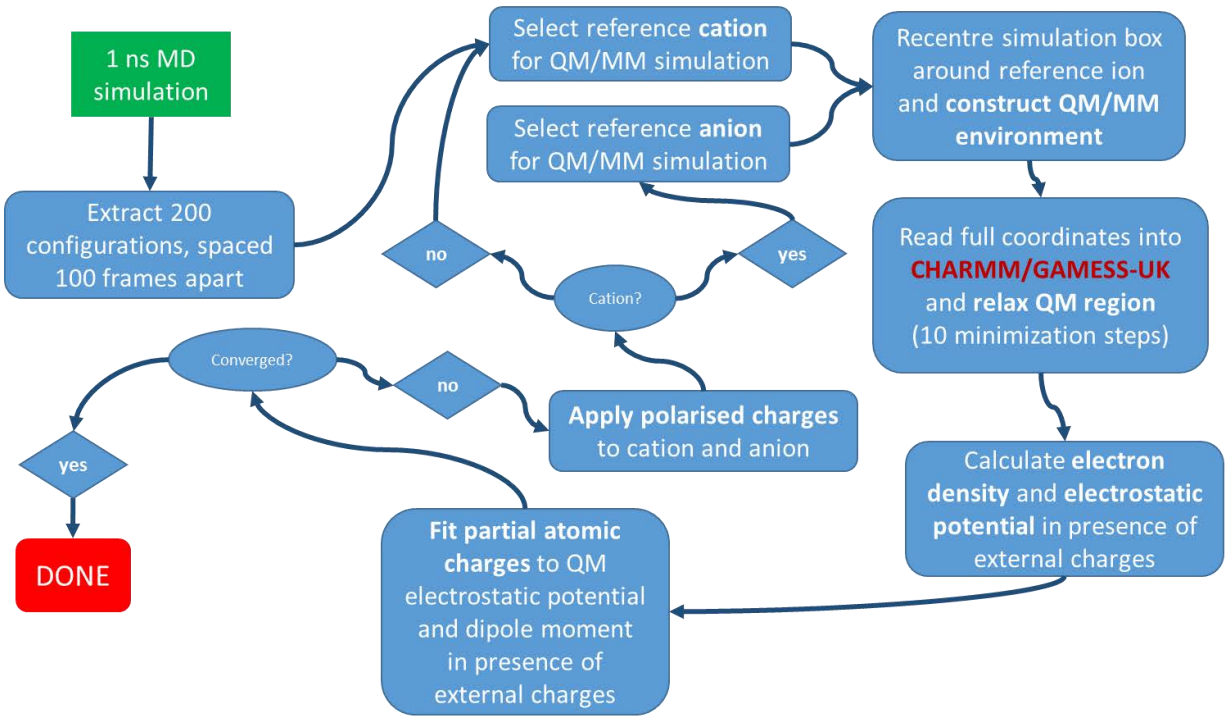

Figure 5.4: Flow diagram of the charge fitting methodology used in computing Condensed phase consistent charges.

5.5 Results and Discussion

5.5.1 Physicochemical Properties: Comparison between Charge Schemes (DF vs CPC)

In section 5.3.1 we saw how the density fitted (DF) charges compare against the Merz-Kollman (MK) charges used in the previous chapter. The overall performance of DF charges was worse compared to the MK charges even though the fitted charges using both methodologies followed a similar trend. The work carried out in this section is in aid of improving the quality of the DF charges and in turn leads to the reproduction of physicochemical properties from simulations that are comparable to experimentally determined values. These charges we will refer to as condensed phase consistent charges (CPC).

5.5.1.1 Potential Derived charges

Shown in figure 5.5 is a C_4MIM cation with the fitted atomic charges using both the DF and CPC methodology. A full set of the charges fitted on the atoms is shown in appendix A5.1.

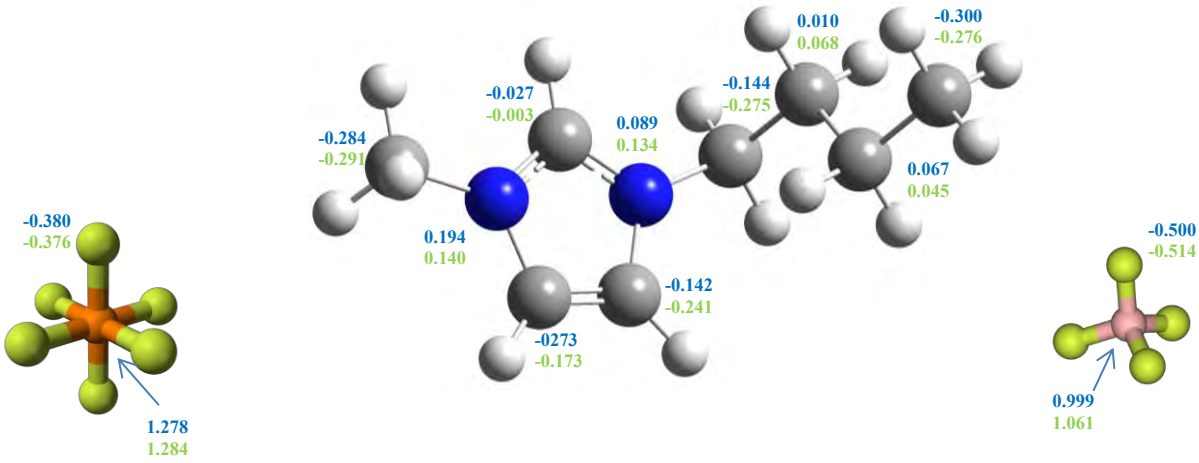

Figure 5.5: C_4MIM cation with partial atomic charges fitted using the CPC and DF charge fitting schemes (charge on hydrogen atoms not shown).

An analysis of the fitted charges (shown in figure 5.6) shows that no trend is maintained going from DF to CPC charges. Although there are significant changes (changes greater than 0.02 e^-) in the charges fitted on the butyl alkyl chain and on the imidazolium ring, the difference in the fitted charges between the two schemes are much less than that between MK and DF.

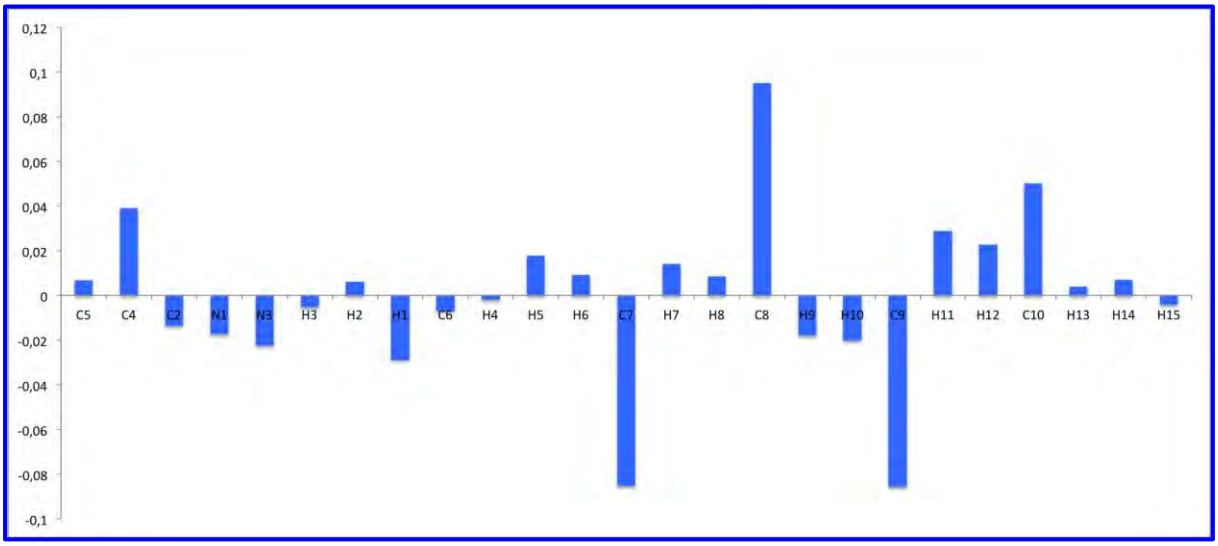

Figure 5.6: The difference in the partial charges fitted on a C_4MIM cation using the Density Fit (DF) and Condensed Phase scheme (CPC).

The figures that follow, figure 5.7 to 5.10, show histograms of the partial atomic charges fitted on some of the atoms over the frames used to calculate the CPC charges. We only show the histograms of the atoms that had the greatest deviations when comparing the two schemes. The C_2 and N_3 histograms follows a normal distribution and the nitrogen and carbon atom were found to be positive in approximately 85% of the frames. On the other hand, the C_4 and C_7 atoms consistently carried a negative charge (with latter atom had a positive charge in 1 out of 200 frames) and in both cases the distribution was slightly skewed to higher negative values. Overall, the histograms are indicative of an average showing small to moderate deviations from the mean, confirming that the selected frames provide a true reflection of the fluctuating charge distribution that is expected to be present in the condensed phase.

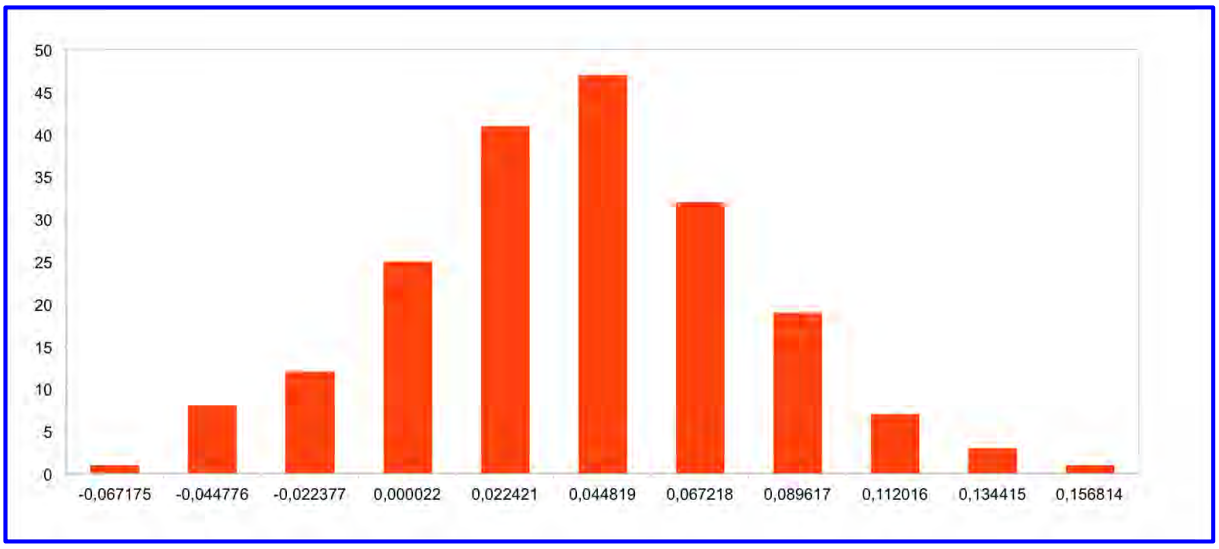

Figure 5.7: A histogram of charges fitted on the C_2 atom of a C_4MIM cation in the condensed phase scheme.

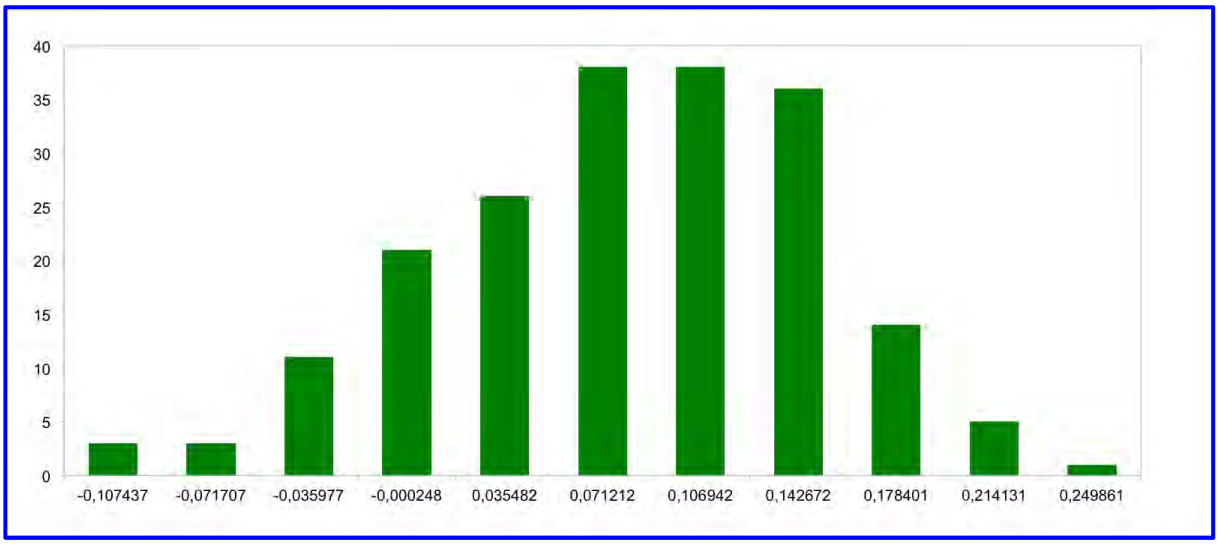

Figure 5.8: A histogram of charges fitted on the N_3 atom of a C_4MIM cation in the condensed phase scheme.

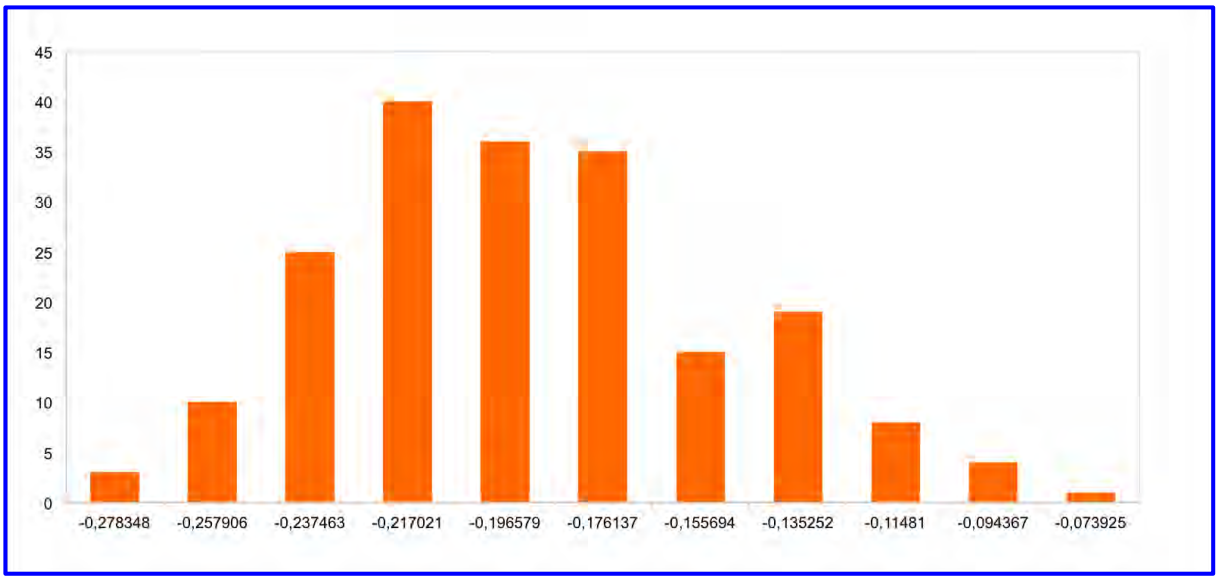

Figure 5.9: A histogram of charges fitted on the C_4 atom of a C_4MIM cation in the condensed phase scheme.

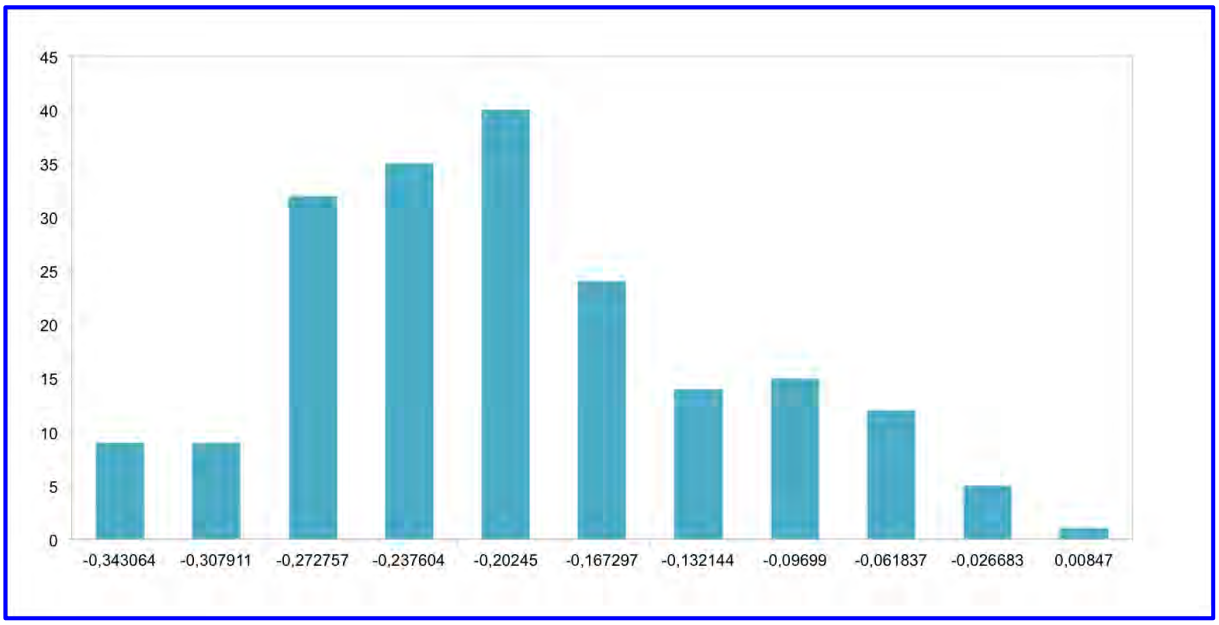

Figure 5.10: A histogram of charges fitted on the C_7 atom of a C_4MIM cation in the condensed phase scheme.

5.5.2 Force field with Self-Consistent Charges

As noted before, there were no significant changes in the overall structure and the liquid density of the RTILs going from DF charges to CPC charges and thus the results obtained for these calculations are only shown in the appendix (appendix **A5.3**). Self-diffusion coefficients were used as a proxy to assess the effectiveness of the charge fitting scheme.

5.5.2.2 Self-Diffusion Coefficients

Shown in table 5.4 is a comparison of the calculated self-diffusion coefficients from MD simulation making use of condensed phase consistent charges (CPC), DF charges and self-diffusion coefficients calculated from experiment.

Table 5.4: Calculated self-diffusion coefficients /x10^{-11} m^2s^{-1} for $[C_4MIM][BF_4]$ and $[C_4MIM][PF_6]$ at 333.15 K.

	$[C_4MIM][BF_4]$/x10^{-11} m^2s^{-1}		**$[C_4MIM][PF_6]$/ x10^{-11} m^2s^{-1}**	
	Anion	Cation	Anion	Cation
Simulation (DF)	0.984 ± 0.036	1.87 ± 0.053	0.823 ± 0.025	1.26 ± 0.057
Simulation (CPC)	3.74 ± 0.00172	4.67 ± 0.0022	1.17 ± 0.00448	1.56 ± 0.00352
Experiment [5]	5.94	5.91	2.84	3.65

There is a clear improvement in the transport properties, most notably for $[C_4MIM][BF_4]$, this may be due to the ions being of different sizes. A similar result was obtained in the work carried out in references 7 and 8, the authors showed that significant improvements can be made in the physicochemical properties predicted from simulations which use the bulk phase of the RTIL to inform the atomic charges to be fitted on the atoms.

In a more recent study by Mondal and Balasubramanian [25] it was shown that crystal site charges of a RTIL in simulation can be used to refine a force field and in turn improve the predicted physicochemical properties [30].

It is a generally accepted that force fields that do not explicitly include polarisation fail to accurately predict physical properties due to the fact that mean ion charges in the molten or condensed phase may be less than unity, this lesser charge may be a result of either charge transfer and/or polarisation. The methodology we have applied in this section provides a computationally inexpensive alternative to implicitly account for polarisation effects. It might be possible to achieve even better results by taking charge transfer into account, as was done in Chapter 4. In the final section of this chapter, this option is briefly explored.

5.5.3 Electron Charge Transfer Analysis

For the analysis of charge transfer an ion pair with overall charge of zero was selected and partial atomic charges were fitted on both the cation and anion as a whole.

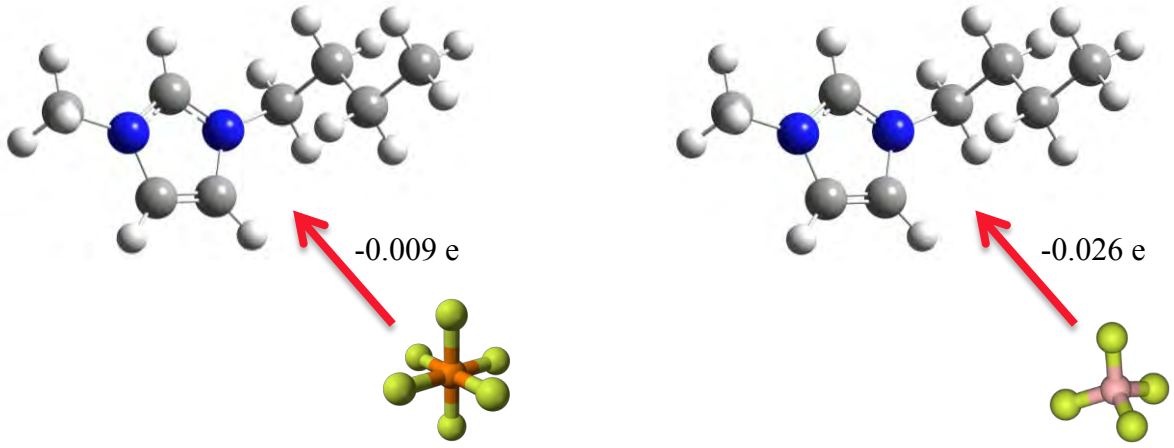

Figure 5.11: Schematic representation of observed charge transfer in $[C_4MIM][BF_4]$ and $[C_4MIM][PF_6]$.

Following the same procedure as before, the atomic charges converged after 50 iterations. The trends in the charge distribution of the ions remained unchanged and they exhibited only a small degree of charge transfer. Table 5.5 shows the overall charges on each of the cations and anions of both liquids.

Table 5.5: Overall fitted charges on ions pairs of $[C_4MIM][BF_4]$ and$[C_4MIM][PF_6]$.

	Charge /e
	Cation/Anion
$[C_4MIM][BF_4]$	± 0.984
$[C_4MIM][PF_6]$	± 0.991

Due to the small charge transfer obtained, MD simulations using the charges fitted in this section were not carried out for the assessment of physicochemical properties of the liquid. Choi *et al.* assessed a $[C_4MIM][BF_4]$ RTIL for charge transfer using a force field based on symmetry-adapted perturbation theory (SAPT) analysis and found charge transfer to be negligible [31]. While charge transfer has been found to be negligible here, it has been shown to exist in other RTILs and may be heavily dependent on the specific ions. For instance in the work of Wendler *et al*., using a charge scheme different to that employed in this work, a significant charge transfer of 0.4 e was shown to occur between the anions and cations of 1,3-dimethylimidazolium chloride $[C_1MIM][Cl^-]$, 1-ethyl-3-methylimidazolium thiocyanate $[C_2MIM][SCN]$ and 1-ethyl-3-methylimidazolium dicyanamide $[C_2MIM][DCA]$ [32]. It is also worth noting that various charge schemes may lead to varying results with regards to charge transfer analysis as can be seen in the works of Choi *et al.* [31] and Wendler *et al.* [32].

5.6 References

1. M. Klahn, A. Seduraman, and P. Wu, J. Phys. Chem. B, 2008, **112**, 10989-11004
2. Y. Zhang and E. J. Maginn, J. Phys. Chem. B 2012, **116**, 10036−10048
3. C. A. Reynolds, J. W. Essex and W. G. Richards, J. Am. Chem. Soc., 1992, **114**, 9075–9079.
4. U. C. Singh and P. A. Kollman, J. Comput. Chem., 1984, **5**, 129–145.
5. R. J. Woods and R. Chappelle, J. Mol. Struct., 2000, **527**, 149–156
6. C. Chipot, B. Maigret, J. L. Rivail and H. A. Scheraga, J. Phys. Chem., 1992, **96**, 10276–10284
7. B. H. Besler, K. M. Merz and P. A. Kollman, J. Comput. Chem., 1990, **11**, 431–439
8. C. I. Bayly, P. Cieplak, W. Cornell and P. A. Kollman, J. Phys. Chem., 1993, **97**, 10269–10280
9. W. D. Cornell, P. Cieplak, C. I. Bayly and P. A. Kollmann, J. Am. Chem. Soc., 1993, **115**, 9620–9631
10. J. Schmidt, C. Krekeler, F. Dommert, Y. Zhao, R. Berger, L. D. Site and C. Holm, J. Phys. Chem. B, 2010, **114**, 6150–6155
11. C. M. Breneman and K. B. Wiberg, J. Comput. Chem., 1990, **11**, 361–373
12. L. E. Chirlian and M. M. Francl, J. Comput. Chem., 1987, **8**, 894–905
13. M. A. Spackman, J. Comput. Chem., 1996, **17**, 1–18
14. L. Martinez, R. Andrade, E. Birgin, J. Martinez, J. Comput. Chem., 2009, **30**,2157 – 2164
15. Darden, T. A.; York, D. M.; Pedersen, L. G. J. Chem. Phys. 1993, **98**, 10089.
16. Essmann, U.; Perera, L.; Berkowitz, M. L.; Darden, T.; Lee, H.; Pedersen, L.G. J. Chem. Phys. 1995, **103**, 8577
17. A. Mackrell, J. Wiorkiewicz-Kuczera, M. Karplus, J. Am. Chem. Soc., 1995,**117**, 11946
18. M.F. Guest, J.H. van Lenthe, J. Kendrick, K. Schöffel, P. Sherwood, and R.J. Harrison, with contributions from R.D. Amos, R.J. Buenker, M. Dupuis, N.C. Handy, I.H. Hillier, P.J. Knowles, V. Bonacic-Koutecky, W. von Niessen, V.R. Saunders, and

A. Stone. The package is derived from the original GAMESS code due to M. Dupuis, D. Spangler and J. Wendoloski, NRCC Software Catalog, Vol. 1, Program No. QG01 (GAMESS), 1980.

19. J. Rigby, E. I. Izgorodina, Phys. Chem. Chem. Phys., 2013,**15**, 1632-1646
20. A. R. Leach, *Molecular Modelling: Principles and Applications*, Pearson Education, 2001
21. T. G. A. Youngs, C. Hardacre, Chem. Phys. Chem., 2008, **9**, 1548 – 1558
22. T. Yan, C. Burnham, M. Del Popolo, G. Voth, J. Phys. Chem. B., 2004, **108**,11877 – 11881
23. T. Morrow, E Maginn, J. Phys. Chem. B, 2002, **106**, 12807 – 12813
24. J. Lopes, J. Deschamps, A. Padua, J. Phys. Chem. B, 2004, **108**, 2038 – 2047
25. A. Mondal, S. Balasurbramanian, J. Phys. Chem. B, 2014, **118**, 3409 – 3422
26. E. Choi, J. G. McDaniel, J. R. Schmidt, A. Yethiraj, J. Phys. Chem. Lett., 2014, **5**, 2670 - 2674
27. K. Wendler, S. Zahn, F. Dommert, R. Berger, C. Holm, B. Kirchner, J. Chem. Theory Comput., 2011, **7**, 3040 – 3044
28. H. Yu, W. F. van Gunsteren, Comput. Phys. Commun., 2005, **172**, 69
29. P. E. Lopes. B. Roux, A. D. MacKerell Jr., Theor. Chem. Acc., 2009, **124**, 11
30. S. W. Rick, S. J. Stuart, B. J. Berne, J. Chem. Phys., 1994, **101**, 6141
31. J. Rigby and E. I. Izgorodina, Phys. Chem. Chem. Phys., 2013, **15**, 163 -1646
32. K. M. Merz, J. Comput. Chem., 1992, **13**, 749–767

CHAPTER 6

Polarisable Force Field Model

6.1 Introduction

The methods investigated in chapters 4 and 5 include the linear scaling of partial atomic charges and the use of partial charges derived from a condensed ionic liquid system.

All these remedies are aimed at computationally efficient methods of adjusting the charge distribution in a manner that accounts for changes that occur due to environmental effects; Polarisable models offer the possibility to mimic the induction arising from the perturbation of the electron density due to the environment in which the molecule is engulfed [1,2]. Literature lists three common methods that can be used to introduce polarisation and model instantaneous charge reorganization in a molecular dynamics simulation.

The fluctuating charge model is an example of one such method that has been used to explicitly introduce polarisation into an MD simulation. In this model the positions of the partial atomic charges are kept fixed, however, the strength of these charges changes as a reaction to the changing environment. This method has been applied to a number of systems which include liquid water [3], hydrated ionic melts [4,5] and RTILs [6,7].

The point-polarised dipole model is often used to include polarisation in force fields. The permanent partial atomic charges on each of the atoms becomes a function of an induced dipole, this way the charge distribution is altered as a reaction to the changing molecular electric fields, while keeping the net charge of the rest of the system unchanged as the set of induced dipoles represents an additional neutral charge distribution [9,10]. For further details on the technical aspects of the point-polarised and the fluctuating charge methods of introducing polarisability, the reader is directed to references 3 and 8, respectively.

In the final experimental approach a Drude oscillator model is implemented to mimic polarisation effects. This method represents electronic induction by introducing a pair of charges. A point charge is attached to each polarisable atom using a harmonic spring and the model is also known as the "charge on a spring" model. This model has been applied in the modeling of a range of molecular systems which includes RTILs [11 – 13]. The Drude oscillator model theory is discussed in chapter 3 section 3.6.

6.2 Computational details

Outlined in Table 6.1 is the polarisability given to each of the atoms in the RTILs in the Drude oscillator model, extracted from Reference 3

Table 6.1: Polarisability (α) of all atom types used in the current work (Hydrogen atoms were made nonpolarisable).

Atom	α/ $(Å)^3$
C	1.28860
N	0.97157
F	0.44475
B	1.59841
P	2.63254

Initial configurations of 250 and 300 ion pairs of $[C_4MIM][BF_4]$ and $[C_4MIM][PF_6]$ respectively, were generated for molecular dynamics using Packmol [15] and relaxed using Newton-Raphson minimization. The simulations were carried out using CHARMM 35 in a cubic cell with starting volume chosen to match experimental density. Polarisation of the atoms was mimicked with the aid of the Drude oscillator model, which has been implanted in CHARMM since 2007 [19]. The polarisabilities, α, of each atom can be specified in the topology file. The mobile drude particles were given a mass of 0.1 amu, which is subtracted from the mass of the corresponding "polarisable parent atom" keeping the mass of the molecule constant regardless of the polarisation.

All non-Drude particles were treated with a thermostat with a temperature of 333.15 K, likewise the Drude particles were treated by a thermostat with a temperature of 1 K. Periodic boundary conditions were used in the isothermal-isobaric (NPT) ensemble with a Nose-

Hoover barostat to maintain a pressure of 1.0 atm. The interactions between permanent charges and Drude pairs were excluded between atoms that share a bond or an angle [21]. The interaction between the corresponding Drude pairs is screened by a Thole function according to Reference 22.

The time step was set to 0.1 fs and the VV2 algorithm was used to integrate the equations of motion [28]. The SHAKE algorithm [18] with a tolerance of 1.0×10^{-10} was applied to all bondsrelated to hydrogen. The van der Waals interactions were cut off beyond 14.0 Å and a switching function initiated at 12.0 Å was used to bring the interaction to zero at the cut off distance. Long-range electrostatic interactions were treated with the particle mesh Ewald method [16 - 17]. The thermodynamic properties of the system such as the total energy and velocity were saved every 50 steps. 10 ns production runs were recorded. Of the 10 ns, 5 were regarded as equilibration and the remaining 5 were used to compute liquid densities and average simulation box sizes.

Following the above, canonical (NVT) molecular dynamics simulations were carried out at 333.15 K using the same computational details and the calculated average box size as the volume of the system from the NPT simulation. 50 ns worth of MD simulations were recorded and the first 10 ns were regarded as equilibration. Learnard-Jones parameters, torsion angle and force constants for all the cations and anions used in these simulations were adapted from the CHARMM 27 force field [14].

6.3 Results and Discussion

6.3.1 Density

Table 6.2 shows the predicted densities. In the cases of both RTILs we observed excellent predictive capabilities of the polarisable force field.

Table 6.2: liquid densities for $[C_4MIM][BF_4]$ and $[C_4MIM][PF_6]$.

	Temp /K	**$[C_4MIM][BF_4]$/g.cm^{-3}**	**$[C_4MIM][PF_6]$/ g.cm^{-3}**
Simulated	333.15	1.185 ± 0.00056	1.344 ± 0.00094
Experimental	333.15	1.178 [13]	1.340 [13]

The percentage deviations are 0.6 and 0.3 % for $[C_4MIM][BF_4]$ and $[C_4MIM][PF_6]$, respectively. Borodin [26] developed a systematic polarisable force field model and amongst the ionic liquids considered this study were $[C_4MIM][BF_4]$ and $[C_4MIM][PF_6]$. The developed model proved reliable for the prediction of liquid densities, reporting a 0.8 and 0.3 % deviation for $[C_4MIM][BF_4]$ and $[C_4MIM][PF_6]$, respectively, in simulated densities at 333 K. Our current model shows a slight improvement in the deviation of $[C_4MIM][BF_4]$ from experiment in comparison to the above mentioned study.

The 0.6% deviation exhibited for the $[C_4MIM][BF_4]$ RTIL is a significant improvement from the 8.3% observed for the classical, non-scaled force field model presented in chapter 4. Whereas for the $[C_4MIM][PF_6]$ RTIL the deviation in density prediction observed for classical and polarisable model remained unchanged.

6.3.2 Liquid Structure

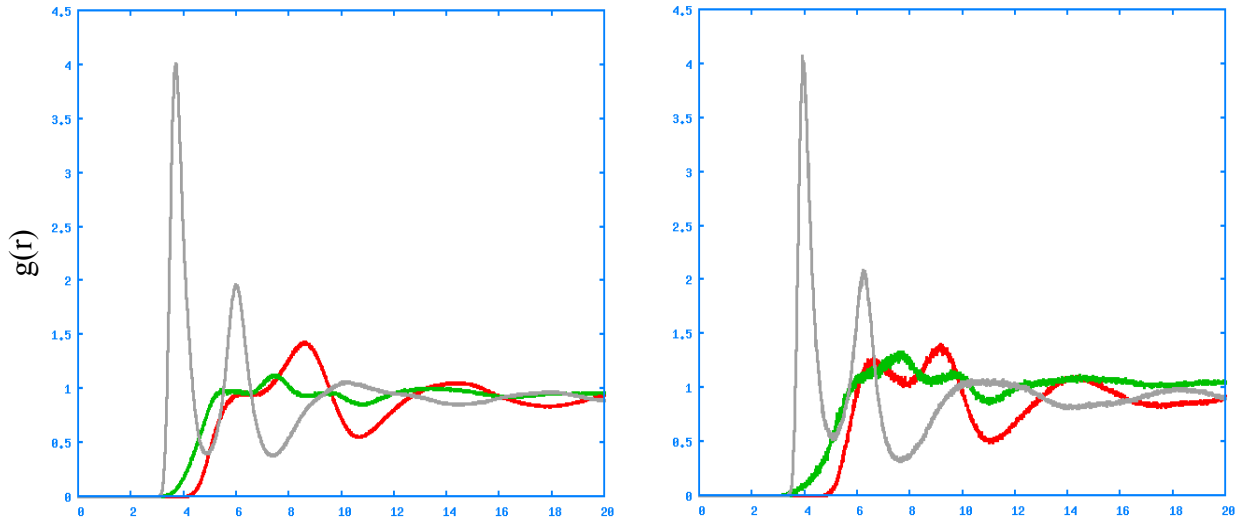

(a) (b)

Figure 6.2: C_2 - C_2, X - X and C_2 - X radial distribution functions for a (a) $[C_4MIM][BF_4]$ and (b) $[C_4MIM][PF_6]$ ionic liquid calculated over a 5 ns trajectory.

The liquid structure described by this model is consistent with that described by the force field models used in the previous sections. The RTILs show an ordering that extends beyond half the length of the simulation box consistent with the long-range interaction that exist within these ionic liquid systems. Shown in table 6.2 are the calculated coordination numbers, maxima and minima positions from the RDFs

According to the $[C_4MIM][BF_4]$ RDF, figure 6.1 (a), of the cation-anion, four peaks are found at 3.6, 4.8, 10.3 and 17.3 Å, respectively. $[C_4MIM][PF_6]$, figure 6.1 (b), also has four peaks at 3.9, 6.2, 10.8 and 17.8 Å. This is similar to those predicted by the other models. The polarisable force field does, however, consistently predict a smaller coordination number, predicting a coordination number of about 2 counterions, similar to the results obtained in chapter 4, for cation-anion ion pairs in the first peak for both the systems under investigation.

Table 6.3: Maximum and minimum positions of a site-site Radial Distribution Functions of RTILs and the first and second shell coordination numbers from a polarisable force field model.

$[C_4MIM][BF_4]$						
	Position[a] / Å				Number of ions	
	$\mathbf{R}_{max1}$	$\mathbf{R}_{min1}$	$\mathbf{R}_{max2}$	$\mathbf{R}_{min2}$	N_1	N_2
X – X	5.9	6.8	8.6	10.4	4.9	15.2
C_2 – C_2	5.4	6.5	7.5	8.2	2.1	14.7
C_2- X	3.6	4.8	6.1	7.6	1.9	5.9
$[C_4MIM][PF_6]$						
X – X	6.6	7.9	9.2	11.2	5.1	15.4
C_2 – C_2	7.6	8.8	9.7	10.9	7.3	14.2
C_2- X	3.9	5.1	6.2	8.9	1.8	5.6

[a]The values tabulated refer to locations of the maximum and minimum of the radial distribution functions.

Cation-cation and anion-anion coordination numbers are also significantly reduced, for instance the classical force field model with non-scaled charges predicts an approximate number of ions within the first solvation shell of a $[C_4MIM][BF_4]$ ionic liquid to be about 30 ions whereas the polarisable model approximates a total of about 8 ions. Although the structuring is very similar, clearly the mobility increase (as is evident from results in the next section) leads to a drop in average coordination number from the RDFs.

6.3.3 Diffusion

Listed in table 6.4 are the diffusion coefficients for $[C_4MIM][BF_4]$ and $[C_4MIM][PF_6]$ calculated from the current Drude oscillator force field model and the experimental determined values at 333.15 K at 1 atm.

Table 6.4: Calculated self-diffusion coefficients /x10^{-11} m^2s^{-1} for $[C_4MIM][BF_4]$ and $[C_4MIM][PF_6]$ at 333.15 K.

	$[C_4MIM][BF_4]$/x10^{-11} m^2s^{-1}		**$[C_4MIM][PF_6]$/ x10^{-11} m^2s^{-1}**	
	Anion	Cation	Anion	Cation
Simulated	2.83 ± 0.017	4.33 ± 0.011	1.52 ± 0.013	1.98 ± 0.021
Experimental[5]	5.94	5.91	2.84	3.65

As far as the diffusion coefficients are concerned the polarisable force model shows the best performance in reproducing the experimentally obtained values. CPC charges were found to perform slightly better for $[C_4MIM][BF_4]$, whereas the polarisable model performs better for $[C_4MIM][PF_6]$. With further refinement one can potentially get predictions of transport properties that rival the expensive polarisable calculations. The predicted diffusion coefficients for the cations and the anions of $[C_4MIM][BF_4]$were found to deviate from experiment by only 26.7 and 52.4%, respectively, a significant improvement from the 78.3 and 58.9% deviation from experiment calculated from the diffusion coefficients obtained using a classical non-polarisable force field model.

Calculated diffusion coefficients for the $[C_4MIM][PF_6]$ RTIL using the polarisable model also showed significant improvement, with the deviations from experimental data 45.8 and 46.5%, for cation and anion respectively. In the systematic polarisable model presented by Borodin [27], self-diffusion coefficients were found to have deviations from experimentally determined values that ranged between 20 - 40%. In the polarisable model presented in this study, deviations from experiments range between 25 – 55%, which in contrast to the models presented in the previous sections, is a significant improvement in terms of reproducing experimental transport properties.

6.4 References

1. V. Chaban, Phys. Chem. Phys., 2011, **13**, 16055 – 16062.
2. C. Schroder, Phys. Chem. Phys., 2012, **14**, 30889 – 3102.
3. T. A. Halgren, W. Damm, Curr. Opin. Struct. Biol.,2001,**11**, 236.
4. M. C. C. Ribeiro, Phys. Rev. B, 2001, **63**, 094205.
5. M. C. C. Ribeiro, J. Chem. Phys., 2010, **132**, 134512.
6. C. Schroder, O. Steinhauser, Phys. Chem. Phys., 2012, **14**, 30889 – 3102.
7. I. V. Vorobyov, V. M. Anisimov, A. D. Mackerell Jr., J. Phys. Chem. B, 2005, 109, 18988 – 18999.
8. S. W. Rick, S. J. Stuart, Rev. Comput. Chem., 2002, **18**, 89.
9. S. J. Stuart, B. J. Berne, J. Phys. Chem., 1996, **100**, 11934 – 11943.
10. D. H. Herce, L. Perera, T. A. Darden, C. J. Sagui, J. Chem. Phys., 2005, **122**, 024513.
11. C Schröder, O. Steinhauser, J. Chem. Phys., 2010, **133**, 154511 – 154523.
12. G. Lamoureux, A. D. MacKerell Jr., B. Roux, J. Chem. Phys., 2003, 119, 10, 5185 – 5197.
13. G. Lamoureux, B. Roux, J. Chem. Phys., 2003, **119**, 3025.
14. G. J. Martyna, M. E. Tuckerman, D. J. Tobias, M. L. Klein, J. CHem. Phys., 1994, **101**, 4177.
15. L. Martinez, R. Andrade, E. Birgin, J. Martinez, J. Comput. Chem., 2009, **30**,2157 – 2164.
16. T. A. Darden, D. M. York, L. G. Pedersen, J. Chem. Phys. 1993, **98**, 10089.
17. U. Essmann, L. Perera,M. L. Berkowitz, T. Darden, H. Lee, L. G. Pedersen, J. Chem. Phys. 1995, **103**, 8577.
18. J. P. Rychaert, G. Giccotti, H. J. C. Berendsen, J. Comput. Phys. 1977, **23**, 327.
19. B. R. Brooks, C. L. Brooks III, A. D. Mackerell Jr, L. Nilsson, R. J. Petrella, B. Roux, Y. Won, G. Archontics, C. Bertels, S. Boresch, A. Caflisch, L. caves, Q. Cui, R. Dinner, M. Feig, S. Fischer, J. gao, M. Hodoscek, W. Im, K. Kuczera, T. Lazaridis, J. Ma, V. Ovchinnikov, E. Paci, R. W. Pastor, C. B. Post, J. Z. Pu, M. York, M. Karplus, J. Comput. Chem., 2009, **30**, 1545.
20. H. Yu, W. F. van Gunsteren, Comput. Phys. Commun., 2005, **172**, 69.
21. P. E. Lopes. B. Roux, A. D. MacKerell Jr., Theor. Chem. Acc., 2009, **124**, 11.
22. S. W. Rick, S. J. Stuart, B. J. Berne, J. Chem. Phys., 1994, **101**, 6141.
23. M. C. Ribeiro, Phys. Rev. B, 2001, **63**, 94205.

24. M. C. Ribeiro, J. Chem. Phys., 2010, **132**, 134512.
25. T. M. Chang, L. X. Dang, J. Phys. Chem. A, 2009, **113**, 2127.
26. D. Bedrov, O. Borodin, Z. Li, G. D. Smith, J. Phys. Chem. B, 2010, **114**, 4984.
27. O. Borodin, J. Phys. Chem. B, 2009, **113**, 11463.
28. Mark E. Tuckerman, Douglas J. Tobias, Michael L. Klein, Mol. Phys., 1996, **87**, 1117 – 1157.

CHAPTER 7

Conclusions

In this study we were able to successfully develop a force field for room temperature ionic liquids using four different approaches. The development was kicked off with a classical non-polarisable force field model, this model made use of static whole charges on all ions making up the liquid. Using this model the density, diffusion, viscosities were calculated and an assessment of the liquid structure of the RTILs was carried out.

The non-polarisable model made use of single ion gas phase charges derived in Gaussian 03 and it was found to suffer shortcomings in predicting the dynamic properties of the liquid and as such our first attempted at overcoming the apparent shortcomings, the commonly used charge scaling methodology was employed. Atomic charges were scaled down linearly in ±0.1 intervals from ±1.0 to ±0.6 e and the inverse, i.e. scaling up of atomic charges, was assessed by scaling the unity charge to ±1.2 e. When partial atomic charges are scaled down, the electrostatic interactions are reduced, leading to an increase in the mobility of the ions in the liquid. As a result the scaling down of atomic charges results in an increase in the mobility of the ions in the liquid. For both [C_4MIM][BF4] and [C_4MIM][PF6] at 333.15 K the 0.6 scaling factor was found to predict dynamic results that are the best comparable to experimental data.

Next, a more physical methodology was used to assign atomic charges. With the aid of CHARMM 35 interfaced to GAMESS-UK for QM/MM calculations, atomic charges were assigned based on a bulk phase system. Initially the charge fitting scheme, which differs slightly from the standard MK scheme, was used on individual ions in the order to allow for comparison to the MK charges calculated earlier.

The newly established charges were tested in MD simulations for the their ability to prediction of dynamic properties of [C_4MIM][BF_4] and [C_4MIM][PF_6] and were found to perform poorly in contrast to MK charges used in chapter 5. A result of little concern to the study, as the aim of the work was to improve on these atomic charges established from single ions in the gas phase. Further work was carried out on these charges using an iterative process to fit partial atomic charges using RTILs in the conceded phase. The revealed that for [C_4MIM][BF_4] and [C_4MIM][PF_6] little evidence of charge transfer.

Partial charges assigned from bulk phase models attempts to include polarisation effects implicitly in the simulation, with some success. To conclude the study, the explicit inclusion of polarisation was also explored. To achieve this, the Drude oscillator model was used. Although the resulting model was found to perform better in the prediction of diffusion coefficients, it comes at significant computational cost. The CPC model would therefore make an effective and viable alternative to include polarisation when long simulation times are required and computational resources are limited.

APPENDIX

A4.1 Charge Scaling - Liquid Structure

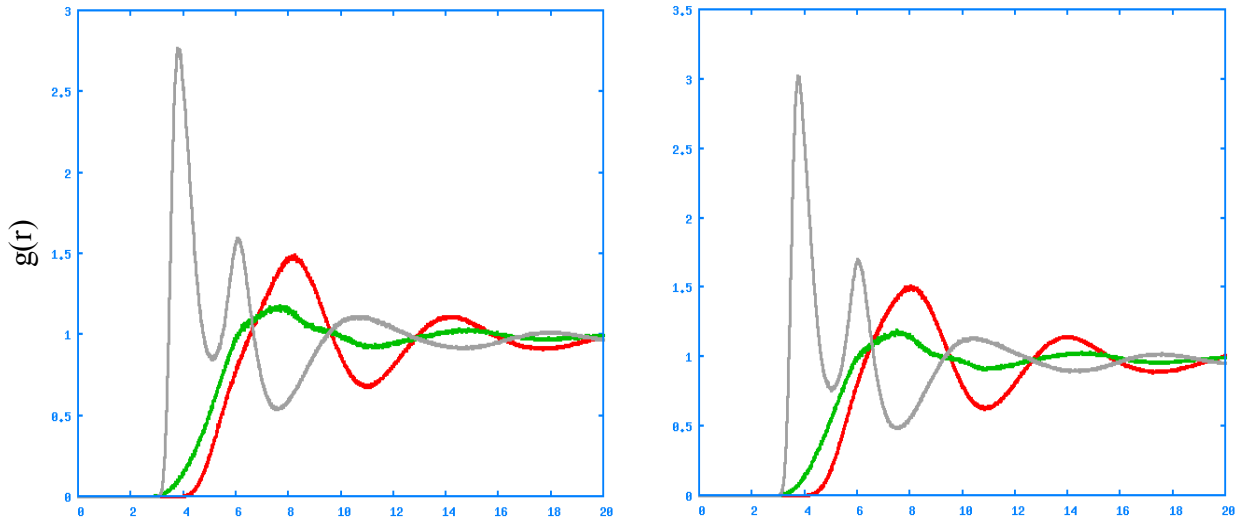

Scaling factor ± 0.6 Scaling factor ± 0.7

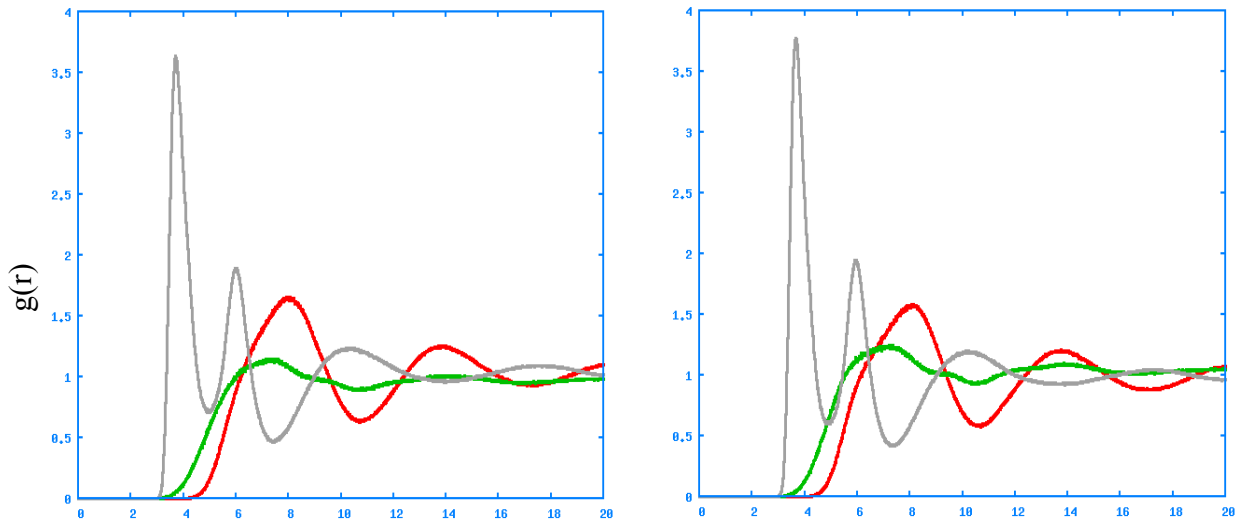

Scaling factor ± 0.8 Scaling factor ± 0.9

Continues on next page…

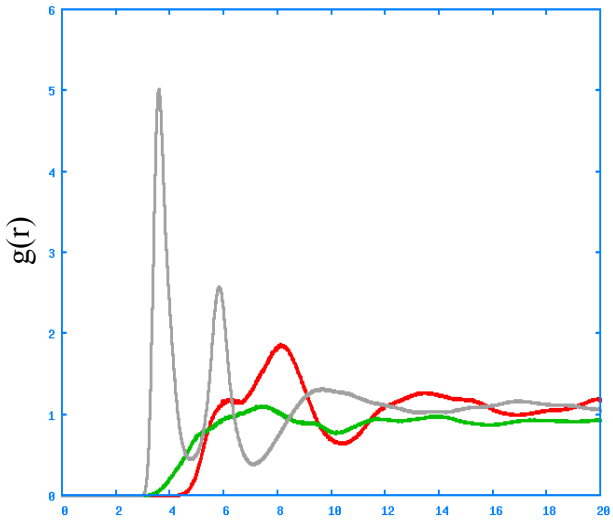

Scaling factor ± 1.2

Figure A4.1: cation-cation, anion-anion and cation-anion radial distribution functions for a $[C_4MIM][BF_4]$ ionic liquid calculated over a 5 ns trajectory.

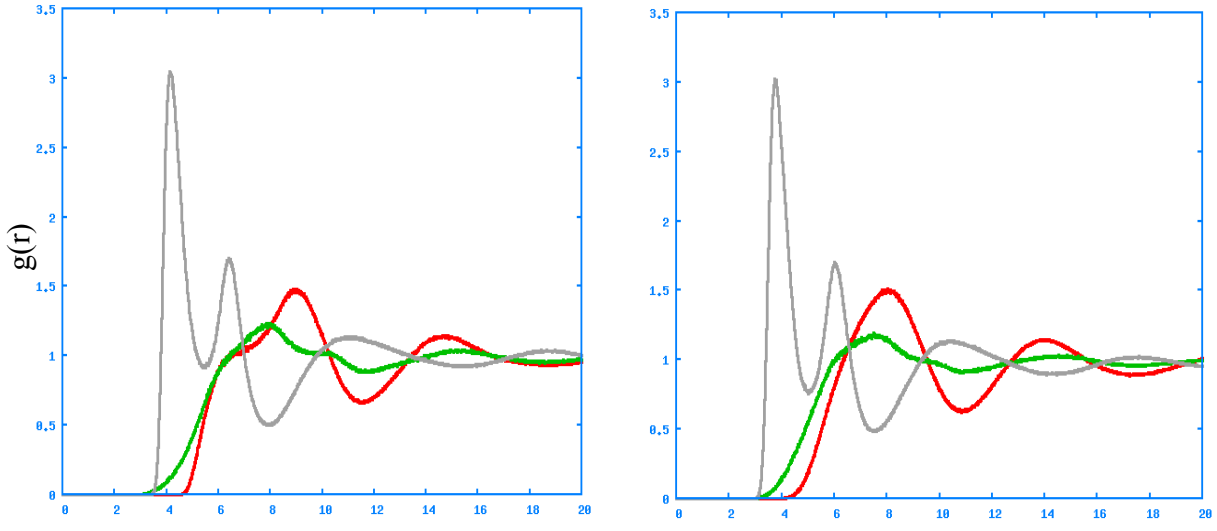

Scaling factor ± 0.6

Scaling factor ± 0.7

Continues on next page…

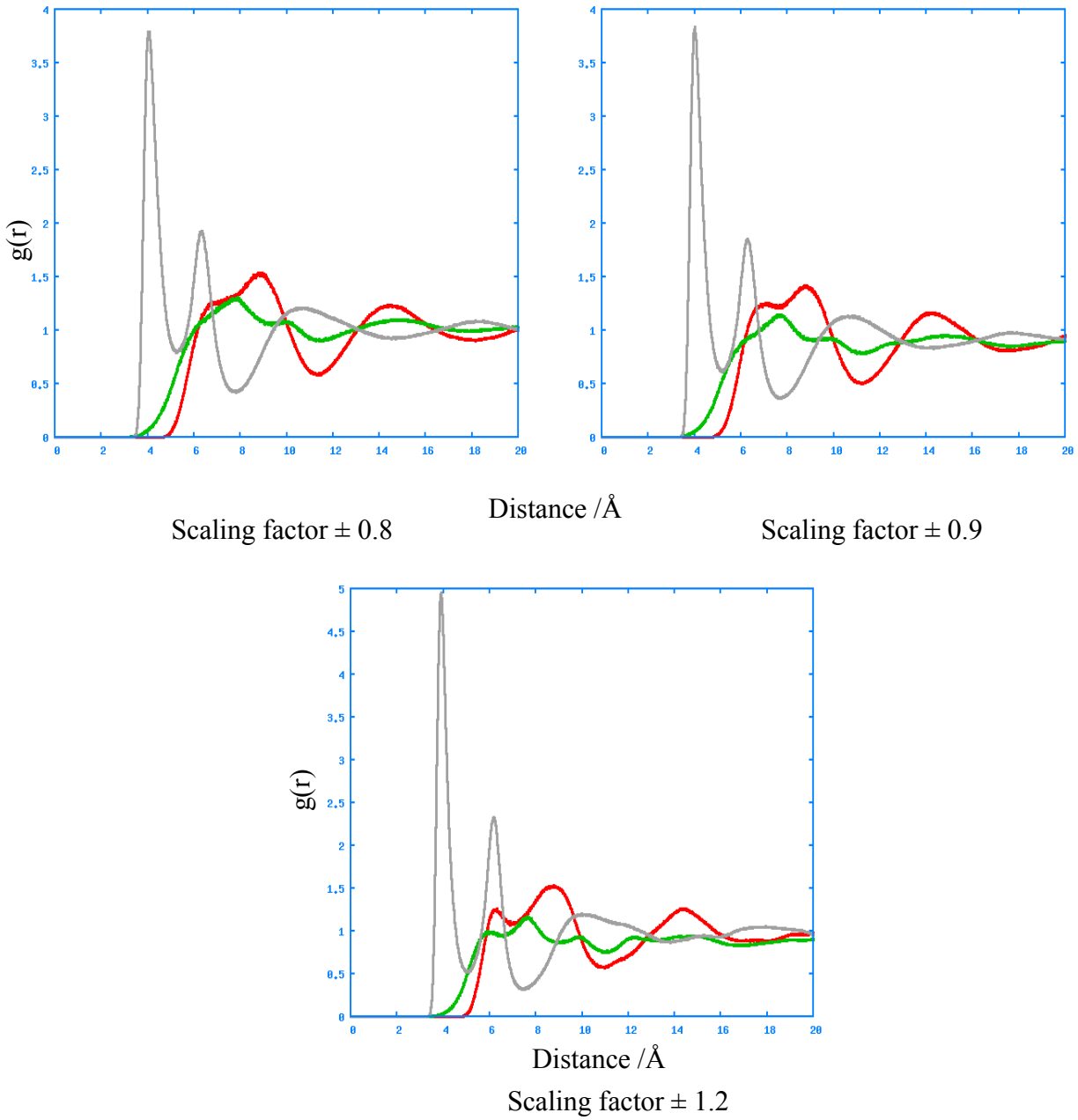

Figure A4.2: cation-cation, anion-anion and cation-anion radial distribution functions for a [C_4MIM][PF_6] ionic liquid calculated over a 5 ns trajectory.

A5.1 Charge schemes

Table A5.1: DF Partial Atomic Charges ([C_4MIM][BF_4]).

Atom	q /e	Atom	q /e
C_5	-0.241	H_{11}	0.021
C_4	-0.173	H_{12}	0.024
C_2	-0.003	C_{10}	-0.276
N_1	0.134	H_{13}	0.070
N_3	0.140	H_{14}	0.100
H_3	0.244	H_{15}	0.076
H_2	0.269	B_1	0.999
H_1	0.225	F_1	-0.499
C_6	-0.291	F_2	-0.500
H_4	0.147	F_3	-0.499
H_5	0.162	F_4	-0.501
H_6	0.163		
C_7	-0.275		
H_7	0.143		
H_8	0.157		
C_8	0.068		
H_9	0.035		
H_{10}	0.036		
C_9	0.045		

Table A5.2: DF Partial Atomic Charges ([C_4MIM][PF_6]).

Atom	q /e	Atom	q /e
C_5	-0.1706	H_{11}	0.0040
C_4	-0.1694	H_{12}	0.0226
C_2	0.0237	C_{10}	-0.2722
N_1	0.0274	H_{13}	0.0647
N_3	0.1692	H_{14}	0.0804
H_3	0.2306	H_{15}	0.0707
H_2	0.2425	P_1	1.293
H_1	0.2314	F_1	-0.385
C_6	-0.3105	F_2	-0.385
H_4	0.1178	F_3	-0.379
H_5	0.1714	F_4	-0.386
H_6	0.1775	F_5	-0.377
C_7	-0.0874	F_6	-0.380
H_7	0.1277		
H_8	0.1197		
C_8	-0.0136		
H_9	0.0176		
H_{10}	0.0636		
C_9	0.0611		

Table A5.3: CPC Partial Atomic Charges ([C_4MIM][BF_4]).

Atom	q /e	Atom	q /e
C_5	-0.142	H_{11}	0.031
C_4	-0.274	H_{12}	0.016
C_2	0.027	C_{10}	-0.319
N_1	0.089	H_{13}	0.090
N_3	0.194	H_{14}	0.094
H_3	0.238	H_{15}	0.084
H_2	0.257	B_1	0.977
H_1	0.231	F_1	-0.503
C_6	-0.293	F_2	-0.487
H_4	0.145	F_3	-0.498
H_5	0.146	F_4	-0.501
H_6	0.149		
C_7	-0.180		
H_7	0.130		
H_8	0.120		
C_8	0.046		
H_9	0.032		
H_{10}	0.037		
C_9	0.051		

Table A5.4: CPC Partial Atomic Charges ([C_4MIM][PF_6]).

Atom	q /e	Atom	q /e
C_5	-0.192	H_{11}	0.002
C_4	-0.197	H_{12}	0.023
C_2	-0.078	C_{10}	-0.279
N_1	0.110	H_{13}	0.064
N_3	0.224	H_{14}	0.073
H_3	0.245	H_{15}	0.073
H_2	0.250	P_1	1.284
H_1	0.252	F_1	-0.383
C_6	-0.349	F_2	-0.387
H_4	0.154	F_3	-0.377
H_5	0.169	F_4	-0.384
H_6	0.175	F_5	-0.373
C_7	-0.078	F_6	-0.379
H_7	0.127		
H_8	0.107		
C_8	-0.095		
H_9	0.045		
H_{10}	0.080		
C_9	0.094		

A5.2 CPC Charges - Density

Table A5.5 shows the density of RTILs predicted from molecular dynamics simulations using the two charge schemes disused in section 5.3.1.1 and the values predicted from experiments.

Table A5.5: liquid densities for $[C_4MIM][BF_4]$ and $[C_4MIM][PF_6]$ at 33.15 K.

	Density /g.cm^{-3}	
	$[C_4MIM][BF_4]$	$[C_4MIM][PF_6]$
Simulation (CPC)	1.079 ± 0.0015	1.346 ± 0.0015
Simulation (DF)	1.081 ± 0.0031	1.342 ± 0.0023
Experiment	1.178 [13]	1.340 [13]

A5.3 CPC Charges - Liquid Structure

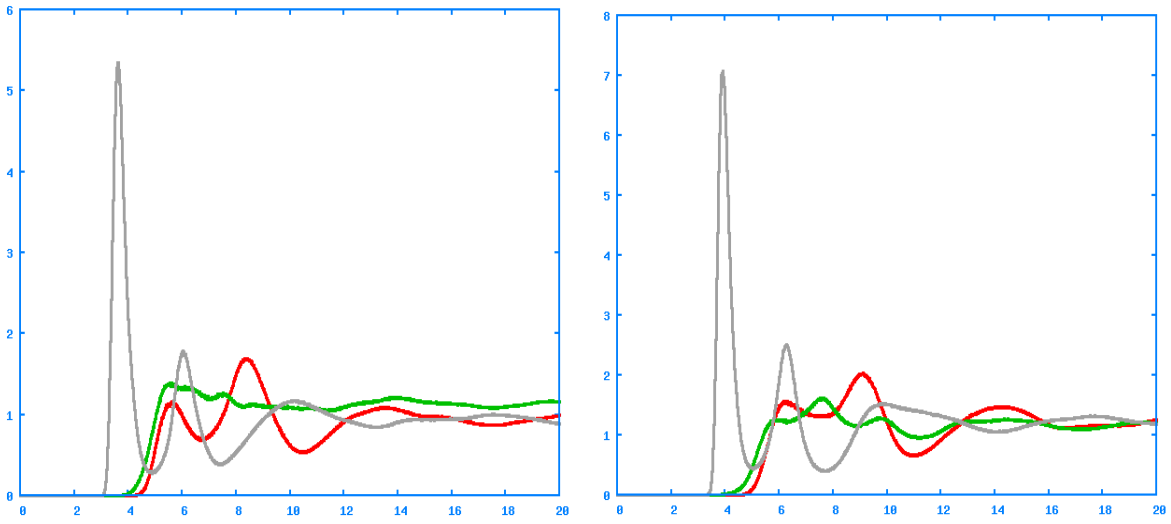

(a) (b)

Figure A5.1: cation-cation, anion- anion and cation-anion radial distribution functions for a (a) $[C_4MIM][BF_4]$ and (b) $[C_4MIM][PF_6]$ ionic liquid calculated over a 5 ns trajectory.

Table A5.6: Maximum and Minimum Positions of Atom-Atom Radial Distribution Functions of RTILs and the First and Second Shell Coordination Numbers from a force field model using CPC charges.

	[C_4MIM][BF4]					
	Position[a] / Å				Number of ions	
	$\mathbf{R}_{max1}$	$\mathbf{R}_{min1}$	$\mathbf{R}_{max2}$	$\mathbf{R}_{min2}$	N_1	N_2
X – X	5.6	6.7	8.3	10.4	3.8	15.6
C_2 – C_2	5.5	7.0	7.5	8.0	2.0	7.3
C_2- X	3.7	4.9	6.0	7.8	2.1	5.5
	[C_4MIM][PF6]					
X – X	6.2	7.6	9.1	10.9	3.7	15.7
C_2 – C_2	5.9	6.4	7.6	8.6	2.2	7.8
C_2- X	3.9	5.1	6.2	7.8	2.3	5.7

[a]The values tabulated refer to locations of the maximum and minimum of the radial distribution function